DENSIFICATION AND ENHANCEMENT OF THERMOMECHANICAL PROPERTIES OF 3D SIC USING SILICA NANOWIRE GROWTH MODELING & IN-SITU MINERALIZATION TECHNIQUE

by

Farjana Sultana

A dissertation submitted to the faculty of
The University of North Carolina at Charlotte
in partial fulfillment of the requirements
for the degree of Doctor of Philosophy in
Mechanical Engineering

Charlotte

2024

Approved by:

_____
Dr. Ahmed El-Ghannam

_____
Dr. Harish Cherukuri

_____
Dr. Qiuming Wei

_____
Dr. Youxing Chen

_____
Dr. Ian Marriott

ABSTRACT

FARJANA SULTANA. Densification and Enhancement of Thermomechanical Properties of 3D SiC Using Silica Nanowire Growth Modeling & In-Situ Mineralization Technique. (Under the direction of DR. AHMED EL-GHANNAM and DR. HARISH CHERUKURI)

Silicon carbide (SiC) is a promising material for high-temperature applications in various industries. Additive manufacturing (AM) of SiC has gained attention due to its challenging manufacturing process, and previous studies from our lab have shown that the creation of a silica gel layer on the surface of SiC using NaOH solution activated the surface and allowed 3D printing of SiC using water based binder in a powder bed binder jet printer. The dried silica gel layer binds adjacent SiC particles upon hydration during 3D printing at room temperature. The 3D printed green parts require a secondary surface activation by impregnating in NaOH solution and thermal treatment to enhance density and strength. The secondary surface activation technique creates an additional silica layer on the surface of SiC at room temperature which can lead to the growth of silica nanowire inside the pore of 3D printed SiC parts upon heat treatment. The hypotheses underlying this approach are twofold: (i) maximum growth of the silica nanowires will facilitate densification and mechanical properties, and (ii) the silica gel layer can mediate a strong bond between SiC and silicate minerals such as mullite. This thesis has three main objectives. First to understand the effect of post processing parameters including concentration of NaOH, thermal treatment temperature and dwelling time on silica nanowires growth and subsequent density and mechanical properties, second, to develop and validate a mathematical model for silica nanowires' growth and ceramic strengthening, and the third objective is to examine the role of creating liquid mullite bonding agent instead of silica layer for the purpose of achieving denser SiC composite. This thesis is structured into two parts: (i)

experimentally optimizing the post processing parameters for silica (SiO_2) nanowire growth inside the pore of 3D printed SiC discs based on quantitative SEM analysis and development of a mathematical growth model for silica nanowire growth, and (ii) creating in situ synthesized liquid mullite as a secondary binder phase for the densification and strengthening of 3D SiC manufactured using powder metallurgy technique.

In the first part, the effects of post processing parameters, such as NaOH concentration, sintering temperature, and time, on silica nanowire growth are investigated. The silica nanowires, grown through vapor-solid noncatalytic mechanism, depend on NaOH concentration, with 20% NaOH showing the highest nanowire number density. The optimal combination for nanowire growth involves impregnation with 10% NaOH and heat treatment at 550 °C for 6 hours and 1100 °C for 4 hours. This results in a nanowire number density of 55431 ± 9232 mm^{-2}, with a compressive strength of 9.86 ± 1.4 MPa, density of 2.27 gcm^{-3}, and porosity of 38.32%. Subsequently, a mathematical nanowire growth model was developed using experimental data in order to investigate the growth mechanism and understand the effect of reaction kinetics on the nanowire growth. The model accounted for the reaction kinetics controlling the formation of silica molecule and its subsequent deposition on nanowire top surface contributing to the growth of the nanowire. The change in nanowire length relation with respect to different post processing parameters obtained from the model showed a good agreement with the experimental data.

The silica gel layer on the surface activated SiC particles transforms into cristobalite (SiO_2) upon heat treatment which serves as a binding agent that holds the SiC particles together and controls the thermomechanical properties, density and porosity of the 3D printed SiC. Therefore, in the second part of this dissertation, addressing the limitations of cristobalite's mechanical and thermal properties in comparison to SiC, an in-situ mullite binding agent was

developed. The composition of 85SiC/15ash exhibits the highest mechanical strength among the samples, with a compressive strength of 434 ± 20 MPa. XRD analysis reveals a composition of 81.8 wt% SiC, 11.4 wt% mullite, and 6.8 wt% cristobalite in the thermally treated sample. SEM-EDX analysis shows a concentration gradient of Al in cristobalite, enhancing the formation of functionally graded bonding zones between phases. The resulting SiC-mullite composite displays exceptional thermomechanical properties, including a nanoindentation elastic modulus of 370.9 ± 22.6 GPa, Vickers hardness of 11.5 ± 1.2 GPa, and high thermal shock resistance. The mullite binding phase resulted in a dense SiC composite with only 8% porosity. The resulting SiC-mullite composite is suitable for high temperature applications such as diesel motor parts, gas turbines, industrial heat exchangers, fusion reactor parts, high-temperature energy exchanger systems, and hot gas filters due to its high mechanical strength and thermal shock-resistance. This work demonstrated the potential of utilizing an in-situ mullite bonding agent instead of silica layer in additive manufacturing of SiC in the powder bed binder jet process for achieving a dense SiC parts with high thermomechanical properties.

DEDICATION

This dissertation is dedicated to my beloved mother, whose sacrifices and unwavering encouragement have played an integral role in shaping the person I have become. To my late father, your wisdom resonates in every accomplishment. My sister, who has been a huge source of strength and encouragement throughout. To my husband, Dr. Shank Kulkarni, for his endless support, care, and love. Additionally, I dedicate this work to the treasured memories of my friends, Pracheta and Imtiaz, whose sudden departure has left an irreplaceable void in my life.

ACKNOWLEDGEMENTS

I would like to express my heartfelt appreciation to my advisor, Dr. Ahmed El-Ghannam, for his unwavering support, guidance, and mentorship for my research work at UNC Charlotte. His consistent encouragement and belief in my abilities served as a constant motivator during the course of my research. A special acknowledgment goes to my co-advisor Dr. Harish Cherukuri for his invaluable support, guidance, and insightful contributions to this study. I am eternally grateful to Dr. Cherukuri and his wife, Dr. Debarati Dutta, for their unwavering support and condolences during the most challenging period of my life after arriving in the USA. I would like to extend my thanks to the members of my dissertation committee, Dr. Qiuming Wei, Dr. Youxing Chen, and Dr. Ian Marriott, for their valuable input and support.

A special thanks is extended to my husband, Dr. Shank Kulkarni, for his tremendous support, care, and encouragement. I would also like to thank my lab mate, Dr. Sujithra Chandrasekaran, for imparting essential knowledge on operating diverse equipment, maintaining the lab, and for her support and friendship. Lastly, my deep appreciation goes to my family, friends, and colleagues for their unwavering support, contributing to the creation of fond memories during my time at UNC Charlotte.

TABLE OF CONTENTS

LIST OF TABLES

LIST OF FIGURES

PART I

SILICA NANOWIRE GROWTH

CHAPTER 1: INTRODUCTION

1.1 SiC and manufacturing of SiC

Silicon Carbide (SiC), commonly known by its historical name "carborundum," stands at the forefront of advanced materials with its unique combination of exceptional physical, chemical and mechanical properties. This compound, composed of silicon and carbon, has gained significant attention in both scientific and industrial communities due to its remarkable characteristics including low density, high thermal conductivity, low thermal expansion, high mechanical strength and thermal shock resistance [1-7]. The unique properties of SiC and related materials make them as suitable candidates for different military and engineering fields that operate at elevated temperature, such as armor, gas turbine parts, for molten metal and gas filtration, aerospace, optical mirrors and in nuclear energy stations [8-13].

The application of SiC in military or engineering fields necessitates the creation of complex three-dimensional SiC ceramic components, posing significant challenges to their fabrication [14-16]. Traditionally, various techniques have been employed for the fabrication of SiC ceramics, including pressure-assisted methods like hot pressing, pressed preforms followed by sintering, liquid silicon infiltration (LSI), chemical vapor infiltration (CVI), and precursor impregnation and pyrolysis (PIP) [13, 17-20]. However, a significant drawback of these methods is their limited capability to produce components with complex geometries. Currently, the production of three-dimensional complex shaped SiC ceramic components employs two methods. The first, sintering and machining, creates bulk SiC ceramic through various sintering methods and shapes it using machining techniques [21, 22]. The second, near-net forming and sintering, involves creating a complex-shaped SiC green body through processes like slip casting or injection molding, followed by pressureless sintering [23-26]. However, both approaches have

drawbacks. In the sintering and machining approach, the intrinsic brittleness and hardness of SiC ceramic lead to machining defects and damages, reducing service properties and longevity [22]. Additionally, the machining of ceramics is a costly and labor-intensive process. Data in the literature showed mechanical tooling costs can constitute up to 80% of the overall manufacturing expenses for ceramic part [27]. The near-net forming and sintering approach requires molds, extending production cycles and costs. Techniques like slip casting and injection molding often compromise precision, density, and strength due to mold reliance. Gel casting, avoiding molds, involves toxic materials [23]. Both approaches fall short of meeting the demands for manufacturing complex 3D SiC ceramic components, emphasizing the urgent need for alternative fabrication methods such as additive manufacturing (AM).

1.2 Additive manufacturing of SiC

The emergence of additive manufacturing (AM) technologies, commonly known as 3D printing, marks a transformative phase in material fabrication, bringing about a revolution in the production of complex structures characterized by enhanced precision and customization. Unlike traditional methods that often involve subtracting material from a larger block, AM builds up structures layer by layer. This layer-by-layer fabrication process allows for precise control over the geometry of the final product, resulting in complex and highly customized designs that might be impractical or impossible to achieve through conventional techniques. AM presents an opportunity to create intricate 3D structures using a variety of materials [28, 29].

The integration of AM techniques into the manufacturing processes of SiC holds the promise of overcoming traditional constraints and unlocking novel possibilities for the application of this remarkable material. Early attempts at incorporating SiC into additive manufacturing processes faced challenges related to the material's high melting point and

susceptibility to thermal stresses. However, recent breakthroughs have demonstrated that the feedstock materials for SiC ceramics in AM can be pre-ceramic polymers, powder-based materials, or reactive chemical-based substances. The selection of feedstock type depends on the specific AM methods used. AM methods necessitating subsequent densification processes include stereolithography, direct ink writing, gel casting, binder jet printing, and laminated object manufacturing [30-38]. Conversely, AM methods capable of layer-by-layer consolidation include selective laser sintering (SLS) and selective laser chemical vapor deposition (LCVD) [39, 40]. Each AM method comes with its set of advantages and drawbacks concerning component size, feature size, additive process speed, presence or absence of structural support during AM, surface quality, cost, and dimensional restrictions which was discussed in detailed by Chen et al. [41].

In this thesis, we focused on the AM of SiC using powder bed binder jetting technique. This dissertation discusses the complexities of binder jetting AM technique, addressing the current challenges for SiC manufacturing, and proposing innovative solutions to propel this field forward.

1.3 Powder bed binder jetting AM technique

Powder bed binder jetting 3D printing (PBBJ) emerges as a promising AM technology, employing an inkjet-based process with powders to construct three-dimensional objects [42]. The process initiates with the digital modeling of the intended product in a Computer-Aided Design (CAD) package, followed by converting the CAD model into a digital stereolithography file format (STL file) for printing. Once the STL file is fed into the printer, then the printing process begins with a powder-spreading roller moving horizontally to spread a powder layer evenly on the build bed. Subsequently, a liquid binder, such as a polymer in a solvent or aqueous solution, is jetted from the printhead onto the designated powder layer based on the slice data, forming a

curing layer by binding selected powder particles. The build bed descends for each layer by a piston supporting the build bed, and a new powder layer is applied, this process is repeated layer by layer until the entire three-dimensional structure is complete [43, 44]. After the printing step, some binder jet technologies may require post-curing, involving the removal of the bed from the printer and heating until the binder is adequately dried [45, 46]. The resulting green parts, with enough strength, are then handled and moved to the densification furnace. Loose powder in the build box is removed via vacuum and manual brushing, followed by further cleaning of individual parts. The green metal powder parts resulting from the binder jet print process are then densified either by sintering to full density or infiltration with another material [47, 48]. Figure 1 summarizes the complete PBBJ AM process along with the different post processing steps used for enhancing the mechanical properties of 3D printed green body.

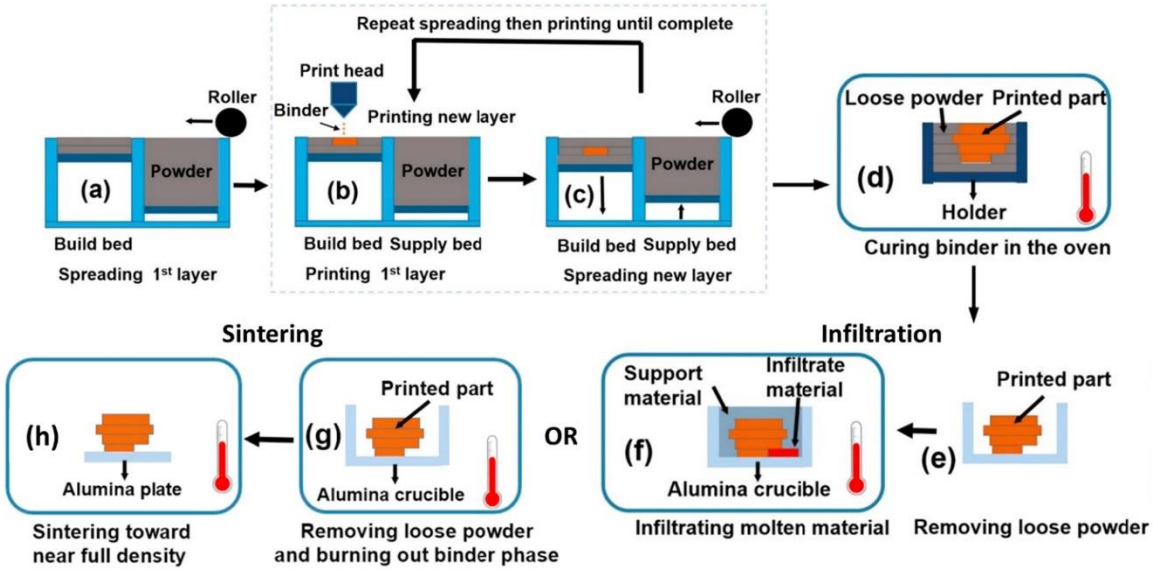

Figure 1: Illustration of PBBJ AM process [49]. (a) Initial steps involve preparing the foundation and the first layer for binder jetting. (b, c) The process continues by jetting binder onto the powder bed and spreading a new layer of powder, repeating this sequence until the entire printing process is completed. (d) The printed structure undergoes binder curing in an oven. (e) Loose powder is removed through depowdering. (f) Infiltration step. (g) Another depowdering step is performed, leading to (h) the final sintering stage in a controlled atmosphere for consolidation.

PBBJ is a highly promising AM technology for ceramic materials, offering exceptional design freedom and scalability. One of its key advantages lies in the absence of supporting

structures for parts with overhangs or bridges, coupled with compatibility with a wide range of materials [50]. PBBJ demonstrates a relatively high building rate compared to other AM technologies [51]. Moreover, in the PBBJ process, the bonding of powder occurs layer by layer, resulting in the absence of residual stress in the sample. This characteristic makes it particularly suitable for brittle materials like ceramics [52].

However, a significant drawback of this technology is the low packing density of powder layers and the utilization of a binder for part construction. This combination gives rise to high porosity and low mechanical properties in the produced green parts [53, 54]. The weak connection between powder particles sets it apart from other additive manufacturing processes.

While parts produced through binder jetting exhibit a high level of porosity, achieving a high density in ceramic components is still attainable through the use of subsequent post processing techniques like sintering or infiltration. For example, Gonzalez et al. [55] accomplished 96% of the theoretical density for aluminum oxide parts after sintering at 1600 °C/16 hr. In another study done by Fielding et al. [56], 95% density was achieved after post processing by adding ZnO and SiO_2 into ($Ca_3(PO_4)_2$) powder. Melcher et al. utilized copper infiltration to create dense parts from alumina green samples with 36% density [57]. Hence, the development of post processing strategies is essential for further enhancement of the density and mechanical strength of the additively manufactured green body.

1.4 Post processing techniques used for SiC green body after PBBJ 3D printing

PBBJ has been employed for SiC ceramic fabrication, often followed by densification methods like melt infiltration or sintering. Various studies, such as those by Lv et al. [58], Baux et al. [59], Fleisher et al. [60], and Fu et al. [61] have utilized PBBJ to create SiC green bodies, subsequently applying methods like chemical vapor infiltration (CVI), chemical vapor deposition

(CVD), capillary liquid silicon infiltration (CLSI), and pyrolysis to achieve densification. These densification processes (such as CVI, CVD, CLSI, PIP, etc.) after PBBJ can introduce material defects. For example, methods like melt infiltration result in two-phase composite materials, while sintering causes volume shrinkage and distortion. CVI, although providing a dense, single-constituent part, has limitations in component dimensions and topological complexity. The infiltration processes may lead to incomplete densification in thick or complex components. These challenges highlight the need for innovative approaches to enhance the quality of PBBJ - prepared SiC ceramics.

In this work the 3D printed SiC green body after heat treatment at 650 °C/5 hr was subjected to an impregnation treatment using NaOH solution. Our previous publications [62-64] showed that when NaOH solution was mixed with SiC particles, NaOH broke the Si–C bond in SiC, released silanol groups ($Si(OH)_n$, n = 1–4) on the material surface before subsequent heat treatment. The low electronegativity of Si facilitated the bonding with hydroxyl ions (OH), leading to the spontaneous re-polymerization of silanol groups into a uniform amorphous gel layer on the SiC particle surface. Alkali solution oxidation of SiC allowed precise control over SiO_2 thickness at room temperature, promoting passive oxidation, weight gain, and densification upon heat treatment. Using silica gel coated SiC particles in disc preparation provided dimensional stability advantages over traditional sintering methods prone to disc shrinkage and weight loss. The pre-formation of a silica gel layer upon heat treatment in the temperature range from 800 to 1100 °C, directed oxidation reaction to produce silica nanowires inside the pore of SiC disc, enhancing the strength of the disc while maintaining dimensional stability. Improved mechanical properties may have resulted from enhanced silica layer diffusion, potentially facilitated by sodium, leading to better bonding between SiC particles and also the silica

nanowire formations that bridged the walls between particles that subsequently densified the resulting solid. Therefore, similar densification and strengthening technique was adapted for the 3D printed SiC green body through the formation of silica nanowire inside the pore of 3D printed SiC disc after impregnation in NaOH solution and subsequent heat treatment.

1.5 Hypothesis

The hypothesis behind this work is that the maximum growth of the silica nanowires will facilitate densification and mechanical properties of the additively manufactured SiC parts.

1.6 Objective

There are two main objectives for this part of the thesis. First to understand the effect of post processing parameters including concentration of NaOH, thermal treatment temperature and dwelling time on silica nanowires growth and subsequent density and mechanical properties, second, to develop and validate a mathematical model for nanowires' growth and ceramic strengthening using the experimental data.

1.7 Silica nanowire growth

In the past two decades, the growth and characterization of one-dimensional (1-D) nanostructures such as nanotubes, nanowires, nanobelts have gained a lot of attention because of their distinctive structure, unique properties, and applications [65-67]. Furthermore, the development of 1D or 2D nanomaterials as reinforcement in ceramic matrix composite has attracted great interest in recent years due to their high mechanical and distinctive physical properties [68]. Nanowires play a crucial role as reinforcement materials in ceramics, addressing challenges related to adhesion and structural integrity. Their high aspect ratios, low diameters, and outstanding mechanical properties make them ideal candidates for enhancing the performance of ceramic matrix composites (CMCs) [69, 70]. Several studies have shown the

implementation of nanowires as reinforcement materials, such as SiC nanowires (SiC nws) [71-78], offer improved tensile strength, flexural strength, and toughness to the composite materials, contributing to increased specific strength and stiffness. Due to outstanding physicochemical stability, lately, there has been a growing focus on developing nanofiber-based CMCs such as alumina nanofiber/geopolymer matrix composites [79], carbon nanofiber-reinforced alumina [80], and zirconia [81], along with a composite film incorporating carbon nanofibers and ZrB2 [82], glass fiber [83], and silica nanowires [84]. Among them, silica nanowires (SiO_2 nws) are one-dimensional nanostructures with unique characteristics, ranging from a few nanometers to micrometers in diameter. These nanowires tend to form intricate morphologies, including flowers, carrots, clusters, and spheres [85]. Several methods such as laser ablation [86], oxide-assisted growth [87], sol-gel template method [88], carbothermal reduction [89], and gas-phase growth [90] (i.e., vapor-liquid-solid, solid-liquid-solid, vapor-solid growth) have been used to synthesize silica nanowires. Silica nanowires possess a large aspect ratio, making them valuable in various applications, especially as reinforcing elements in composite materials.

In this work, silica nanowire was grown by vapor-solid (VS) mechanism inside the pore of additively manufactured SiC disc during sintering as reinforcing material for the 3D printed SiC discs. The density, porosity and mechanical strength of the 3D printed SiC samples depended on the silica nanowire number density, nanowire dimensions. Previous studies from our lab showed that the nanowire number density and size such as length and width of the nanowires varied with respect to the experimental parameters such as NaOH concentration and thermal treatments [62-64]. However, previous investigations lacked a comprehensive analysis of both quantitative and qualitative characteristics of silica nanowires. Given the significant influence of shape, size, and morphology on the ultimate physical and chemical properties of

nanowires, this study aims to explore how post-processing parameters influence the number density, size, and morphology of silica nanowires. This can be achieved through a meticulous analysis employing quantitative SEM image analysis in conjunction with a nanowire growth model. The primary focus of this work is to determine the optimal NaOH concentration and thermal treatment conditions that facilitate the nucleation and growth of secondary silica nanowires within the pores of 3D-printed SiC components, consequently enhancing densification and mechanical properties. The development of nanowire growth model is crucial for maximizing the output of nanowire synthesis.

The morphologies and number density of silica nanowires as a function of NaOH concentration, sintering temperature, and dwelling time were analyzed with the help of differential scanning calorimetry (DSC) and thermogravimetric (TG) analysis. DSC analysis measures the heat flow into or out of a sample as a function of temperature or time. It is commonly used to investigate phase transitions, such as melting, crystallization, glass transitions, and chemical reactions that involve heat changes. During a DSC analysis, a sample and a reference material are subjected to identical thermal cycles, and the heat difference between them is recorded. This provides information about the material's heat capacity, enthalpy changes, and the temperature at which transitions occur. TG analysis, on the other hand, measures the weight change of a sample as a function of temperature or time in a controlled atmosphere. This technique is particularly useful for studying decomposition, oxidation, and volatilization processes. During a TG analysis, the sample is heated or cooled, and its weight change is recorded. The temperature at which specific weight changes occur can provide insights into the thermal stability and composition of the material. Based on the DSC-TG analysis, NaOH concentrations and heat treatment protocol have been selected for analyzing the effect of post

processing parameters on silica nanowires growth using a quantitative SEM image analysis technique.

1.8 Nanowire growth model

While experimental validation remains important in materials science research, the integration of numerical modeling serves as a powerful complement, providing insights into underlying processes and aiding in the prediction of complex phenomena. A notable example is nanowire formation, where the low repeatability of growth poses a significant challenge for mass production. Achieving nanostructures with specified properties involves prolonged optimization of technological parameters such as temperature, carrier flow, and annealing time, necessitating an extensive series of experimental studies [91]. Consequently, delving into the nanowire formation process becomes essential for a more profound understanding of the physics governing growth on activated surfaces [92], necessitating the development of appropriate theoretical models. It requires the development of adequate theoretical models. Previous modeling studies have covered diverse growth mechanisms, including vapor-liquid-solid (VLS) and vapor-solid (VS) processes. For instance, diffusion-induced nanowire growth models have been crafted for various nanowires (e.g., Ge, GaN, GaP) formed via the vapor-liquid-solid (VLS) mechanism [93-97]. Simakov, V., et al [91] has developed a diffusion transport model for the selective growth of tin dioxide nanowires using the VS (vapor–solid) mechanism through catalyst-free physical vapor deposition. However, these established mathematical models predominantly focus on nanowire growth on substrate surfaces within controlled environments. Notably, there is an absence of mathematical models in the literature exploring nanowire growth mechanisms in bulk materials. The primary challenge in developing such models lies in the scarcity of data and a comprehensive understanding of the growth process.

This work introduces a theoretical growth model for silica nanowires formed within the pores of a SiC disc. The objective is to construct a theoretical framework elucidating the dynamics of nanowire growth and subsequently validate this model through experimental measurements. This work advances the field by introducing a numerical model specifically tailored to the NaOH solution impregnation-induced silica nanowire growth in SiC. Ordinary differential equations (ODEs) have been formulated to represent the dynamic evolution of nanowire length over time, considering key parameters such as solution concentration, sintering temperature and time. The numerical implementation utilizes the forward Euler method within the MATLAB environment to predict the increase of silica nanowire lengths under various processing conditions.

To establish the credibility of the numerical model, extensive comparisons have been made between theoretical predictions and experimental measurements of nanowire lengths obtained through controlled impregnation processes. The agreement between model predictions and experimental data not only validates the proposed ODEs but also provides a deeper understanding of the underlying mechanisms governing silica nanowire growth in SiC discs. The integration of numerical modeling into the exploration of silica nanowire growth offers a predictive tool for optimizing the proposed post processing technique for AM of SiC.

CHAPTER 2: EXPERIMENTAL WORK ON SILICA NANOWIRE GROWTH

2.1 Materials and methods

2.1.1 3D printing of SiC using 3DProjet460Plus printer

The raw materials used for printing were a powder mixture of 70 weight % of SiC powder (US Nano research, Houston, TX, USA) with average particle size of 40 µm, 15 weight % of SiC with average particle size of 2 µm and 15 weight % of SiC with average particle size of 600 nm [98]. As described in a previous study from our lab [98] prior to mixing with submicron SiC particles, the 40 µm SiC powder was mixed with a 20% sodium hydroxide solution using a commercial power drill with a paint mixer with a 1-3/4" spiral blade, resulting in a homogenous slurry after 30 minutes. The mixture was covered and left for 24 hours, then decanted, and washed with nanopure water. The washing process was repeated until the pH of the SiC suspension reached 10 - 11. The particles were dried overnight in a chemical fume hood, followed by milling with alumina beads for 4 hours using a roller mixer. Next, the SiC powder was sieved and dried in an oven at 100 °C for 12 hr and again the SiC powder was milled using the roller mixture to break any clumps. The binder jetting machine used in this research is Projet460Plus printer from 3D systems (Rock hill, SC). 3D printed SiC discs of 10 mm diameter x 7 mm height for post processing analysis and cylinders of 10 mm diameter x 20 mm height for mechanical strength measurement, were printed using a layer thickness of 102 µm. The binder used in this work from 3D systems was a water-based binder system (with anaerobic bacteria) without requirement of curing of the printed parts. Upon completion of printing, the printed samples were carefully taken out of the build bed and were heat treated in a Thermolyne™ (Thermo Scientific, Vernon Hills, IL) muffle furnace at 650 °C/5 hr at a rate of 10 °C/min [98]. During the heat treatment process, the water-based binder phase burnt out from the printed parts

and the formation of amorphous SiO_2 on the surface activated 40 µm SiC particles provided handling strength to printed parts. After this step, any loose powders remaining on the green parts were removed by gently using the air blower attachment on the ProJet 460 Plus printer. Then, in order to achieve further densification and strengthening of the 3D printed SiC green parts, various post processing steps were performed based on the differential scanning calorimetry (DSC) and thermogravimetric analysis (TGA) method discussed in the next section.

2.1.2 Sample preparation and differential scanning calorimetry (DSC) and thermogravimetric analysis (TGA) preparation

40 µm average particle size SiC powders were pretreated with 5%, 10% and, 20% NaOH, were hand pressed in a tungsten carbide die for a duration of 1 min without any external compact pressure to mimic the 3D printing process and a disc of 5 mm diameter x 4 mm length was prepared. The thermal analysis of SiC discs were performed using a coupled DSC-TGA thermal analyzer TA SDT Q600 (TA Instruments) in air environment at a heating rate of 10 °C/min over the range from room temperature to 1100 °C and maintained at 1100 °C for 30 mins. The thermal analysis was performed on these SiC discs to select the optimal thermal treatment parameters for post processing stage that facilitate nucleation and growth of silica nanowires inside the pores of 3D printed SiC parts and enhance densification and mechanical properties.

2.1.3 Effect of post processing parameters on 3D printed SiC green parts

2.1.3.1 Effect of NaOH concentration on the silica nanowire growth

Objective: The objective of this experiment was to determine the optimum NaOH concentration that enhances densification and strengthening of 3D printed SiC samples by creating maximum nanowire growth and nanowire number density (mm^{-2}). 3D printed SiC discs (10 mm diameter x 7 mm height) pretreated at 550 °C/6 hr were impregnated separately in 5%,

10%, and 20% NaOH solution for 15 mins and were subjected to two-step heat treatment procedure. Based on the DSC-TGA analysis, the NaOH-impregnated 3D printed SiC discs were heat treated at nucleation temperature (550 °C) for 6 hr and then the secondary heat treatment was done at crystallization temperature (800 °C) for 2 hr. After thermal treatment, the density of the samples was measured using Archimedes method, the mechanical properties were measured in compression mode and the fracture surface was analyzed by SEM-EDX.

2.1.3.2 Effect of sintering temperature on the silica nanowire growth

Next, the effect of sintering temperature on the densification and strengthening of the 3D printed SiC samples by creating optimum nanowire growth and nanowire number density (mm^{-2}) were analyzed by varying the sintering temperatures. In this analysis, 10% NaOH was chosen for impregnating 3D printed SiC green parts, based on the findings from previous experiment. The selection is supported by the observation that 10% NaOH demonstrated favorable dimensional stability compared to 20% NaOH and superior mechanical properties compared to 5% NaOH. 3D printed SiC discs (10 mm diameter x 7 mm height) were impregnated in 10% NaOH solution for 15 mins and were subjected to two-step heat treatment process discussed in section 2.3.1. At first all the samples were heat treated at nucleation temperature (550 °C) for 6 hr and then subjected to heat treatment at various sintering temperature ranging from 800 °C/2 hr, 900 °C/2 hr, 1000 °C/2 hr and 1100 °C/2 hr. After thermal treatment, the mechanical properties of the 3D printed SiC cylinders (n=7) of 10 mm diameter x 20 mm height were measured.

2.1.3.3 Effect of dwelling time on the silica nanowire growth

It was found from the previous experiment that thermal treatment at 1100 °C led to the maximum nanowire number density and growth, the current study focused on analyzing the impact of dwelling time on nanowire growth. Therefore, the temperature was held constant at

1100 °C, while varying the dwelling time to investigate its influence on silica nanowire development and mechanical properties of 3D printed SiC parts.

The objective is to determine the optimum dwelling time at 1100 °C that enhances the densification and strengthening of the 3D printed SiC samples by promoting maximum nanowire growth and nanowire number density (mm^{-2}). 3D printed SiC discs (10 mm diameter x 7 mm height) were impregnated in 10% NaOH solution for 15 mins and were subjected to two-step heat treatment process. First all the samples were heat treated at nucleation temperature (550 °C) for 6 hr and then at 1100 °C for 2 hr, 4 hr, 6 hr, or 8 hr in air. 3D printed SiC cylinders (n=7) (10 mm diameter x 20 mm height) were prepared for mechanical properties measurements. Fracture surface was analyzed by SEM-EDX.

2.1.4 Characterization

2.1.4.1 Density measurements

The apparent open porosity (Pa, %) and density (D, $g \cdot cm^{-3}$) were measured by following the Archimedes principle, employing a density determination kit (Ohaus, Parsippany, NJ) and a digital scale (Ohaus, Parsippany, NJ). Pure DI water served as the immersion liquid. The calculation of apparent density (D) was calculated using Eq. (1),

$$D = \frac{m_d}{m_d - m_w}(D_0 - D_L) + D_L, \quad (1)$$

where, m_d is the dry mass of the sample in grams (g), m_w is the mass of the saturated sample in water (g), D_0 is the density of the DI water ($g \cdot cm^{-3}$), and D_L represents the air density ($0.0012\ g \cdot cm^{-3}$). The apparent open porosity was determined through Eq. (2),

$$P_a = \frac{m_a - m_d}{m_a - m_w} \times 100\%, \quad (2)$$

where, m_a represents saturated sample mass in the air (g).

2.1.4.2 SEM-EDX morphology analysis

Both nanowire growth and the thickness of the bonding zone between SiC particles are important material parameters that control the mechanical properties. Therefore, the fractured surface of the 3D printed samples pre-impregnated with different post processing parameters was analyzed by SEM-EDX. Scanning electron microscope-energy dispersive X-ray (SEM-EDX) analysis was used to analyze the morphology of the sintered discs including:

(i) Droplets number density that is the number of droplets per unit surface area on the wall of the pore, (ii) width of the droplets at the base (at the contact surface with the wall of the pore), similarly, (iii) nanowire number density, and (iv) length and width of the nanowires present inside the pore of the 3D printed SiC discs. The elemental composition of the microstructural features was assessed through Energy-Dispersive X-ray Spectroscopy (EDX) at 20 kV with a working distance of 10 mm using an Oxford Instruments INCA EDS in combination with a JEOL 6480 SEM (SEM, JEOL USA, Waterford, VA).

2.1.5 Quantitative SEM image analysis

Quantitative image analysis was done using SEM images for studying the influence of post processing parameters such as NaOH concentration, sintering temperature and time profile, on silica droplets formation, nanowire growth and width of the bonding zone between fused SiC particles. Silica droplet number density, defined as the number of silica droplets per unit surface area of the pore wall (mm^{-2}), was determined from at least 10 SEM images at x10,000 magnification per three samples. An open-source software, ImageJ developed by the National

Institute of health sciences (LOCI, University of Wisconsin) was employed for SEM image analysis. First, the area of the micrograph was measured and then using the multi-point tool the number of droplets were counted in the measured area. The mean and standard deviations were evaluated to measure the droplets number density with respect to NaOH concentration. The width of the droplets at the base, in contact with the SiC particle surface, was measured, and a histogram divided the data into four groups: 0.08 µm – 0.3 µm, 0.3 µm – 0.6 µm, 0.6 µm – 1 µm, and 1 µm – 4.7 µm. Mean and standard deviations were evaluated to analyze the percentage of droplets in different width groups with respect to post processing parameters. Similarly, the nanowire number density, length and width of the silica nanowires on the fracture surface of 3D printed SiC discs were analyzed using the ImageJ software. For the analysis of nanowires, at least 40 SEM images at x2000 magnification per three samples for different post processing parameters were used. The fractured surface of the SiC discs were divided into 4 quarters and 10 SEM images were collected from each quarter. For the quantitative analysis of nanowire width, tapered nanowires' width was measured at the base of the nanowire close to the SiC particle surface. While measuring nanowire length, the fractured nanowires or the nanowire which both ends were not visible in the micrograph were not considered during measurement. For the analysis of width of silica bonding zone fusing the SiC particles, at least 10 SEM images at x2000 magnification per three samples were captured on the fracture surface of 3D printed SiC discs. ImageJ software was employed for bonding zone width analysis and mean, and standard deviations were evaluated to characterize the width of silica bonding zone between silicon carbide particles.

2.1.6 Compressive strength and modulus of elasticity measurements

The mechanical properties of the thermally treated 3D printed SiC cylinders were measured using an Instron 5582 machine (Instron 5582, Norwood, MA) at 25 °C in air. To analyze the post processing parameters on the compressive strength, 3D printed SiC cylinders (n=7) of 10 mm diameter x 20 mm height were used. The samples were compressed at a rate of 2 mm/min until reaching failure. The stress-strain curves derived from these tests were utilized to determine both compressive strength and the modulus of elasticity under compression.

2.1.7 Statistical analysis

Statistical analysis of mean differences was conducted using One-Way ANOVA test with Tukey's HSD test for multiple comparisons. A significance level of $p < 0.05$ was applied to determine statistical significance.

2.2 Results and discussion

2.2.1 Differential scanning calorimetry (DSC) and Thermogravimetric analysis (TG) analysis

Figure 2 shows the differential scanning calorimetry (DSC) and thermogravimetric (TG) analysis performed on SiC discs (5 mm diameter × 4 mm length) pretreated with 5%, 10% or, 20% NaOH, to determine the nucleation and phase transformation temperatures of the silica phase on the SiC surface.

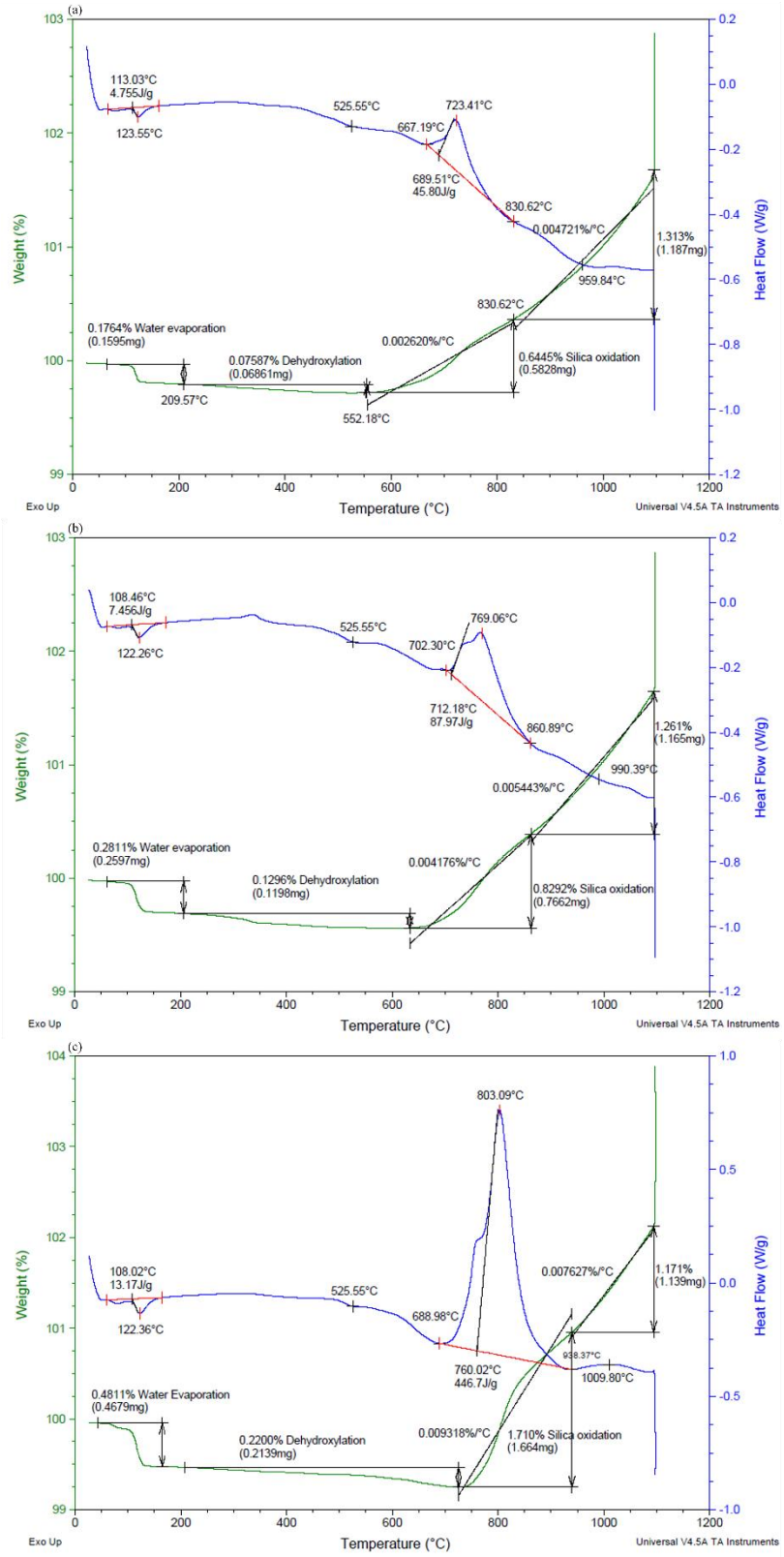

Figure 2: DSC-TG analysis of 40 µm SiC mixed with (a) 5 %, (b) 10 %, and (c) 20 % NaOH, hand pressed using minimal pressure and heat treated to 1100 °C for 30 mins in air environment at a heating rate of 10 °C/min.

DSC analysis showed an endothermic peak at around 122 °C indicating water desorption in the temperature range of 75 – 180 °C. In association with the desorption, TG analysis showed 0.1764%, 0.2811%, and 0.4811% weight loss respectively for samples pretreated with 5%, 10%, and 20% NaOH. This was similar to previous studies that reported desorption of water from amorphous silica in the temperature range 25 – 200 °C [99, 100]. The amount of water desorption increased with the increase in the NaOH concentration due to the increased formation of silica gel layer. This was confirmed in previous studies from this lab where the FTIR analysis showed a significant increase in the area under the peak for the Si-OH and the Si-O-Si as the NaOH concentration varies from 5%, 10%, 15%, 20%, and 40% [101]. Following desorption, the silica gel layer underwent condensation of the hydroxyl groups that led to elimination of water molecules and formation of Si-O-Si siloxane bridges according to the equation given as,

$$Si(OH)_4(s) + Si(OH)_4(s) \rightarrow 2SiO_2(s) + 4H_2O(g)$$

The 0.219% weight loss in the temperature range 200 – 725 °C is attributed to the dehydroxylation process of silica gel as well as the release of SiO and $Si(OH)_4$ vapor molecules. Previous studies using FTIR analyses confirmed the release of silicon oxide and silanol groups from the silica gel layer on the surface of SiC [62, 63]. Dehydroxylation of pure silica in the temperature range from 200 – 700 °C was reported in the literature to be associated with weight losses depending on the surface area of the material [102, 103]. The DSC curves for all samples treated with various concentrations of NaOH showed an endothermic peak at 525.5 °C indicating the nucleation of the silica crystals. Previous studies showed that the T_g of sodium silicate glass that has 1:2 Na:Si ratio was 440 °C [104]. Previous studies from our lab showed that the ratio of Na:Si is much lower than 1:2 and hence the nucleation temperature is expected to be high [62, 63].

DSC analysis showed a major exothermic peak due to crystallization in the temperature range from 667 - 831 °C, 702 - 861 °C, and 689 - 938 °C for samples pretreated with 5%, 10%, and 20% NaOH. Measurement of area under the peaks showed an increase in the ΔH as the NaOH concentration increased from 5% to 20%. The ΔH for samples pretreated with 5%, 10%, and 20% where 45.8 J/g, 87.97 J/g, and 446.7 J/g, respectively. The increase in ΔH correlates with the significant weight gain observed by TG analysis associated with increased oxidation reaction that led to nanowire formation according to the reactions given by,

$$2SiO\ (g) + O_2(g) \rightarrow 2SiO_2(s)$$

$$Si(OH)_4(g) + Si(OH)_4(g) \rightarrow 2SiO_2(s) + 4H_2O(g)$$

The TG analysis showed that the weight gains for samples treated with 5, 10 and 20% NaOH were 1.77 mg, 2.03 mg, and 2.80 mg, respectively. SEM analysis confirmed the DSC and TG analyses and showed significant increase in the nanowire number density for samples pretreated with 20% NaOH compared to 10% and 5% NaOH samples heated at 1100 °C/30 mins (Figure 3).

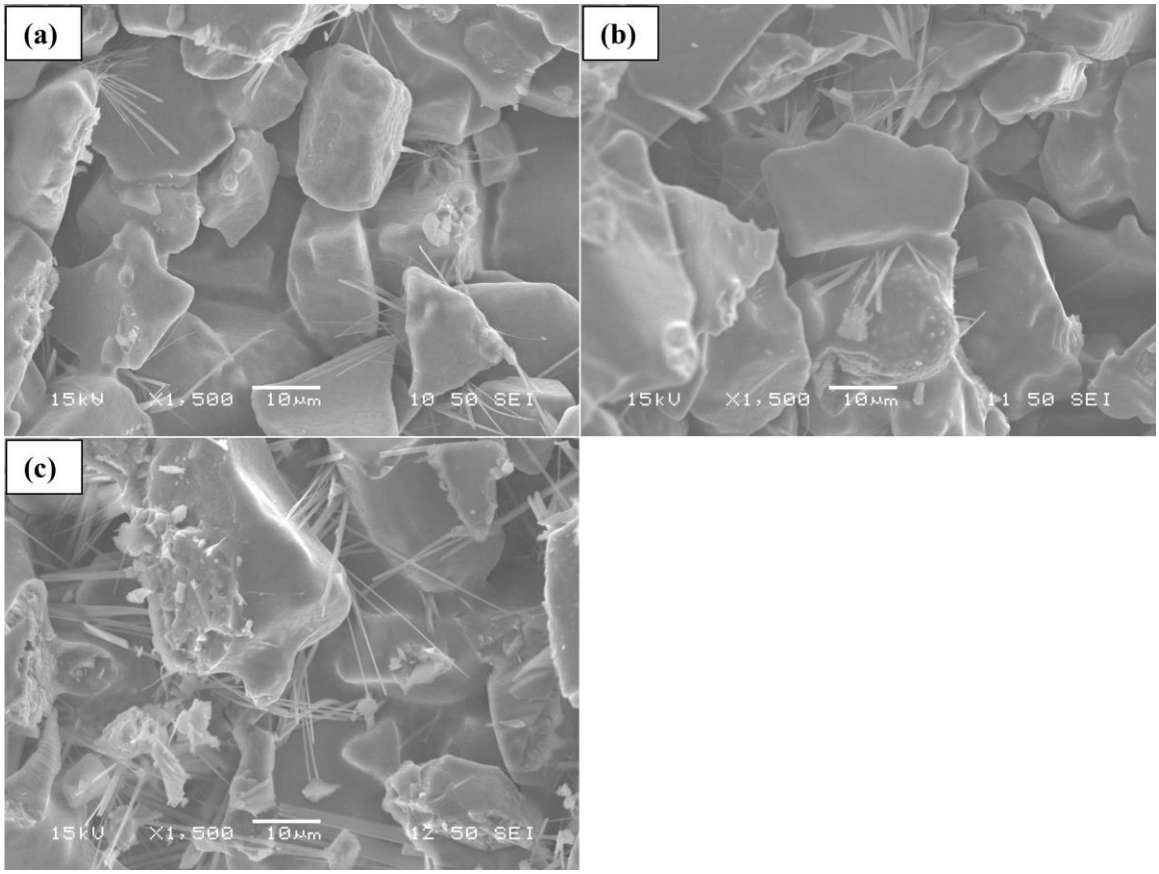

Figure 3: SEM analysis of DSC-TGA samples prepared by mixing 40 μm SiC with (a) 5%, (b) 10%, and (c) 20% NaOH, compacted at 0.47 MPa and heat treated to 1100 °C for 30 mins in air environment at a heating rate of 10 °C/min.

In conjunction with the differences in the nanowire's density, TG analysis showed a significant increase in weight gain. The rate of weight gain for all samples took place in two steps. The initial weight gain step took place in the temperature range 552-831 °C, 636-861 °C and 726-940 °C for sample pretreated with 5%, 10%, and 20% NaOH, respectively. The rate of weight gain in the first step increased with the increase in the concentration of NaOH in the order of 20.8 ug/min, 34.1 ug/min, and 77.76 ug/min for 5%, 10%, and 20% NaOH, respectively. The second weight gain step took place in the temperature range 831-1100 °C, 861-1100 °C, and 940-1100 °C for sample pretreated with 5%, 10%, and 20% NaOH, respectively. A similar trend in the rate of weight gain was also observed in the second step weight gain stage from TG analysis. The rate of weight gain in the second step increased with the increase in the concentration of

NaOH in the order of 44.13 ug/min, 48.75 ug/min, and 73.2 ug/min for 5%, 10%, and 20% NaOH, respectively. For the 20% NaOH constant rate in the two steps weight gain observed due to presence of thick silica gel that was deprived of oxygen as shown in our previous study, EDX analysis clearly revealed that the silica layer is oxygen deficient with Si/O ratio close to 1 [62, 63]. For the samples pretreated with 5% or 10% NaOH the weight gain increased in the second step (in the temperature range 831-1100 °C or 861-1100 °C) compared to the first step (in the temperature range 552-831 °C or 636-861 °C) due to the passive oxidation. Data in the literature showed that passive oxidation leads to weight gain due to the formation of a SiO_2 layer on the SiC surface through oxidation. The SiO_2 layer functions as a protective barrier, impeding further oxidation, and concurrently releases gaseous phases such as SiO (g) and CO (g) from the SiC material [105-107]. Therefore, in our work, the formation of silica gel layer by chemically attacking the SiC surface using NaOH solution, promoted passive oxidation that led to weight gain and densification upon heat treatment. The initial high rate of weight gain was due to oxygen diffusion into the oxygen deficient silica layer [62, 63]. As more oxygen diffusion took place the concentration gradient decreased, and the rate of diffusion also decreased. The DSC-TG analysis confirmed that the nucleation temperature is at 525.5 °C and crystallization temperature is at 800 °C. The analysis also confirmed that as the NaOH concentration increases, significant weight gain can be observed along with significant increase in nanowire number density. Based on the above analysis, the effect of NaOH concentrations and thermal treatment parameters for post processing stage of 3D printed SiC green body was investigated in the next sections of this thesis. The goal of this investigation is to determine the optimum parameters that facilitate nucleation and growth of secondary crystals at the SiC grain boundaries and enhance densification and mechanical properties.

2.2.2 Effect of NaOH concentration on nucleation and growth of the silica nanowire

SEM morphological analysis of fractured surface of 3D printed SiC discs impregnated in 5%, 10%, and 20% NaOH for 15 mins and heat treated at the nucleation temperature of 525 °C/20 mins is shown Figure 6. At 525 °C the SEM analysis showed the formation of silica droplets/nuclei on the SiC particle surface. Based on Figure 4, it is evident that the number of silica droplets or nuclei formed on the SiC particle surface increased with increase in NaOH concentrations.

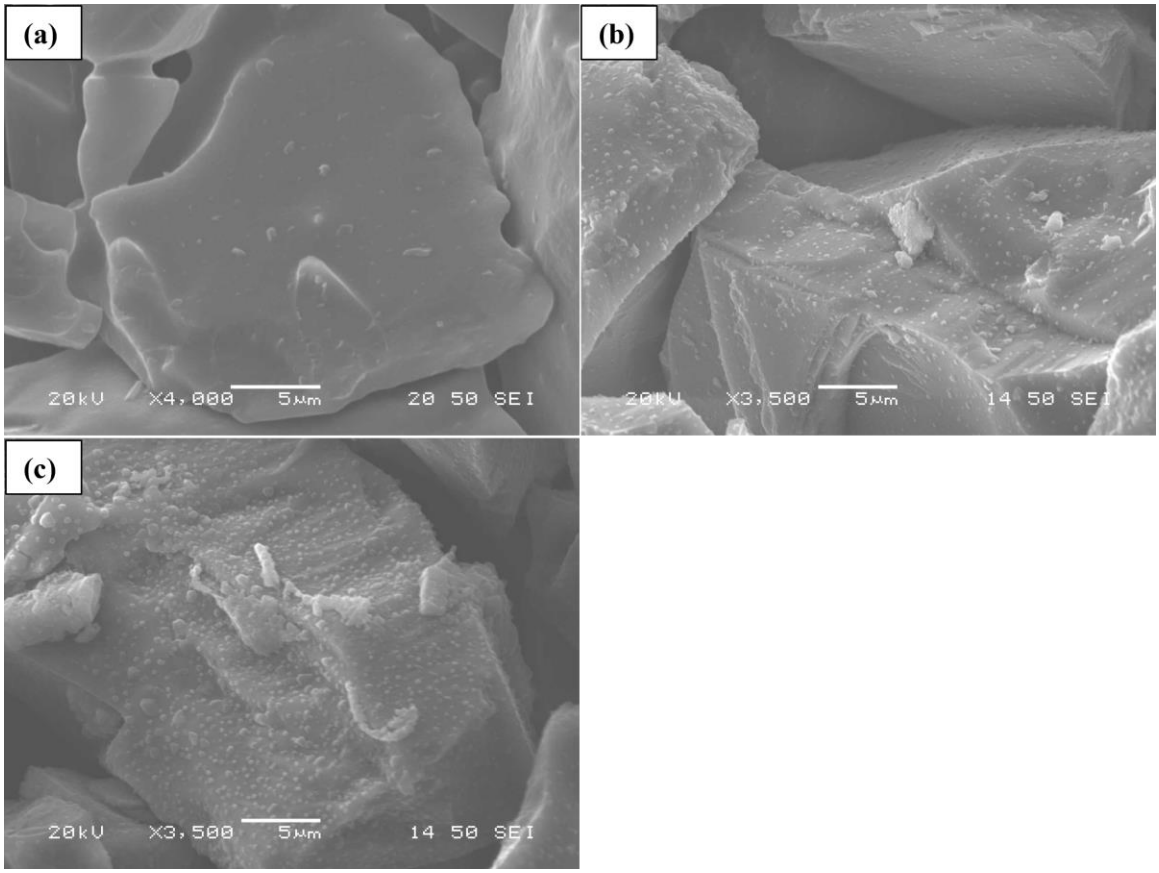

Figure 4: SEM analysis of fractured surface of 3D printed SiC discs impregnated in (a) 5%, (b) 10% and (c) 20% NaOH for 15 mins, heat treated at 525 °C/20 mins showing the droplets/ nuclei formation on the SiC particles surface.

A quantitative SEM analysis was performed on fractured surface of the 3D printed SiC disc impregnated in 5%, 10%, and 20% NaOH for 15 mins, subjected to a heat treatment at 525 °C for 20 mins for analyzing the silica droplets number density (mm-2) and % distribution of

silica droplets width groups as shown in Figure 5. The results revealed a significant increase in the average number of silica droplets per 1 mm^2 area with increasing NaOH concentration: 1906513 ± 602204 for 5% NaOH, 3626558 ± 523220 for 10% NaOH, and 4161277 ± 481338 for 20% NaOH (Figure 5a). Analysis of droplet width distribution showed a bimodal pattern for samples treated with 5%, 10%, and 20% NaOH, as shown in Figure 5b. In the case of 5% NaOH, the majority of silica droplets were within the 0.08 µm – 0.3 µm (38.54%) and 0.3 µm – 0.6 µm (52.17%) width groups. However, there was an observable shift in the distribution towards wider width groups (0.6 µm – 1 µm and 1 µm – 4.7 µm) with increasing NaOH concentration. Specifically, the percentage increased from 8.66% and 0.62% for 5% NaOH to 13.32% and 1.52% for 10% NaOH, and further to 18.84% and 7.33% for 20% NaOH, indicating a trend of silica droplets favoring larger width groups under higher NaOH concentrations. The observed percentage increase in the larger droplet width group, along with a concurrent decrease in the smaller width groups as NaOH concentration increases, can be attributed to the high density of silica droplets present in the sample. This increased droplet density facilitated the coalescence of smaller droplets, ultimately leading to the formation of larger droplets.

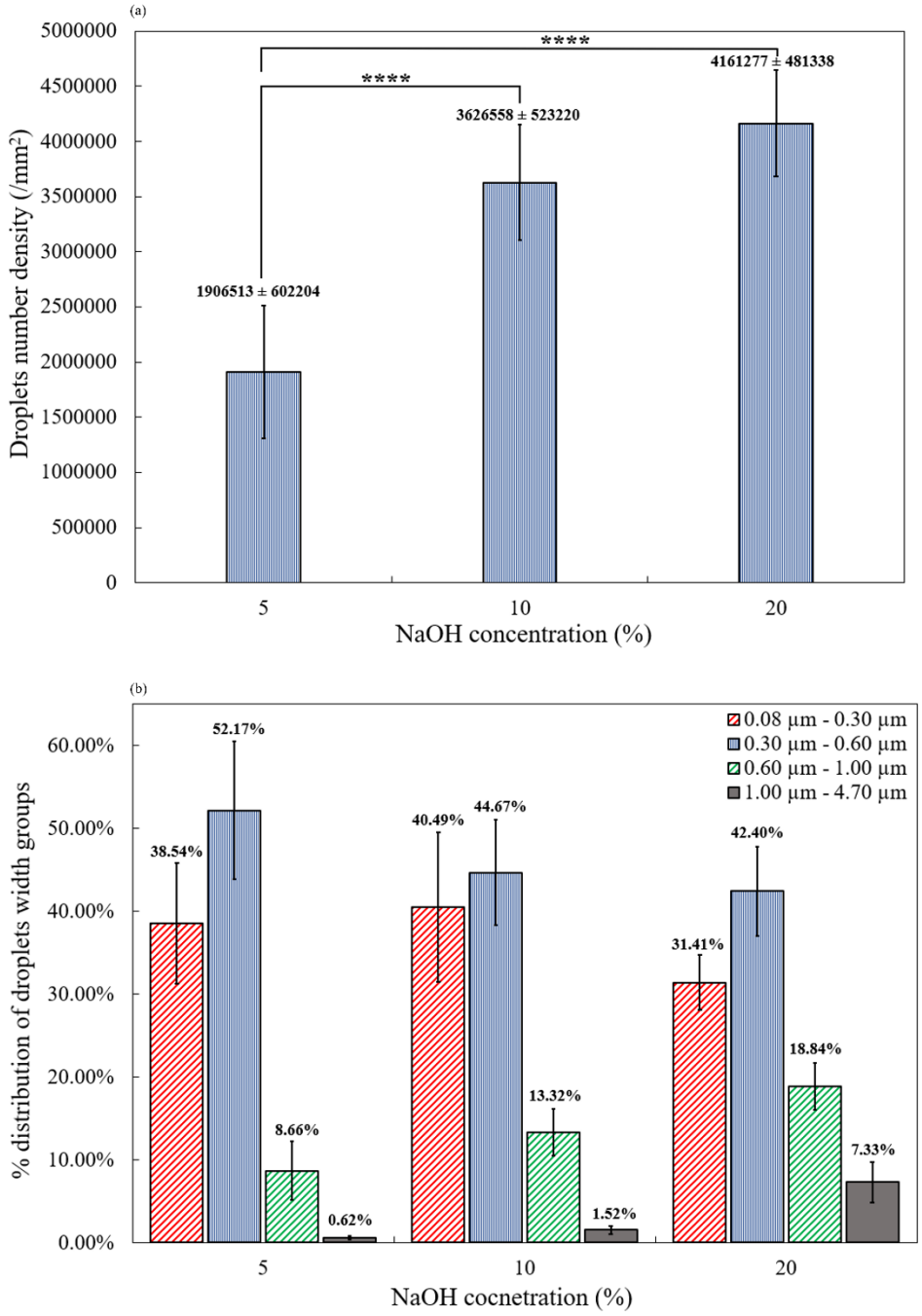

Figure 5: Quantitative SEM image analysis obtained from the fractured surface of 3D SiC discs showing the change in (a) silica droplets number density (mm^{-2}), and (b) % distribution of droplets width groups for 5%, 10% and 20% NaOH concentrations. (****P<0.0001.)

SEM morphological analysis of fractured surface of 3D printed SiC discs impregnated in 5%, 10%, and 20% NaOH for 15 mins and heat treated at 550 °C/6 hr followed by a heat treatment at crystallization temperature of 800 °C/2 hr is shown Figure 6. The number of

nanowires present inside the pore of the 3D printed SiC discs and size of the nanowires increased with increase in NaOH concentrations.

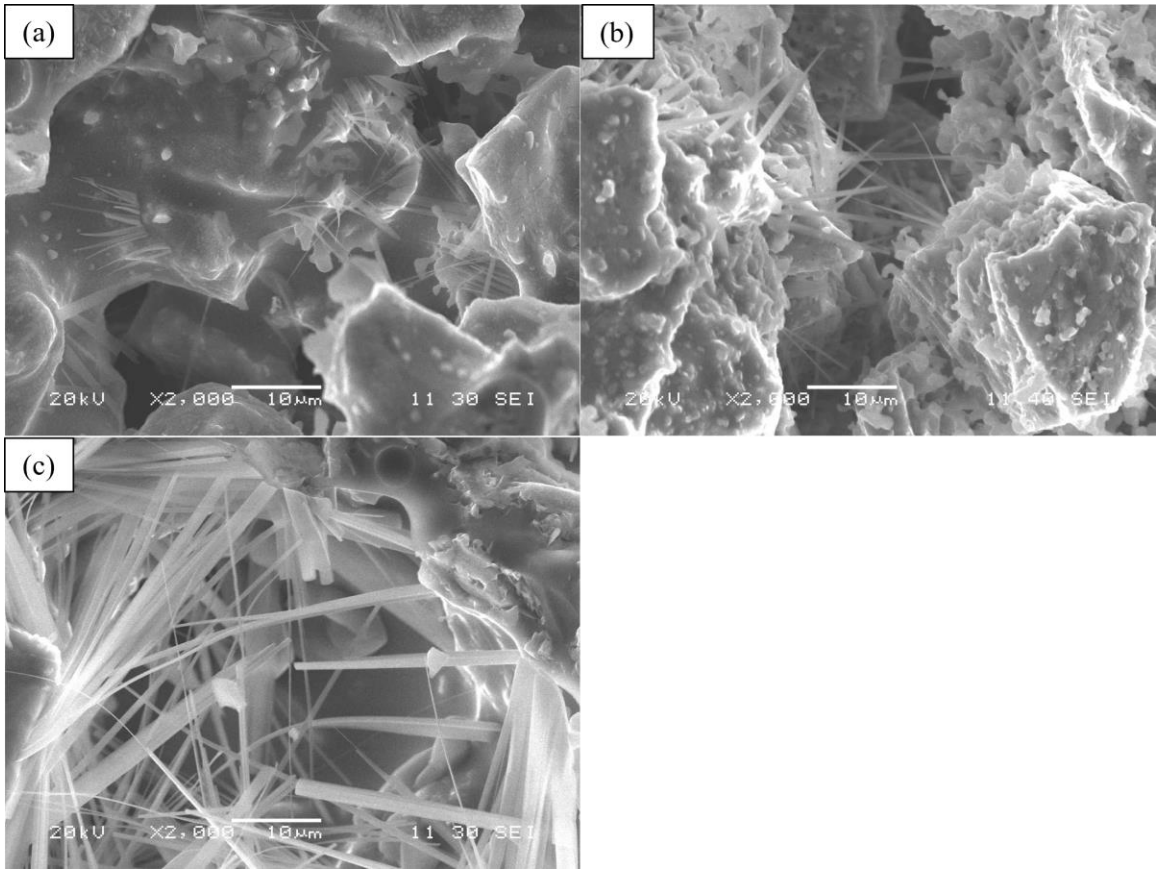

Figure 6: SEM analysis of fractured surface of 3D printed SiC discs impregnated in (a) 5%, (b) 10% and (c) 20% NaOH for 15 mins, heat treated at 550 °C/6 hr followed by heat treatment at 800 °C/2 hr in air environment at a heating rate of 1 °C/min. The number and size of the nanowires increase as NaOH concentration increases from 5% to 10% or 20%.

Figure 7 shows the quantitative SEM image analysis performed on the fractured surface of 3D SiC discs showing the change in silica nanowire number density (mm^{-2}), % distribution of nanowire width groups, and average length of the nanowire for 5%, 10%, and 20% NaOH concentrations. The ImageJ software analysis of the fracture surface showed a statistically significant higher number density of nanowires in the samples impregnated in 20% NaOH compared to 5% or 10% NaOH (Figure 7a). Here, the increased number of silica nanowire crystals in the 20% NaOH is attributed to the high number of silica droplets or nuclei formation

in the sample as demonstrated in Figure 4 and Figure 5a. The nucleation process is enhanced by the presence of Na ions as well as the hydroxyl groups present in the silica gel layer. The nanowire number density (mm^{-2}) as well as the width and length distribution of the nanowires increased according to the concentration of the NaOH used to pretreat 3D printed SiC in the order 20% > 10% > 5% (Figure 7b and Figure 7c). While a bimodal distribution of nanowire width was observed for samples pretreated with 5% and 10% NaOH, the 20% NaOH samples showed three distinct ranges of nanowire's width. The majority of silica nanowires width found in samples impregnated in 5% NaOH was in the range from 0.08 µm to 0.3 µm and from 0.3 µm to 0.6 µm whereas for 10% NaOH the nanowire width was found mostly in bigger range 0.3 µm – 0.6 µm and 0.6 µm – 1 µm (Figure 7). For 3D printed SiC discs pretreated with 20% NaOH concentration, the width distribution of the nanowires was 31.75% (0.3 µm – 0.6 µm), 24.69% (0.6 µm – 1 µm), and 24.10% (1 µm – 4.7 µm). The increase in nanowire width ranges (20% > 10% > 5%) is attributed to the presence of a high number of silica droplets on the SiC particles as shown in Figure 5a. When the number density of silica droplets increases for 10% or 20% NaOH concentrations, more droplet-droplet coalescence occurred, resulting in an increased droplet size (Figure 5b). This, in turn, resulted in wider nanowire formation, particularly pronounced for higher NaOH concentrations suggesting that the width of the nanowire is directly related to the width of silica droplet. The average nanowire length measurement showed statistically significant increase in nanowire length, 41 ± 7 µm for 20% NaOH compared to 8 ± 1.2 µm for 5% NaOH or 12.6 ± 3.2 µm for 10% NaOH. The increase in the nanowire's length could be attributed to the increase amount in SiO and $Si(OH)_4$ vapors released from the silica gel layer [62, 63] and participate in the growth of nanowires.

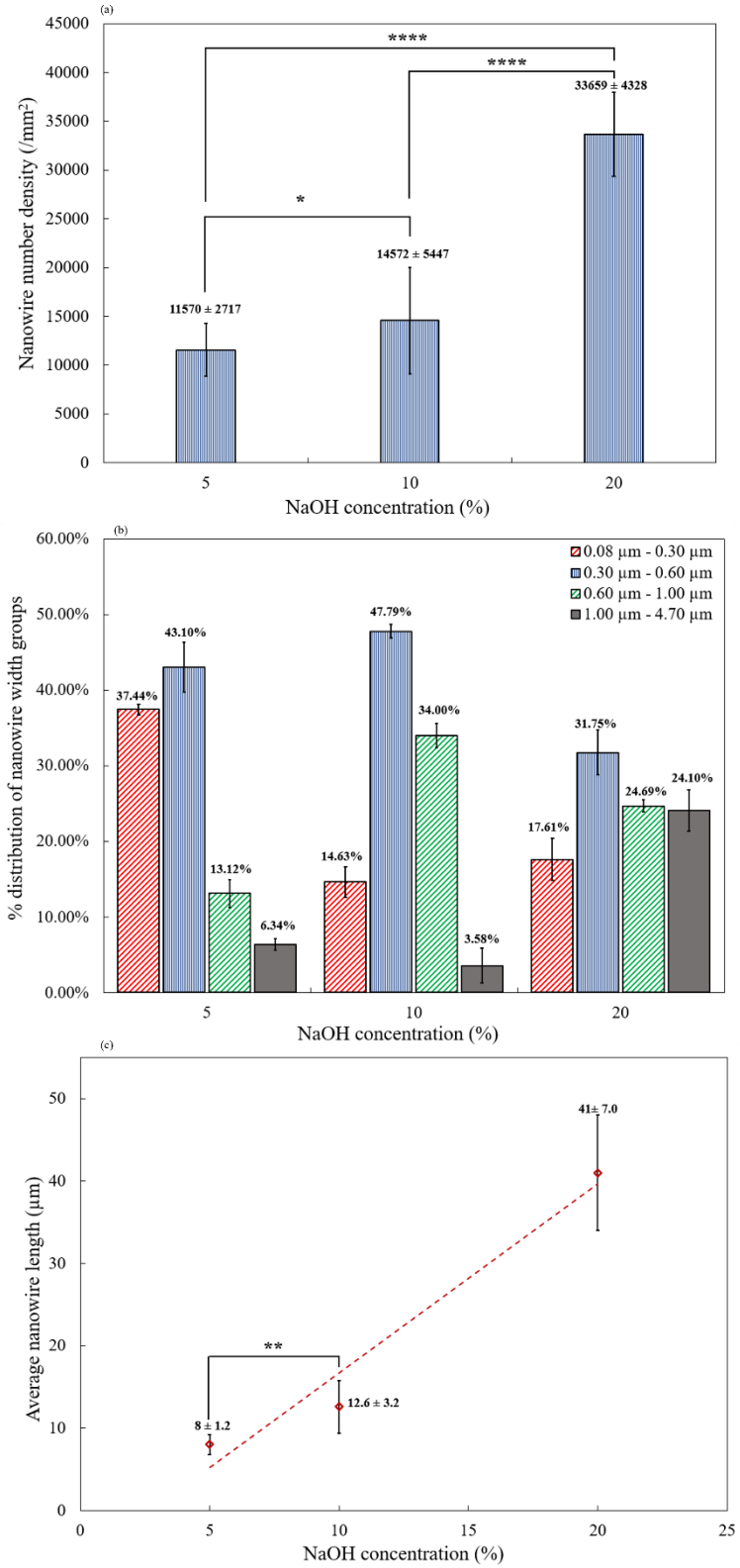

Figure 7: Quantitative SEM image analysis obtained from the fractured surface of 3D SiC discs showing the change in (a) silica nanowire number density (mm^{-2}), (b) % distribution of nanowire width groups, and (c) average length (µm) of the nanowire for 5%, 10% and 20% NaOH concentrations. (*P<0.05, **P<0.01 and ****P<0.0001.)

2.2.3 Effect of NaOH concentration on the width of the silica bonding zone between SiC particles

Figure 8 illustrates the average width of the silica bonding zone that fuses SiC particles together, as measured from SEM micrographs captured on the fractured surface of 3D printed SiC discs treated with varying NaOH concentrations ranging from 5% to 20%. The result showed a gradual increase in the average width of the silica bonding zone. Specifically, for samples impregnated in 5% NaOH, the width increased from 4.87 ± 1.94 μm to 5.08 ± 1.62 μm for 10% NaOH and further to 5.41 ± 2.11 μm for 20% NaOH. However, statistical analysis did not reveal a significant difference. Treating SiC with NaOH breaks the SiC bonds, resulting in the formation of a silica gel layer enriched in Si-O bonds. This silica layer acts as a binder for the SiC particles. Samples treated with a higher concentration of NaOH led to a larger amount of silica layer, contributing to the observed increase in the width of the silica bonding zone along with increased nanowire growth.

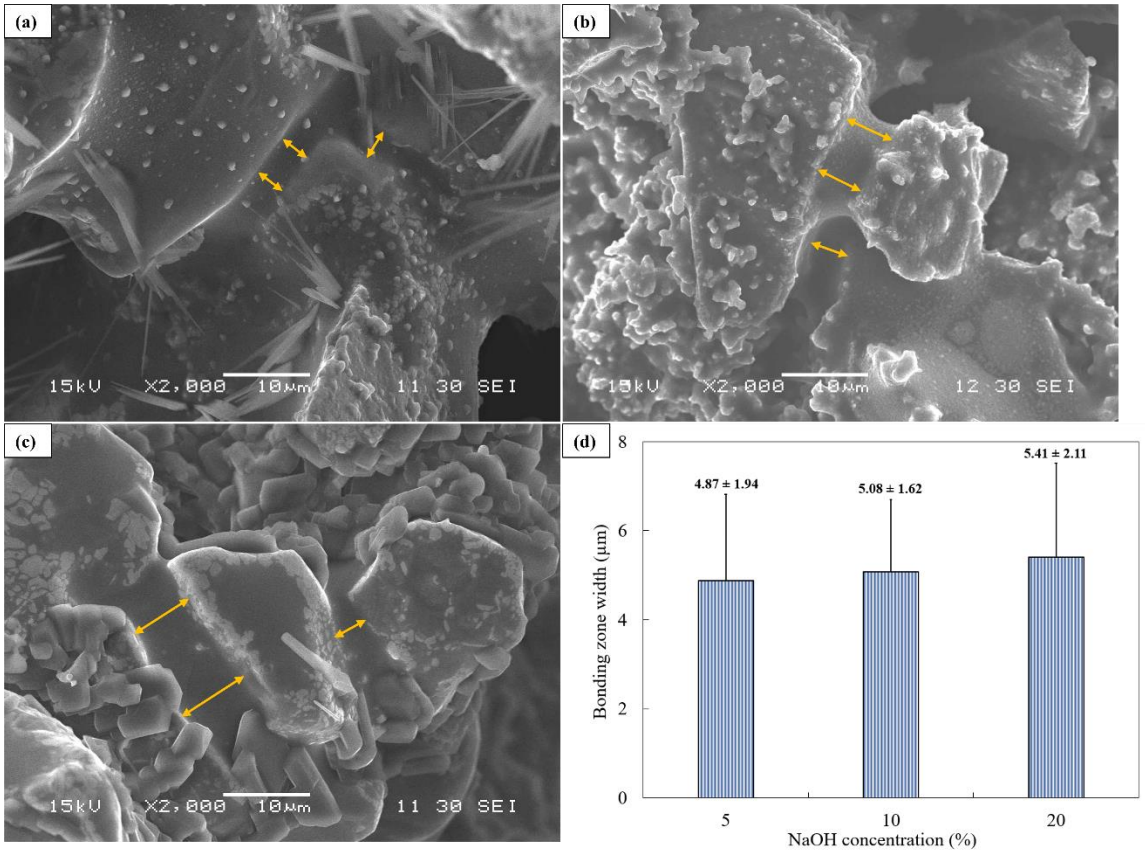

Figure 8: SEM analysis of fractured surface of 3D printed SiC discs impregnated in (a) 5%, (b) 10%, and (c) 20% NaOH for 15 mins, heat treated at 550 °C/6 hr followed by heat treatment at 800 °C/2 hr in air environment at a heating rate of 1 °C/min. The yellow arrows show the silica bonding zone fusing the SiC particles together. (d) Average bonding zone thickness obtained from quantitative SEM performed for 5%, 10%, and 20% NaOH concentrations.

2.2.4 Effect of nanowires growth and the width of the silica bonding zone between SiC particles on compressive strength and modulus of elasticity

Figure 9(a-c) shows the representative stress-strain curves generated from compression test performed on 3D printed SiC discs impregnated in 5%, 10%, and 20% NaOH for 15 mins, heat treated at 550 °C/6 hr followed by heat treatment at 800 °C/2 hr. The measurement of mechanical properties revealed a notable enhancement in compressive strength and compression modulus of elasticity with increasing NaOH concentration, as illustrated in figure 9(d). Specifically, compressive strength measurements exhibited a statistically significant ($P < 0.005$) increase in the mechanical strength of 11.33 ± 2.52 MPa for 3D printed SiC samples (n=7)

impregnated in 20% NaOH in comparison with samples impregnated in 5% or 10% NaOH and heat treated at 550 °C/6 hr and 800 °C/2 hr as shown in figure 9(d). The significant improvement in the strength of the 3D printed SiC discs subjected to higher NaOH concentration can be attributed to several factors; (i) significant increase in the silica nanowire number density, (ii) the dimensions of the nanowires facilitating bridging within pores and densification of the material, and (iii) increase in the width of silica bonding zone, contributing to heightened mechanical properties.

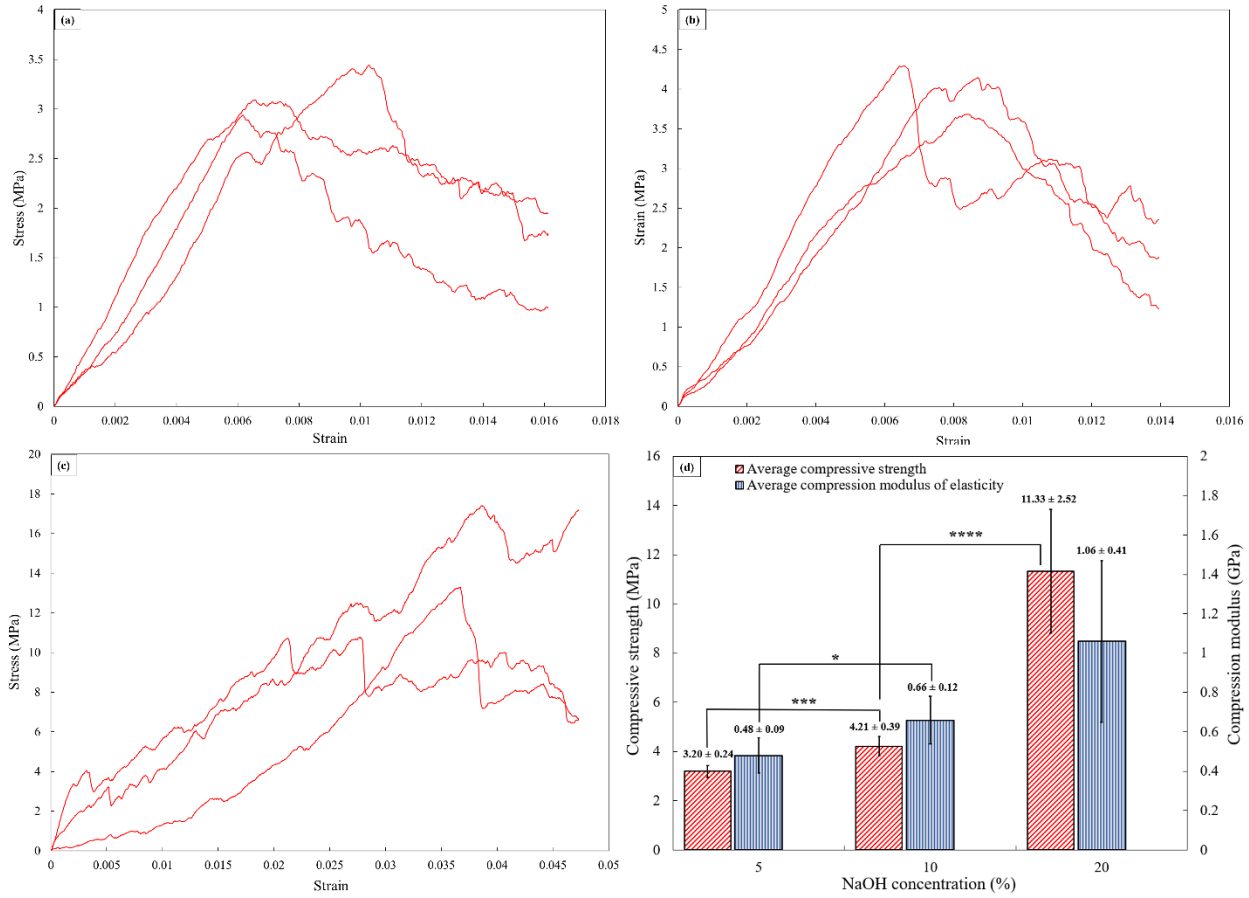

Figure 9: (a), (b), and (c) Stress-strain curves of 3D printed SiC discs impregnated in 5%, 10%, and 20% NaOH and heat treated at 550 °C/6hr and 800 °C/2hr in air environment at a heating rate of 1 °C/min. (d) Mechanical properties of samples with varying concentrations of NaOH solution. (*P<0.05, ***P<0.001 and ****P<0.0001.)

2.2.5 Effect of NaOH concentrations on the dimensional stability of the 3D printed discs

However, the dimensional stability analysis of 3D printed SiC samples (n=7) impregnated in 5%, 10%, and 20% NaOH and subjected to heat treatment at 550 °C/6 hr and 800

°C/2 hr showed significant change in sample's diameter and height for 20% NaOH compared to 5% or 10% NaOH (Figure 10). This can be explained by the very fact that NaOH attacks the Si-C bond and forms silica gel layer on the SiC particle surface and silica gel thickness increases as the NaOH concentration increases. In our previous study, XRD analysis of SiC discs pretreated with 20 % NaOH and heat treatment at 800 °C/2 hr showed the formation of α-SiC as the main phase with the presence of cristobalite phase [62, 63]. Hence, the % amount of cristobalite phase formation increases as the NaOH concentration increases [64]. The co-efficient of thermal expansion (CTE) of pure cristobalite (17.5×10^{-6}/K at 20 – 1000 °C) has huge mismatch with that of SiC (4.7×10^{-6}/K at 20 – 700 °C) [108]. This huge mismatch can lead to incompatible volume change resulting in large deformation of the samples upon cooling. Therefore, the formation of high quantity of cristobalite phase using 20% NaOH showed large deformation compared to 5% or 10% NaOH.

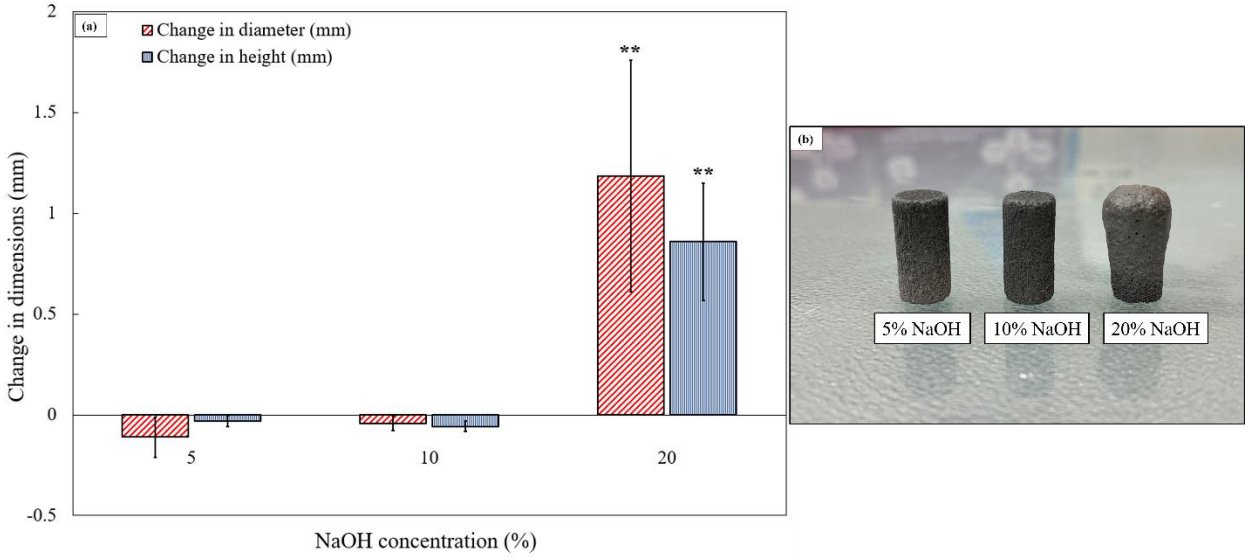

Figure 10: (a) Dimensional stability, and (b) digital image, of 3D printed SiC discs impregnated in 5%, 10%, and 20% NaOH and heat treated at 550 °C/6hr and 800 °C/2hr in air environment at a heating rate of 1 °C/min. (** sign indicates P<0.01.)

2.2.6 Effect of NaOH concentrations on the apparent density and porosity of the 3D printed discs

Apparent density and porosity analysis showed a significant ($P < 0.005$) decreases in the density and porosity for 3D printed SiC samples (n=7) impregnated in 20% NaOH in comparison with samples impregnated in 5% or 10% NaOH as shown in Figure 11. The significant reduction in porosity with respect to NaOH concentration is attributable to the increased nanowire number density and nanowires' growth as measured by nanowire length and width which fill up the pore of the 3D printed SiC discs. Theoretically when the percent porosity decreases, it leads to an increase in density. However, in this study the opposite trend was found for the density of 3D printed SiC discs subjected to different NaOH concentration. As the NaOH concentration increased from 5% to 20%, density of the samples decreased from 2.63 gcm^{-3} to 2.15 gcm^{-3}. This can be explained by the phases present in the sample. As discussed earlier, the phases present in the sample after heat treatment are α-SiC and cristobalite and the density of pure phases of SiC and cristobalite are 3.2 gcm^{-3} and 2.65 gcm^{-3}. Moreover, as the NaOH concentration increases, the amount of cristobalite phase present in the sample also increases resulting in a decrease in the overall density of the sample.

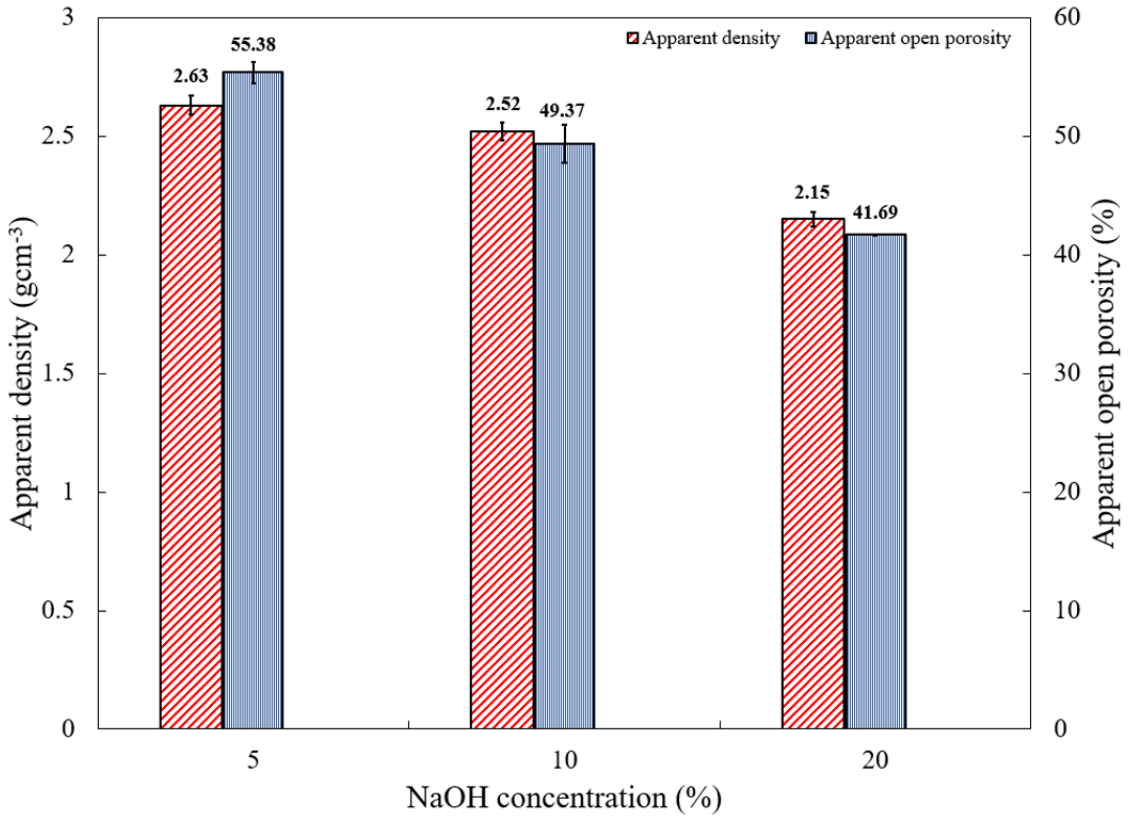

Figure 11: Comparison of apparent density and apparent porosity % of 3D printed SiC discs impregnated in 5%, 10%, and 20% NaOH concentration respectively for 15 mins and subjected to heat treatment at nucleation temperature 550 °C/6 hr and sintering temperature at 800 °C/ 2 hr.

Since 3D printed SiC samples impregnated in 20% NaOH concentration demonstrated low dimensional stability, we have excluded 20% NaOH concentration from further analysis. Good dimensional stability was found for both 5% and 10% NaOH, however the samples impregnated in 10% NaOH showed higher strength than 5% NaOH due to the increased number in silica nanowire density and increased thickness of the bonding zone. Therefore, 10% NaOH was selected for further analysis related to analyzing the effect of sintering temperature and dwelling time.

2.2.7 Effect of sintering temperature on the silica nanowire growth

SEM morphological analysis of fractured surface of 3D printed SiC discs impregnated in 10% NaOH for 15 mins and heat treated at 550 °C/6 hr followed by a second heat treatment at

various sintering temperature ranging from 800 °C/2 hr to 1200 °C/2 hr is shown in Figure 12. As shown in Figure 12(a-d), number of nanowires present inside the pore of 3D printed SiC disc and the size of nanowire increased when sintering temperature increased from 800 °C/2 hr to 1100 °C/2 hr. When the sintering temperature was further increased to 1200 °C/2 hr, the number of nanowires present inside the pore of 3D printed SiC disc and size of nanowire showed a decrease (Figure 12e).

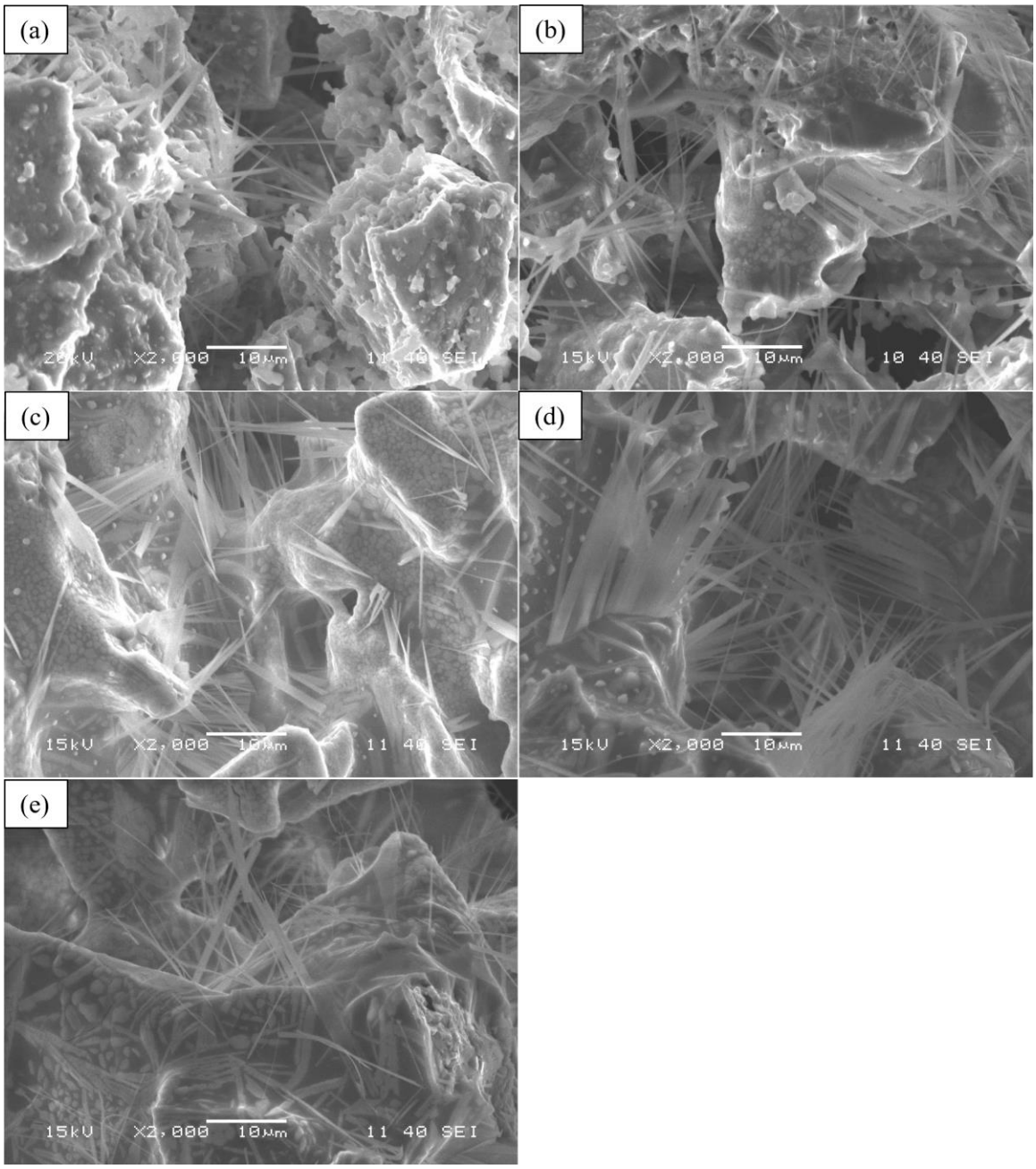

Figure 12: SEM analysis of fractured surface of 3D printed SiC discs impregnated in 10 % NaOH for 15 mins, heat treated at 550 C/6hr and sintered at (a) 800 °C/2 hr, (b) 900 °C/2 hr, (c) 1000 °C/2 hr, (d) 1100 °C/2 hr, and (e) 1200 °C/2 hr in air environment at a heating rate of 1 °C/min.

As Figure 12 showed that the number of nanowires present inside the pore of 3D SiC increased when sintering temperature was increased to 1100 °C and then decreased as the temperature was raised to 1200 °C, was confirmed by the quantitative SEM image analysis performed on the fractured surface of 3D SiC discs as shown in Figure 13a. Nanowire number

density (mm^{-2}) measurement showed a gradual increase with respect to sintering temperature from 800 °C to 1100 °C and showed highest number density of 49698 ± 6767 mm^{-2} at 1100 °C/2 hr. The goal of this thesis is to find the required post processing parameters for optimum nanowire growth and number density. Therefore, the sample heat treated at 1200 °C/2 hr was excluded from the quantitative SEM image analysis for measuring the nanowire width and length at various sintering temperatures since at 1200 °C nanowire number density decreased as shown in Figure 13a. Interestingly, the % distribution of nanowire width groups showed same size distribution for sintering temperatures varying from 800 °C to 1100 °C (Figure 13b). The majority of nanowires were found in 0.3 µm – 0.6 µm width groups. This analysis revealed that the nanowire width is independent of post processing parameters rather it is directly related to the size of the droplets. To confirm the above claim droplet size analysis was performed as shown in Figure 14. The average nanowire length measurement showed a linear increase in nanowire length from 12.6 ± 3.2 µm at 800 °C to 20.5 ± 3.2 µm at 1100 °C (Figure 13c). The increase in the nanowire's length could be attributed to the increased oxidation of the SiO with the increase in sintering temperature and its subsequent condensation as SiO_2 molecules. The TG analysis for 10% NaOH concentration showed a large weight again in the temperature range from 861 °C to 1100 °C as discussed in section 3.1. The noticeable weight gain with the rising temperature of the SiC discs suggests the dominant effect of oxidation. This signifies that the oxidation process of SiO, along with the subsequent condensation into silica (SiO_2) nanowires, played a significant role in the observed weight gain.

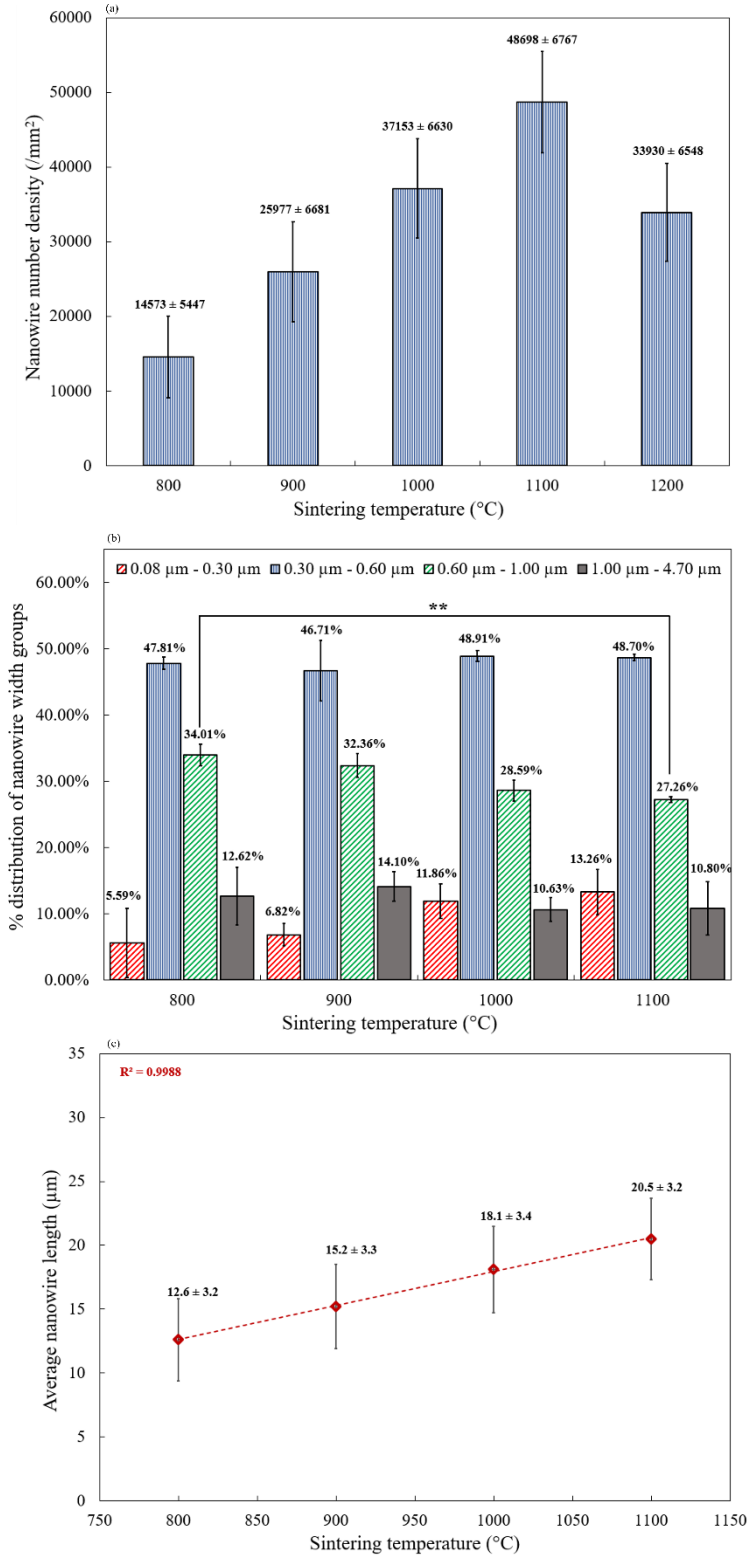

Figure 13: Quantitative SEM image analysis obtained from the fractured surface of 3D SiC discs showing the change in (a) silica nanowire number density (mm^{-2}), (b) % distribution of nanowire width groups, and (c) length of the nanowire for different sintering temperatures at 800 °C, 900 °C, 1000 °C, and 1100 °C for 2hr. (** sign indicates $P<0.01$.)

Figure 14(a and b) show the SEM images for 3D printed SiC discs impregnated in 10 % NaOH for 15 mins and heat treated at 525 °C/20 mins and 600 °C/20 mins. As shown in Figure 14(a and b) various sizes and shapes of silica droplets were found. At 525 °C the width of the droplets appears to be smaller than the droplets formed at 600 °C. At 600 °C due to increase in the thermal energy fusion of multiple droplets led to the formation of larger droplets which is evident by the presence of concave structures in the SEM image (Figure 14) suggesting the merging region of two adjacent droplets. As expected, the quantitative SEM image analysis (Figure 14c) for droplets size distribution measurement showed good agreement with the above observation. Sample heat treated at 600 °C, majority of droplets were found in bigger size range from 0.3 µm to 0.6 µm and from 0.6 µm to 1 µm whereas at 525 °C range varied from 0.08 µm to 0.3 µm and from 0.3 µm to 0.6 µm as shown in Figure 14c. The % distribution of droplets size groups at 600 °C showed similar size distribution as nanowire width groups found at different sintering temperatures as shown in Figure 13b. These measurement analyses suggest that the width of nanowires was directly related to the size of the silica droplets (Figure 14c).

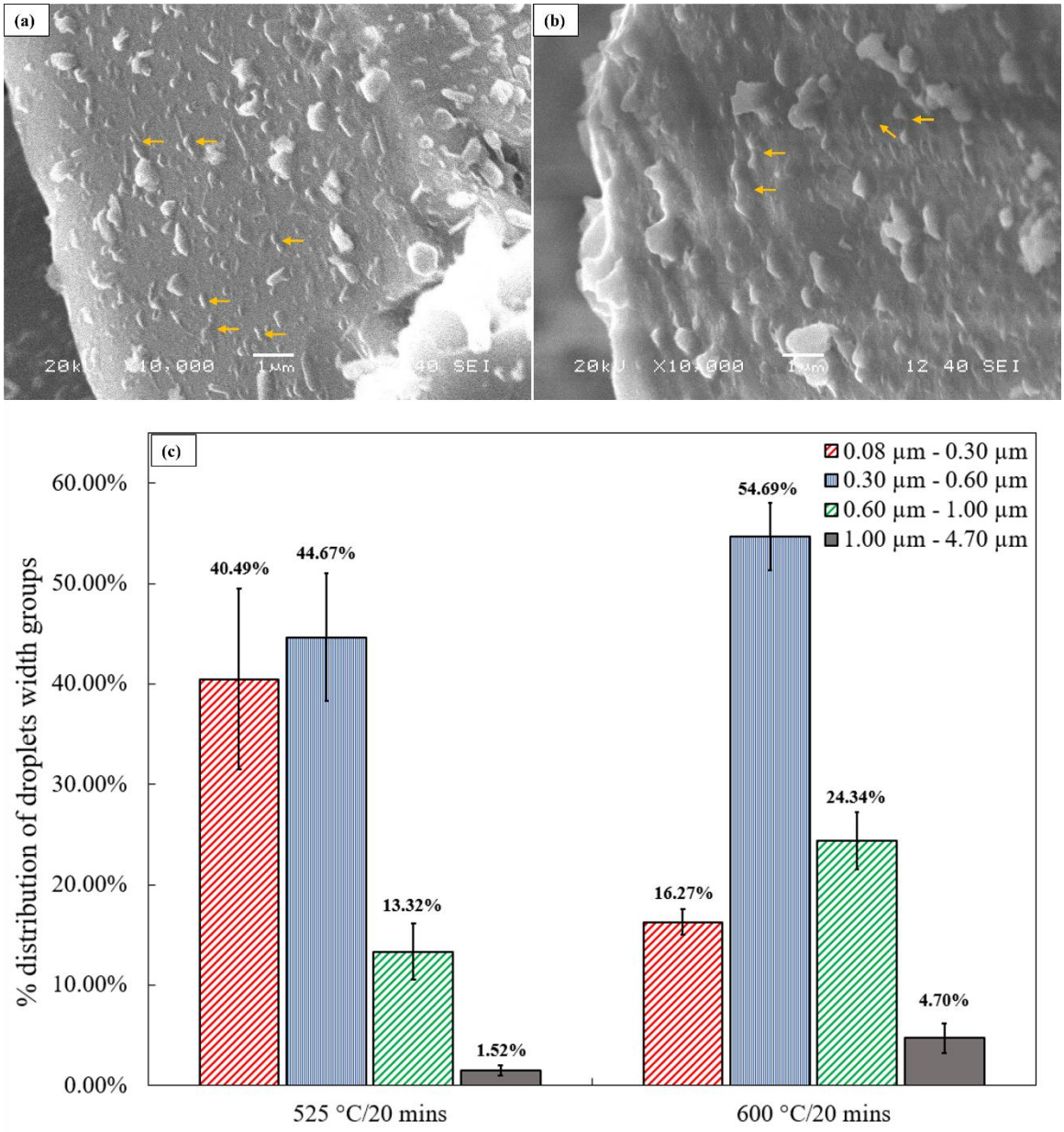

Figure 14: 3D printed SiC disc impregnated in 10% NaOH and heat treated at different temperatures; (a) 525 °C/20 mins, (b) 600 °C/20 mins SEM photographs, and (c) % distribution of droplet size groups obtained for 525 °C/20 mins, and 600 °C/20 mins. The yellow arrows show the merging of droplets into bigger droplets.

It was found from this study that the optimum post processing temperature for 3D printed SiC disc green body was 1100 °C for 10% NaOH concentration which facilitated nucleation and growth of secondary crystals at the SiC grain boundaries and enhanced densification of the sample. Therefore, to analyze the effect of dwelling time on nanowire growth and mechanical

properties, post processing was performed on 3D printed SiC disc impregnated in 10% NaOH and sintering temperature was kept constant at 1100 °C while varying the dwelling time.

2.2.8 Effect of dwelling time on the silica nanowire growth

SEM morphological analysis of fractured surface of 3D printed SiC discs impregnated in 10% NaOH for 15 mins and heat treated at 550 °C/6 hr followed by a second heat treatment at 1100 °C for different dwelling times such as 2 hr, 4 hr, 6 hr, and 8 hr is shown Figure 15. As shown in Figure 15(a and b) the number of nanowires present inside the pore of 3D printed SiC disc and the length of the nanowires increased bridging the pores inside the SiC particles when dwelling time increased from 2 hr to 4 hr at 1100 °C. On the other hand, when the dwelling time was further increased to 6 hr or 8 hr at 1100 °C, the number of nanowires present inside the pore of 3D printed SiC disc as well as length of nanowire showed decrease (Figure 15(c and d)).

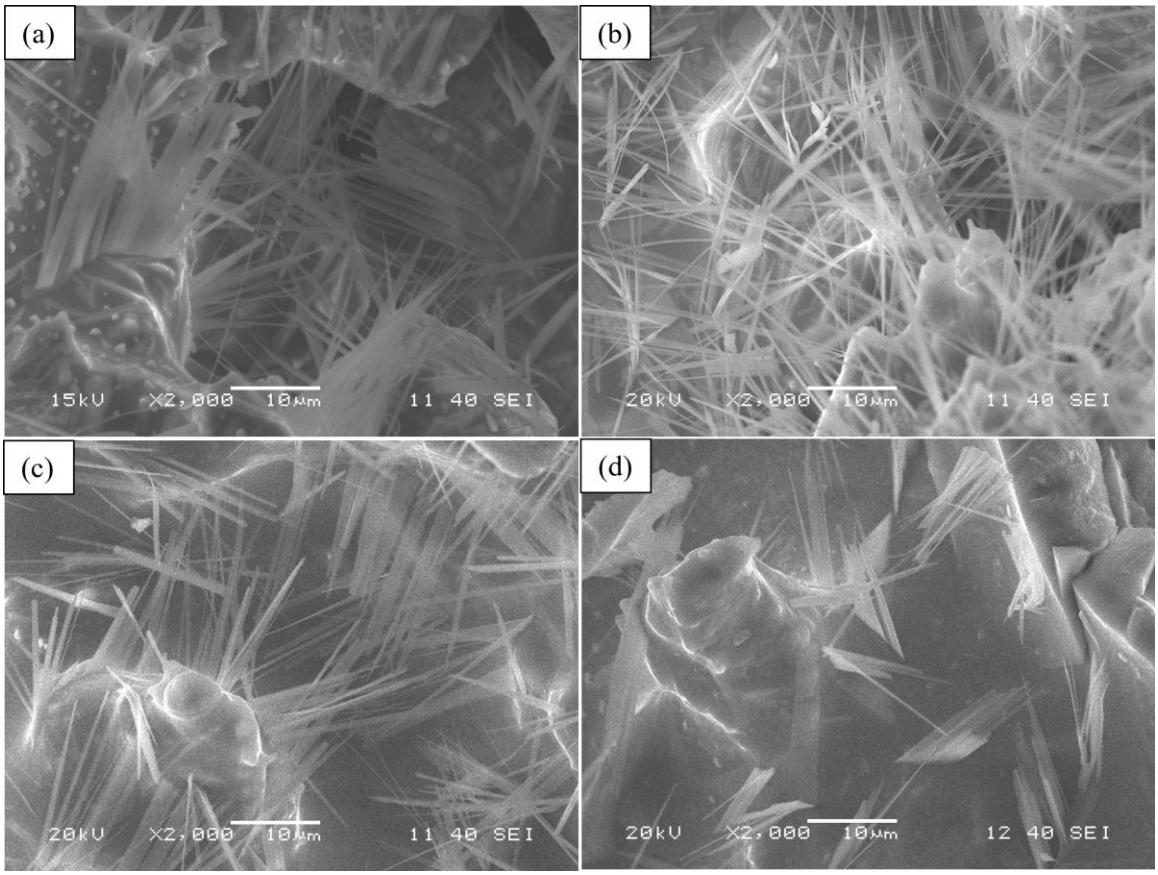

Figure 15: SEM analysis of fractured surface of 3D printed SiC discs impregnated in 10% NaOH for 15 mins, heat treated at 550 °C/6 hr and sintered at 1100 °C for (a)2 hr, (b)4 hr, (c)6 hr, and (d)8 hr in air environment at a heating rate of 1 °C/min.

Figure 16 shows the quantitative SEM image analysis performed on the fractured surface of 3D SiC discs impregnated in 10% NaOH showing the change in silica nanowire number density (mm^{-2}), % distribution of nanowire width groups, and average length of the nanowire at 550 °C/6hr and 1100 °C for 2 hr, 4 hr, 6 hr, and 8 hr. Figure 16a demonstrates that the nanowire number density (mm^{-2}) measured at 1100 °C/4 hr is significantly higher than that of sample treated, at 1100 °C/2 hr, and 1100 °C/8 hr. Moreover, the sample treated at 1100 °C/6 hr showed a decrease in nanowire number density (51704 ± 6853 mm^{-2}) compared to 1100 °C/4 hr (55431 ± 9232 mm^{-2}). However, the difference is not statistically significant. The quantitative SEM image analysis for measuring the nanowire width and length at different dwelling times was performed only for sample treated at 1100 °C/2 hr and 1100 °C/4 hr since 1100 °C/6 hr and 1100 °C/8 hr

showed decrease in nanowire number density (mm^{-2}) as shown in Figure 16a. The % distribution for nanowire width groups analysis for sample treated at 1100 °C/4 hr showed a significant 14.47% increase in number of nanowires in the width range from 0.08 µm – 0.3 µm and 5.34% and 6.55% decrease in the width range from 0.3 µm – 0.6 µm and 0.6 µm – 1 µm respectively compared to sample treated at 1100 °C/2 hr (Figure 16b). The increase in the number of narrow nanowire and decrease in the wider nanowire number present in the sample as the dwelling time increased, can be attributed to transformation of new droplets into nanowire due to increased thermal energy and partial melting of the wider nanowire due to prolong heat treatment duration. On the other hand, the average nanowire length measured for sample treated at 1100 °C/4 hr showed a significant increase in nanowire length from 20.5 ± 3.2 µm at 1100 °C/2 hr to 25.6 ± 3.3 µm as shown in Figure 16c. This is due to the longer oxidation process which generated more SiO_2 molecules that were readily available for deposition on the nanowire top surface resulted in the increased length of the nanowire.

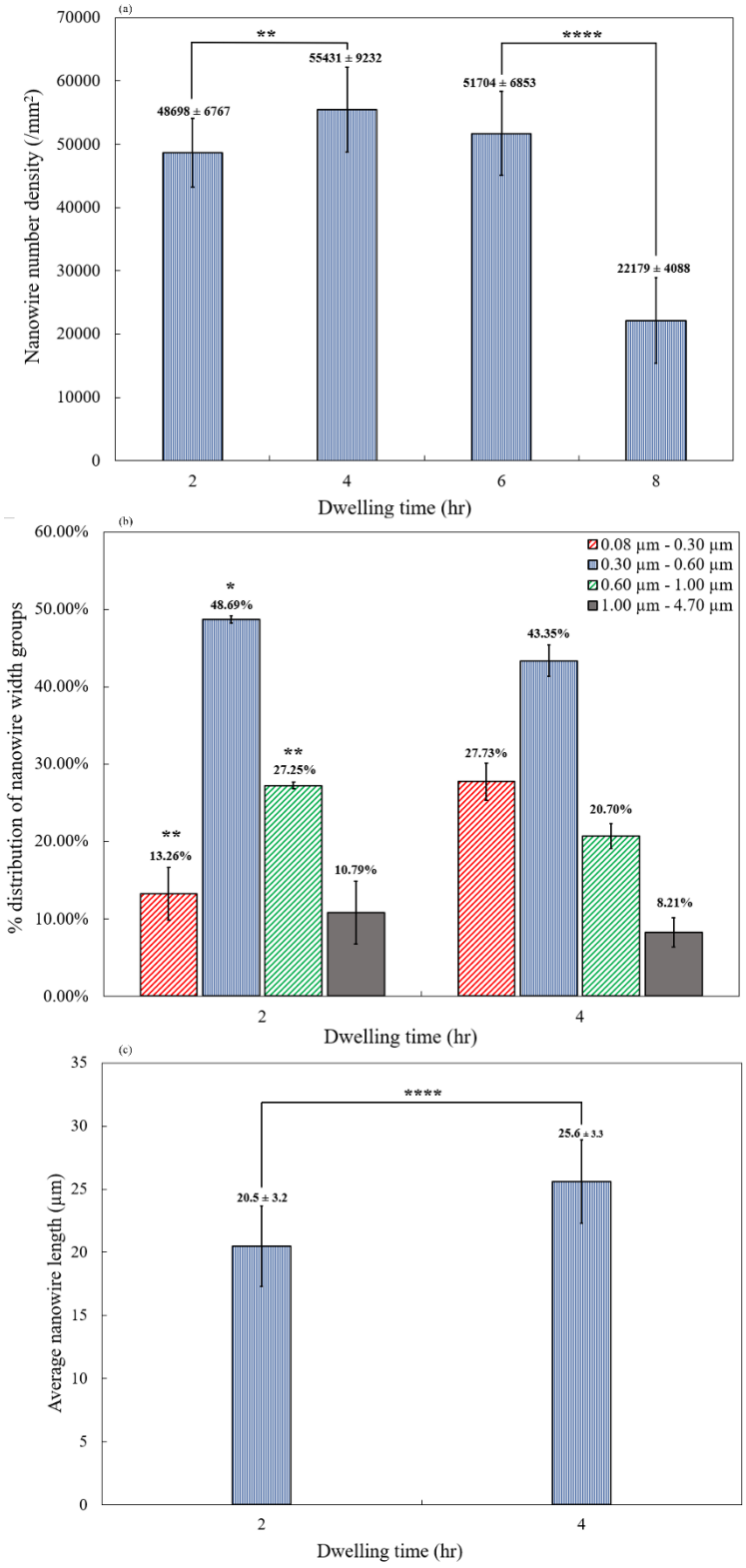

Figure 16: Quantitative SEM image analysis obtained from the fractured surface of 3D SiC discs showing the change in (a) silica nanowire number density (mm^{-2}), (b) % distribution of nanowire width groups, and (c) length of the nanowire for various dwelling times; 2 hr, 4 hr, 6 hr, and 8 hr at 1100 °C. (*P<0.05, **P<0.01 and ****P<0.0001.)

2.2.9 Compressive strength measurement

Figure 17 presents a comparative analysis of the average compressive strength, compression modulus of elasticity, and dimensional stability of 3D printed SiC discs. These discs were impregnated in 10% NaOH concentration for 15 minutes and then subjected to heat treatment at the nucleation temperature, 550 °C/6 hr, and various sintering temperatures: 800 °C/2 hr, 900 °C/2 hr, 1000 °C/2 hr, 1100 °C/2 hr, and 1100 °C/4 hr in an air environment with a heating rate of 1 °C/min. In this investigation, compressive strength and compression modulus of elasticity measurements exhibited a significant ($P < 0.03$) increase for samples subjected to heat treatment at 1100 °C/4 hr compared to those treated at various other sintering temperatures (Figure 17a). Furthermore, dimensional stability analysis revealed comparable stability among all the samples (Figure 17b). Notably, the dimensional stability of discs prepared using silica gel-coated SiC particles represents a substantial advantage over traditional sintering methods, which are prone to disc shrinkage due to grain boundary fusion and weight loss from carbon burning at elevated temperatures [109]. On the other hand, the pre-formation of a silica gel layer on SiC surfaces guided the oxidation mechanism to grow silica nanowires on the SiC surface, filling the pores and increasing strength while maintaining dimensional stability. Another plausible explanation for the enhanced mechanical properties could be the improved diffusion of the silica layer, facilitated by sodium, leading to better bonding between SiC particles. However, the observed dimensional stability at higher temperatures suggests a minimal role of particle fusion in the strengthening mechanism.

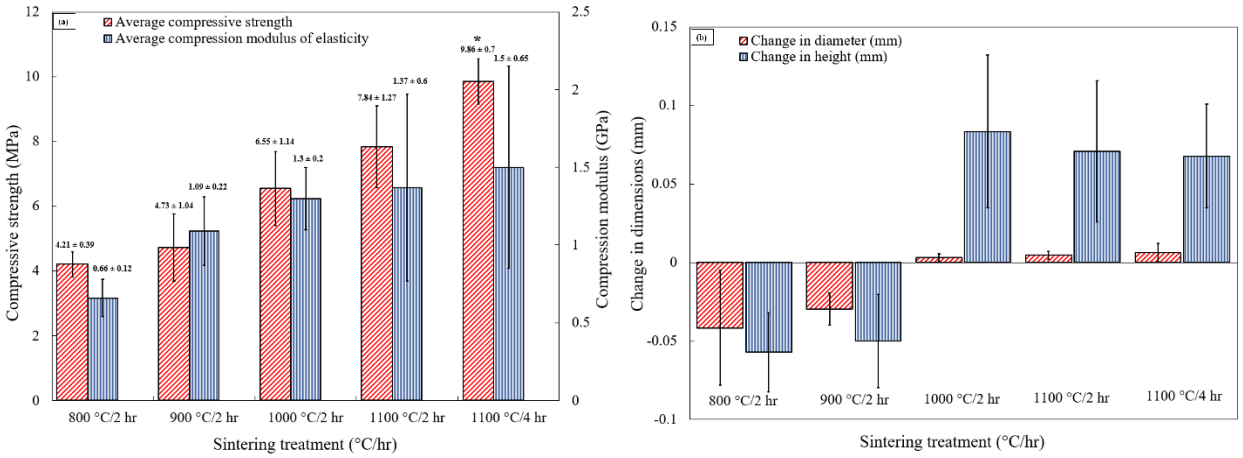

Figure 17: Comparison of (a) average compressive strength and (b) dimensional stability of 3D printed SiC discs impregnated in 10% NaOH concentration for 15 mins and subjected to heat treatment at nucleation temperature 550 °C/6 hr and various sintering temperature and time, 800 °C/ 2 hr, 900 °C/2 hr, 1000 °C/2 hr, 1100 °C/2 hr, and 1100 °C/4 hr in air environment at a heating rate of 1 °C/min. (* sign indicates $p<0.05$.)

2.2.10 Density and porosity (%) measurements

Figure 18 depicts the comparison of apparent density and apparent open porosity % of 3D printed SiC discs impregnated in 10% NaOH concentration for 15 mins and subjected to heat treatment at nucleation temperature 550 °C/6 hr and various sintering temperatures, 800 °C/ 2 hr, 900 °C/2 hr, 1000 °C/2 hr, 1100 °C/2 hr, and 1100 °C/4 hr in air environment at a heating rate of 1 °C/min. The apparent density calculations revealed that as the sintering temperature increased from 800 °C to 1100 °C, apparent density decreased gradually. The samples impregnated in 10% NaOH heat treated at 550°C/6 h and 800 °C/ 2 hr showed the highest densities of all the samples, with density value of 2.52 gcm^{-3}. As the sintering temperature increased to 900 °C, apparent density decreased to 2.49 gcm^{-3} and both 1000 °C and 1100 °C for 2 hr heat treatment showed a comparable density value of 2.31 gcm^{-3}. The samples heat treated at 1100 °C/4 hr showed a significantly smaller density of 2.27 gcm^{-3} compared to all other samples due to increased amount of cristobalite phase formation. The apparent open porosity calculations showed a similar trend as the density. The strength of the 3D printed samples increased as the porosity of the sample decreased. The samples impregnated in 10% NaOH heat treated at 550°C/6 h and 800

°C/2 hr showed the highest apparent porosity of 49.37% whereas samples treated at 1100 °C/4 hr showed significantly low apparent open porosity of 38.32%.

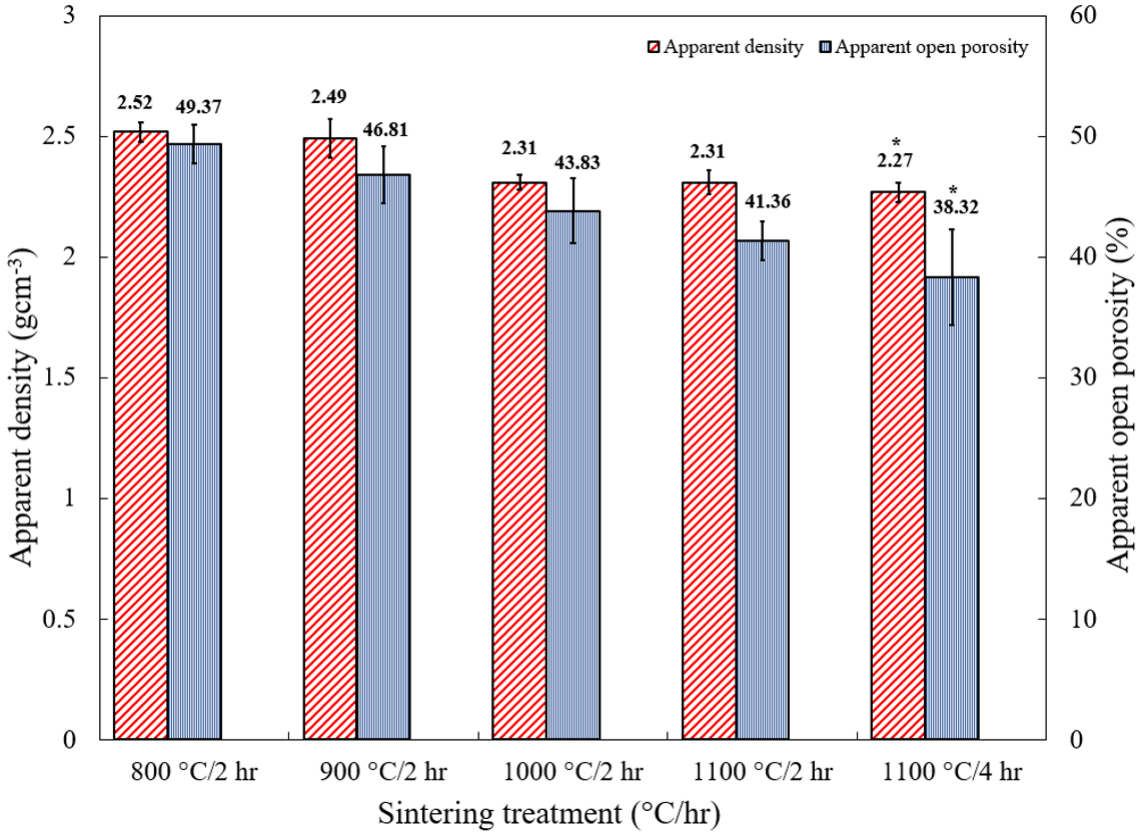

Figure 18: Comparison of apparent density and apparent porosity % of 3D printed SiC discs impregnated in 10% NaOH concentration for 15 mins and subjected to heat treatment at nucleation temperature 550 °C/6 hr and various sintering temperature 800 °C/ 2 hr, 900 °C/2 hr, 1000 °C/2 hr, 1100 °C/2 hr, and 1100 °C/4 hr in air environment at a heating rate of 1 °C/min. (* sign indicates $p<0.05$.)

CHAPTER 3: SILICA NANOWIRE GROWTH MECHANISM AND GROWTH MODEL

3.1 Silica Nanowire Growth Mechanism

Figure 19 shows the SEM analysis showing the growth of silica nanowires inside the pores of SiC discs (5 mm diameter ×4 mm length) pretreated with 20 % NaOH and thermally treated at (a) 525 °C/15 mins, (b) 800 °C/15 mins, and (c) 1100 °C/30 mins respectively. At 525 °C EDX analysis showed that the silica droplets formed from the silica gel layer are oxygen deficient as shown in Figure 20. At the early stage of droplet formation, the silica structure is amorphous and becomes rich in hydroxyl (OH^-) ions. At 800 °C the droplets grow into nanowires as seen in Figure 19b. As the heat treatment temperature is raised to 1100 °C the length of the nanowires increases (Figure 19c).

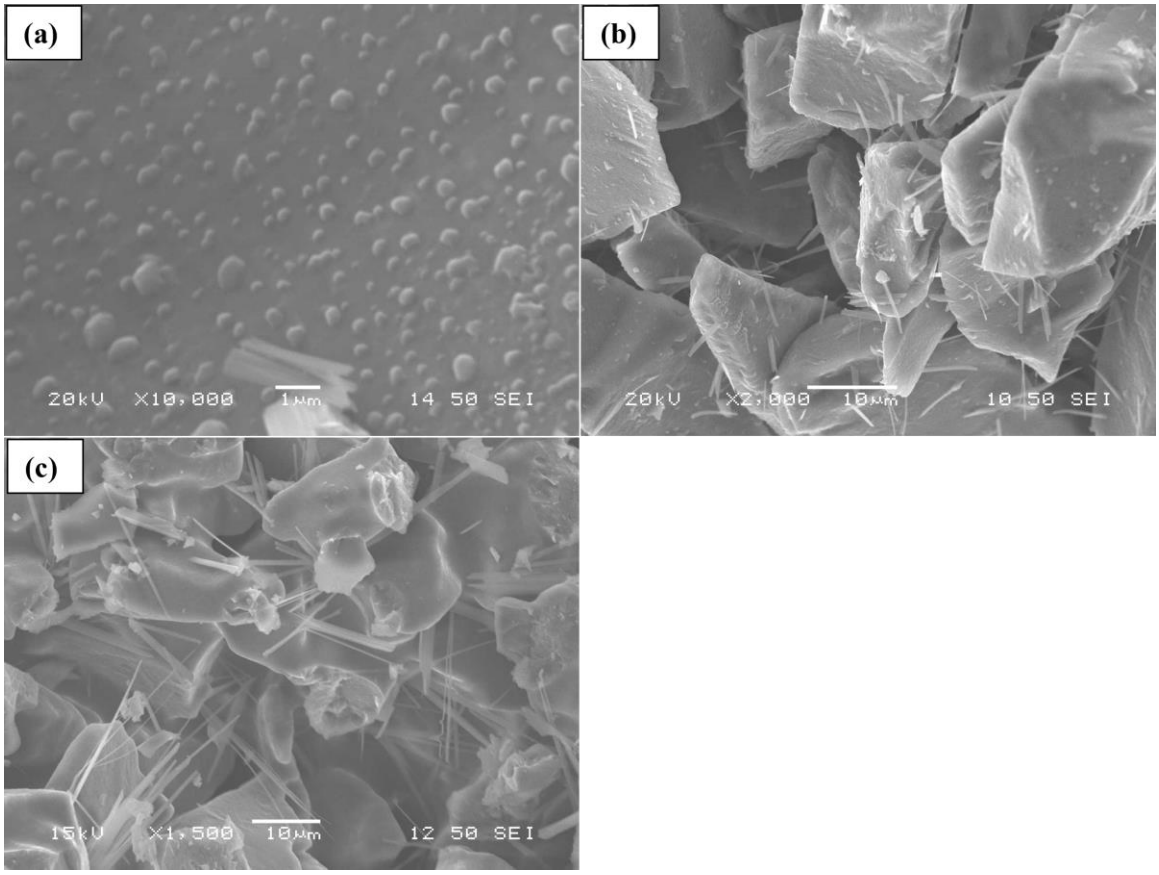

Figure 19: SEM images of the fracture surface of 3D SiC porous discs pretreated with 20% NaOH showing the formation of (a) silica droplets (nuclei) on the surface of SiC particles formed at 525 °C/15 mins, (b) small silica nanowires formation after treatment at 800 °C/15 mins, (c) long nanowires growth after treatment at 1100 °C/30 mins.

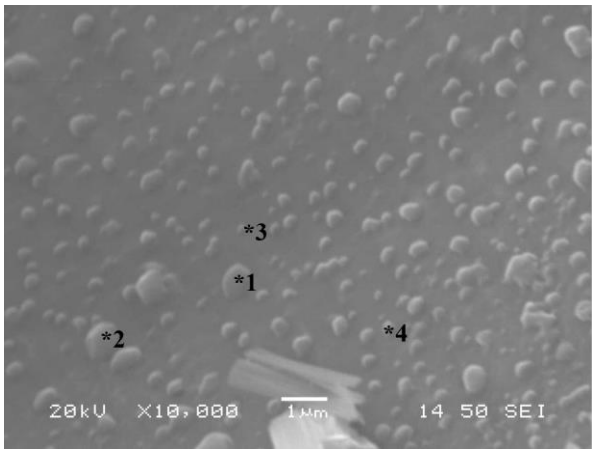

Spot	C atomic %	Si atomic %	Na atomic %	O Atomic %
1	35.43	52.47	1.34	10.77
2	21.75	66.78	0.72	10.75
3	32.18	58.36	0.61	8.85
4	34.30	57.14	0.71	7.84

Figure 20: SEM fracture surface analysis of the 3D SiC discs pretreated with 20% NaOH and heat treated at 525 °C/15 mins showing the EDX elemental composition of silica droplets (spots 1, 2, 3, and 4) formed on the SiC particle surface.

Figure 21 shows SEM images at higher magnifications of fractured surface of 3D printed SiC discs that were impregnated in 10% NaOH/15 min and heat treated at (a) 800 °C/15 min and

(b) 1100 °C/30 min. More silica crystals and droplets appeared on the surface of the pores with the presence of few nanowires at the grain boundaries as seen in Figure 21a. This implies that in the initial stage of nanowire formation, the presence of defects on the SiC surface makes a preferential high energy active site for nanowires formation. At 1100 °C longer nanowires were observed (Figure 21b). It was difficult to identify the grain boundaries at high temperature due to the increase of thickness of the oxide layer.

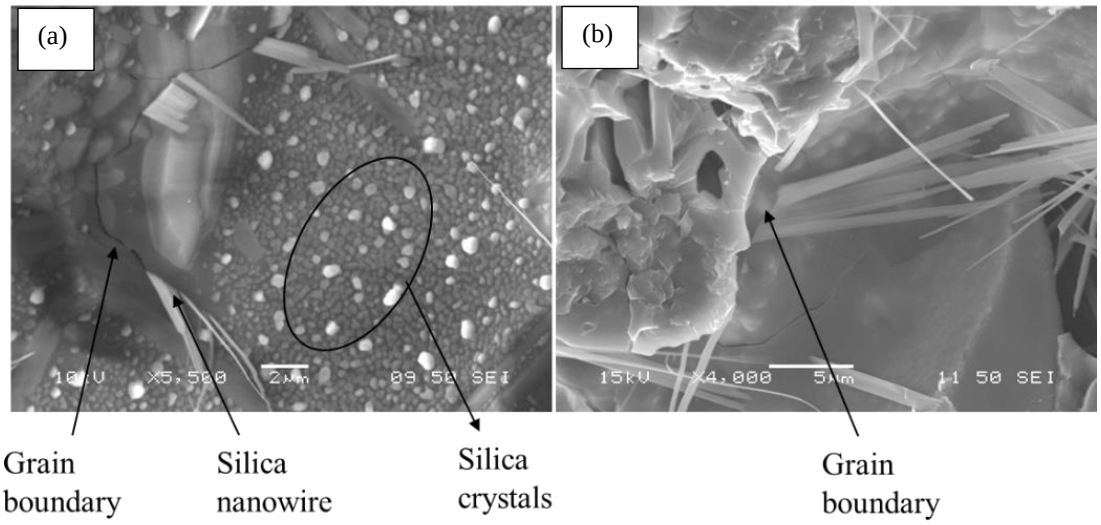

Figure 21: SEM images of the fracture surface of 3D printed SiC porous discs. (a) Presence of silica crystals in the absence of surface defects (black circle) and (b) silica nanowire formation along the grain boundaries (black arrows).

Data in the literature indicated that nanowires could grow by vapor-liquid-solid (VLS) [110-116] growth mechanism which make use of a molten catalyst droplet for axial growth or vapor-solid (VS) growth mechanism [117-123] which is a non-catalyst growth. The vapor-liquid-solid (VLS) method, introduced by Wagner [110] in the mid-1960s for producing Si microwires, has become a highly utilized and effective approach for growing high-quality 1D semiconductor structures. This technique employs catalytic metal nanoparticles, commonly gold Au [110, 124], but also other metals such as Ti [112], Fe [125], Ag [126], Cu [127], Co [128], Ni [129], Ga [130, 131], Al [131], etc., act as catalysts by absorbing and dissolving the semiconductor vapor

to form a liquid alloy to accommodate vapor precursors, form seeds, and guide growth, allowing for selective control over the site, orientation, dimension, and morphology of the nanowires. In the VS mechanism, semiconductor material vapor reacts directly with a solid substrate, usually a crystalline seed particle or substrate, to form nanowires or nanostructures [120-123]. Unlike the VLS mechanism, there is no liquid phase or foreign catalyst involved in the growth process. The semiconductor vapor condenses directly onto the solid substrate, leading to the nucleation and growth of one-dimensional nanostructures. The resulting nanostructures exhibit characteristics determined by the substrate and growth conditions.

In the present study, an oxidation step at room temperature is initiated by mixing SiC particles with NaOH solution. The NaOH treatment breaks the Si–C bond, releasing the free silanol groups ($Si(OH)_n$, n = 1–4) that subsequently form a silica gel layer on the material surface. The generation of silanol groups is facilitated by the low electronegativity of Si, promoting bonding with hydroxyl ions (OH) and resulting in the formation of silanol groups ($Si(OH)_4$) along with the release of free carbon, as indicated by the eq (3).

$$SiC + 4OH^- \rightarrow Si(OH)_4 + C^- \quad (3)$$

Heating the 3D printed SiC discs at 525 °C results in the formation of silica droplets on the inner walls of the SiC pores (Figure 19). These droplets serve as nucleation sites for silica nanowire growth. As the heat treatment continues, up to 700 °C he silanol groups undergoes condensation of the hydroxyl groups that leads to elimination of water (H_2O) molecules and formation of Si-O-Si siloxane bridges to form silica layer (SiO_2) according to the eq (4),

$$Si(OH)_4(s) + Si(OH)_4(s) \rightarrow 2SiO_2(s) + 4H_2O(g) \quad (4)$$

EDX analysis (Figure 20) revealed that the silica droplets exhibit oxygen deficiency. The oxygen deficiency of the silica droplets renders them a high energy sites for further reaction. Previous work from our lab [62, 63] demonstrated the release of SiO and $Si(OH)_4$ vapor upon heating porous 3D SiC discs, pretreated with 20 % NaOH, at 500 °C/25 min. SiO vapor was generated alongside CO, as carbon atoms compete with the Si atoms for oxygen, inducing a redox reaction that resulted in the partial reduction of the silica layer (SiO_2) through the involvement of incoming carbon, as described by the eq (5),

$$SiO_2(s) + C^- \rightarrow SiO(g) + CO(g) \tag{5}$$

Motivated by the oxygen concentration gradient the silica nanowires grow upward towards the open space inside the pore. It is worth mentioning that the outer tip of the growing nanowires does not show the initial round droplet that formed at 525 °C suggesting direct condensation of various evaporated molecules on the active surface of the droplet. As the heat treatment continued from 700 °C to 1100 °C, SiO_2 molecules formed simultaneously due to reaction between SiO vapor and oxygen molecules from air according to eq (6) and reaction between two $Si(OH)_4$ vapor and released water vapor according to eq (7),

$$2SiO\ (g) + O_2(g) \rightarrow 2SiO_2(s) \tag{6}$$

$$Si(OH)_4(g) + Si(OH)_4(g) \rightarrow 2SiO_2(s) + 4H_2O(g) \tag{7}$$

Figure 22 shows the schematic growth of the nanowire nucleation and growth of silica (SiO_2) nanowire by following the VS mechanism inside the pore of 3D printed SiC disc, (a) Droplet formation, (b) Deposition of SiO_2 molecules and growth of nanowire, and (c) consumptions of the reactants due to the growth of the nanowire.

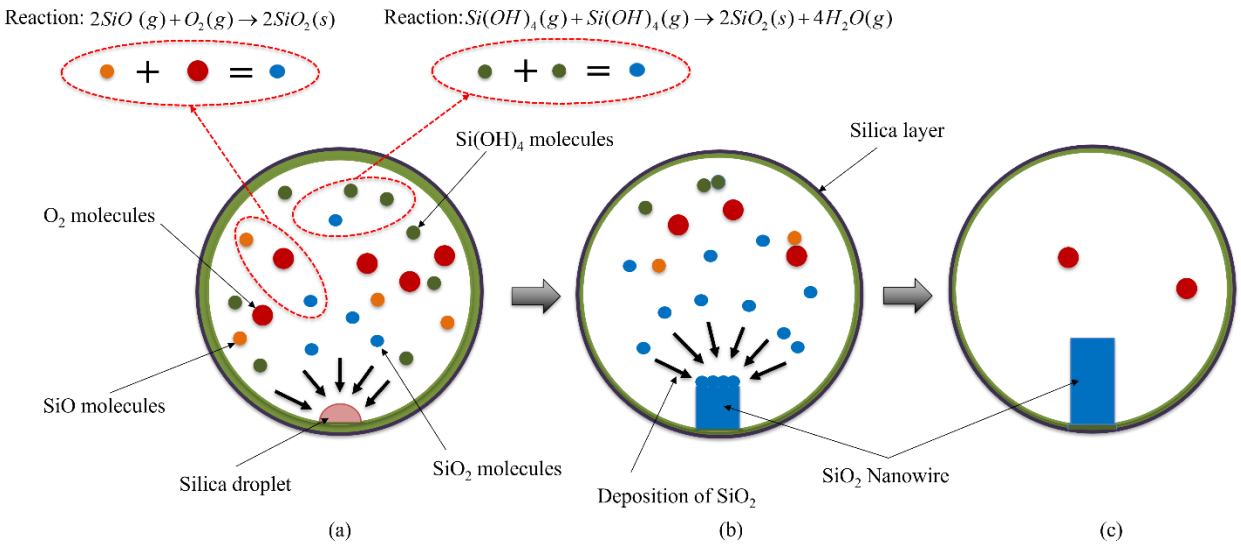

Figure 22: Scheme of nucleation and growth of silica (SiO_2) nanowire by VS mechanism inside the pore of 3D printed SiC disc. (a) Droplet formation, (b) Deposition of SiO_2 molecules and growth of nanowire, and (c) consumptions of the reactants due to the growth of the nanowire.

The above nanowire growth mechanism inside SiC pores is supported by several studies which indicated that that highlight the reactivity of SiO gas molecules, along with $(SiO)_2$ and $(SiO)_3$ oligomers, with oxygen molecules. This reactivity leads to the formation of a linear $(SiO_2)_n$ structure [132-134]. SEM analysis of nanowires after thermal treatment showed a continuous increase in the length of the nanowires without noticeable change in the width. This is attributed to the high energy of the tip of the nanowires due to lack of bonding of the tip atoms with the maximum nearest neighbors. The side Si-O-Si moiety in the cyclic structure of the nanowire are already bonded with maximum nearest neighbor (Figure 23), so they have less motivation to react with vapor molecules inside the pore. It was found that the nanowire width was similar to that of the droplet size.

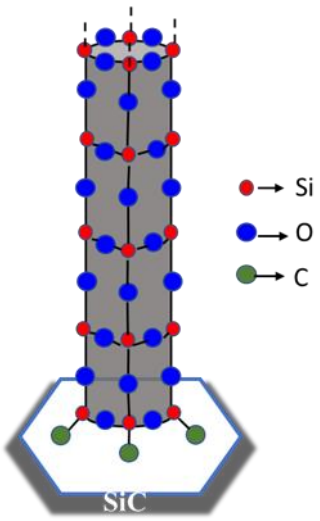

Figure 23: Schematic of a growing silica (SiO_2) nanowire on the SiC particle surface showing the bonded side surface of the nanowire and open bonds on the top surface as an active surface for nanowire growth.

Therefore, the modeling efforts will focus on the growth of silica nanowire length via chemical reactions involved in the formation of silica molecules and deposition of these molecules. The primary purpose of the models is to study the effect that the post processing parameters have on the growth of silica nanowire which fills the pore of 3D printed SiC disc and, therefore, provides strength for the additively manufactured parts. The process parameters of primary importance are the NaOH concentration, and the sintering time-temperature profile. We focus our attention on the chemical reactions happening inside the pore of the SiC disc as described in the above chemical reactions for silica nanowire growth. In this model, it was assumed that 50% of silanol groups reacted to form silica layer according to above eq (2) and 50% released inside the pore of the 3D SiC disc as $Si(OH)_4$ vapor and contributes into nanowire growth which be discussed later.

3.2 Reaction kinetics

In the context of chemical reactions, the law of mass action for elementary reactions establishes that the rate of a reaction is directly proportional to the powers of the concentrations of the reacting species [135]. However, when dealing with more complex reactions, researchers

often resort to simplified kinetic models. In such models, the powers may not precisely match the stoichiometric coefficients of the reacting species and are frequently determined through experimental investigation [136, 137]. In our case, we adopt a simplification by considering each chemical reaction as a one-step, irreversible process, represented by eq (1-5). This simplification involves treating each reaction as first order in both reactants. [102, 135, 138]. The reaction rates (K_i) exhibit a strong dependence on temperature, a relationship that can be elucidated through the inclusion of an Arrhenius term in the model. This Arrhenius term captures the exponential dependence of reaction rates on temperature and is formulated in a manner that involves the activation energy of the reaction. The Arrhenius equation is commonly employed in chemical kinetics to describe how the rate of a reaction changes with temperature. It is expressed as:

$$K_i(T) = A_i \exp\left(-\frac{E_{a_i}}{RT}\right), \tag{8}$$

where A_i is a pre-exponential constant, E_{a_i} is the activation energy of the reaction, T is the sintering temperature, R = 8.314 J.mol^{-1}K^{-1} is the universal gas constant, and i is the reaction number varying as $i = 1, 2, 3, 4, 5$.

System of ordinary differential equations (ODEs) for reaction given by equation 3 can be represented as,

$$\frac{dC_{SiC}}{dt} = -K_1 C_{SiC} C_{OH^-} \tag{9a}$$

$$\frac{1}{4}\frac{dC_{OH^-}}{dt} = -K_1 C_{SiC} C_{OH^-} \tag{9b}$$

$$\frac{dC_{Si(OH)_4}}{dt} = K_1 C_{SiC} C_{OH^-} \tag{9c}$$

$$\frac{dC_{C^-}}{dt} = K_1 C_{SiC} C_{OH^-} \tag{9d}$$

where $\frac{d}{dt}$ represents the change of concentration with respect to time for the reactants i.e., C_{SiC} and C_{OH^-} and products $C_{Si(OH)_4}$ and C_{C^-}.

Similarly for system of ordinary differential equations for the remaining chemical reactions shown in equations (4-7) can be given as:

For equation 4:

$$\frac{1}{2}\frac{dC_{Si(OH)_4}}{dt} = -K_2 C_{Si(OH)_4} C_{Si(OH)_4} \tag{10a}$$

$$\frac{1}{2}\frac{dC_{SiO_2}}{dt} = K_2 C_{Si(OH)_4} C_{Si(OH)_4} \tag{10b}$$

$$\frac{1}{4}\frac{dC_{H_2O}}{dt} = K_2 C_{Si(OH)_4} C_{Si(OH)_4} \tag{10c}$$

For equation 5:

$$\frac{dC_{SiO_2}}{dt} = -K_3 C_{SiO_2} C_{C^-} \tag{11a}$$

$$\frac{dC_{C^-}}{dt} = -K_3 C_{SiO_2} C_{C^-} \tag{11b}$$

$$\frac{dC_{SiO}}{dt} = K_3 C_{SiO_2} C_{C^-} \tag{11c}$$

$$\frac{dC_{CO}}{dt} = K_3 C_{SiO_2} C_{C^-} \tag{11d}$$

For equation 6:

$$\frac{1}{2}\frac{dC_{SiO}}{dt} = -K_4 C_{SiO} C_{O_2} \tag{12a}$$

$$\frac{dC_{O_2}}{dt} = -K_4 C_{SiO} C_{O_2} \tag{12b}$$

$$\frac{1}{2}\frac{dC_{SiO_2}}{dt} = K_4 C_{SiO} C_{O_2} \tag{12c}$$

For equation 7:

$$\frac{1}{2}\frac{dC_{Si(OH)_4}}{dt} = -K_5 C_{Si(OH)_4} C_{Si(OH)_4} \tag{13a}$$

$$\frac{1}{2}\frac{dC_{SiO_2}}{dt} = K_5 C_{Si(OH)_4} C_{Si(OH)_4} \tag{13b}$$

$$\frac{1}{4}\frac{dC_{H_2O}}{dt} = K_5 C_{Si(OH)_4} C_{Si(OH)_4} \tag{13c}$$

3.3 Deposition of SiO_2 Molecules:

The deposition rate of the SiO_2 molecules depends on the concentration of SiO_2 molecules and temperature according to Hertz-Knudsen equation [91, 97, 139, 140],

$$Z = C_{SiO_2}\sqrt{\frac{k_b T}{2\pi m}}, \tag{14}$$

where Z is the deposition rate of the SiO_2 molecules, C_{SiO_2} is the SiO_2 molecules concentration obtained by solving the ODEs given by equations (9-13), k_b is the Boltzmann constant, and m is the molecular weight of SiO_2 molecule.

Silica nanowire vertical growth rate can be measured as changing its volume during the introduction of the SiO_2 molecules on the top surface of the nanowire.

$$\frac{dL}{dt} = Z\Omega \tag{15}$$

where L is the length of nanowire and Ω is the volume of single SiO_2 molecule.

3.4 Numerical Approach

In this work the forward Euler method was used for solving the system of ODEs given by equations (9-13). The Forward Euler method is a numerical technique used for approximating the ODEs. This method is based on the idea of discretizing the time domain and approximating the derivative of a function using a finite difference.

For a first-order ODE of the form

$$\frac{dy}{dt} = f(t, y), \tag{16}$$

Where, y is the dependent variable, t is the independent variable (time), and f is a given function, the Forward Euler method updates the solution at each time step using the following formula:

$$y_{n+1} = y_n + dt \cdot f(y_n, t_n), \tag{17}$$

where, y_{n+1} is the updated approximation of the solution at the next time step, y_n is the approximation of the solution at the current time step, dt is the step size, representing the size of the time intervals, and t_n is the current time.

The method starts with an initial value y_0 and iteratively computes the solution at subsequent time steps using equation (17). Using equation (17) of Forward Euler method, equation (9a) can be given as

$$\left(C_{SiC}\right)_{n+1} = \left(C_{SiC}\right)_n + dt \cdot f\left(\left(C_{SiC}\right)_n, t_n\right). \tag{18}$$

where $\left(C_{SiC}\right)_{n+1}$ is the SiC concentration at the next time step t_{n+1}, $\left(C_{SiC}\right)_n$ is the SiC concentration at the current time step t_n, and t_n is the current time. Here the value of $f(C_{SiC}(t_n), t_n)$ can be obtained using equation (9a) as,

$$f\left(\left(C_{SiC}\right)_n, t_n\right) = -K_1\left(C_{SiC}\right)_n\left(C_{OH^-}\right)_n. \tag{19}$$

Hence, the complete set of discretized ODEs representing equation (9) can be given as,

$$\left(C_{SiC}\right)_{n+1} = \left(C_{SiC}\right)_n - dt \cdot K_1\left(C_{SiC}\right)_n\left(C_{OH^-}\right)_n \tag{20a}$$

$$\left(C_{OH^-}\right)_{n+1} = \left(C_{OH^-}\right)_n - 4 \cdot dt \cdot K_1\left(C_{SiC}\right)_n\left(C_{OH^-}\right)_n \tag{20b}$$

$$\left(C_{Si(OH)_4}\right)_{n+1} = \left(C_{Si(OH)_4}\right)_n + dt \cdot K_1\left(C_{SiC}\right)_n\left(C_{OH^-}\right)_n \tag{20c}$$

$$\left(C_{C^-}\right)_{n+1} = \left(C_{C^-}\right)_n + dt \cdot K_1\left(C_{SiC}\right)_n\left(C_{OH^-}\right)_n \tag{20d}$$

Similarly, discretized version of ODEs given in equations (10-13) can be obtained and are given in Appendix A.

3.5 Results and discussions of modeling work

This section discusses the results of the model presented in section 3.4. Equations 9 to 13 were solved simultaneously using Forward Euler method by writing a script in MATLAB. The initial concentrations used for SiC, hydroxyl (OH^-) ions, and oxygen are given in Table 1. All the chemical parameters used in the model are given in Table 2.

Figure 24 shows plots of concentrations of reactants and products presented in equation (3) with respect to time. The value of 'dt' was 0.005 seconds. The concentration of $Si(OH)_4$ groups and free carbon formation increased as the hydroxyl (OH^-) groups from NaOH were

chemically attacking the SiC particles surface. Furthermore, as the NaOH concentration increased from 5% to 20 %, the amount of silanol groups formation also increased. The hydroxyl group and SiC concentration decreased with respect to time and eventually reached zero resulting in a steady state. Increase in the NaOH concentration also led to the delay in achieving the steady state.

Table 1: Initial concentrations used in the model.

Initial concentration	Value	Units
$C_{SiC,0}$	0.00074793	No of moles
For 5% NaOH, $C_{OH,0}$	0.00000214	No of moles
For 10% NaOH, $C_{OH,0}$	0.00000428	
For 20% NaOH, $C_{OH,0}$	0.00000857	
$C_{O_2,0}$	2 [135]	No of moles

Table 2: Typical values of parameters used in the model described in chapter 4.

Parameter	Value	Units
A_1	1.0×10^3	$m^2/(mol^2 \cdot s)$
A_2	1.0×10^7 [102]	$m^2/(mol^2 \cdot s)$
A_3	1.0×10^4 [138]	$m^2/(mol^2 \cdot s)$
A_4	1.0×10^7 [135]	$m^2/(mol^2 \cdot s)$
A_5	1.0×10^7 [102]	$m^2/(mol^2 \cdot s)$
E_{a1}	27196	J/mol
E_{a2}	94900 [102]	J/mol
E_{a3}	120000 [138]	J/mol
E_{a4}	27196 [135]	J/mol
E_{a5}	94900 [102]	J/mol
R	8.314	$J/(mol \cdot K)$
k_B	1.3806×10^{-23}	J/K
m	9.96×10^{-26} [135]	Kg
Ω	4.536×10^{-29} [135]	m^3

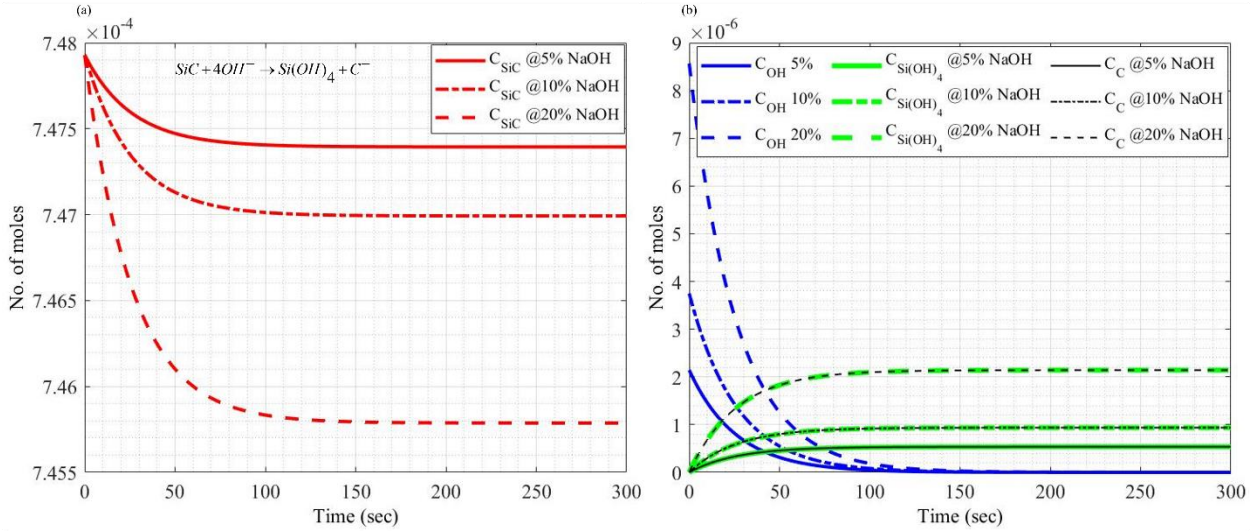

Figure 24: Plots of concentrations of reactant (a) SiC (red lines), and (b) OH (blue lines) and products $Si(OH)_4$ (green lines) and C (black lines) of equation (3) with respect to time obtained by solving equation (20).

Figure 25 shows plots of concentrations of reactants and products presented in equation (4) with respect to time. The silanol groups formed after the first reaction react with each other and goes through dehydroxylation reaction according to equation (4). It forms silica (SiO_2) layer on the SiC particles while releasing water vapor. The SiO_2 concentration (Figure 25) initially increases at a fast rate and eventually reaches a steady state value as the $Si(OH)_4$ concentration goes to zero. The SiO_2 concentration during this reaction increases as NaOH concentration increases.

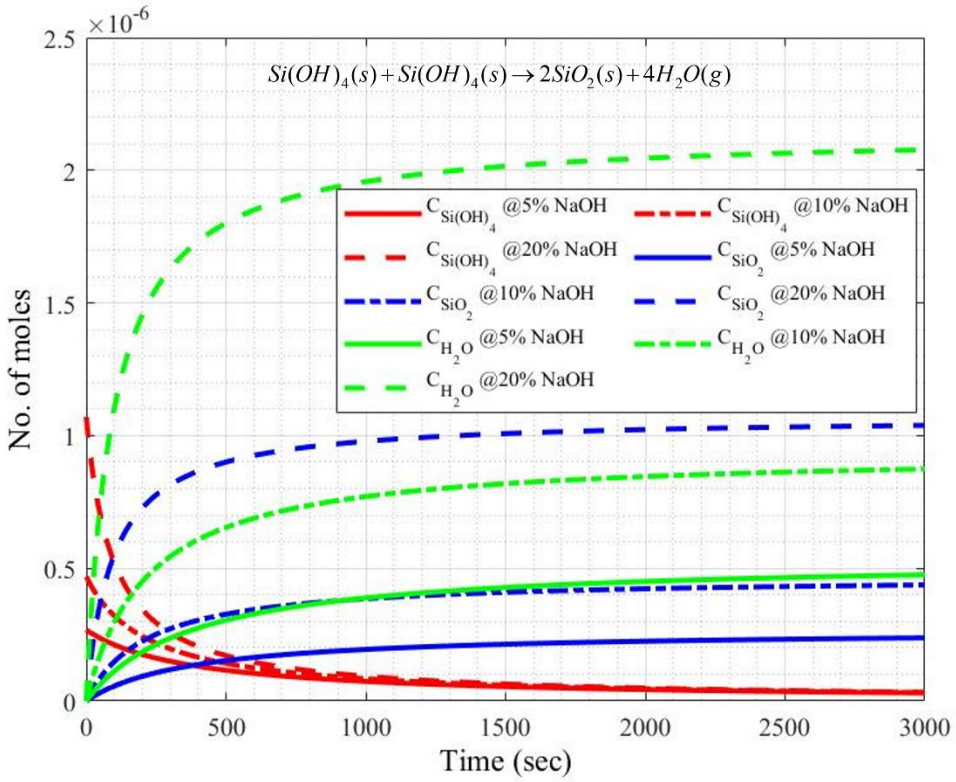

Figure 25: Plots of concentrations of reactants $Si(OH)_4$ (red lines) and products SiO_2 (blue lines) and H_2O (green lines) of equation (4) with respect to time obtained by solving equation (21) given in appendix.

Figure 26 shows plots of concentrations of reactants and products presented in equation (5) with respect to time. SiO vapor concentration increases as the free carbon generated from equation (3) reacts with the SiO_2 layer. In this reaction, the amount of SiO concentration formed is same as the CO concentration. The steady state is achieved due to the consumption of SiO_2 layer. The SiO concentration value is directly proportional to the initial concentration of NaOH.

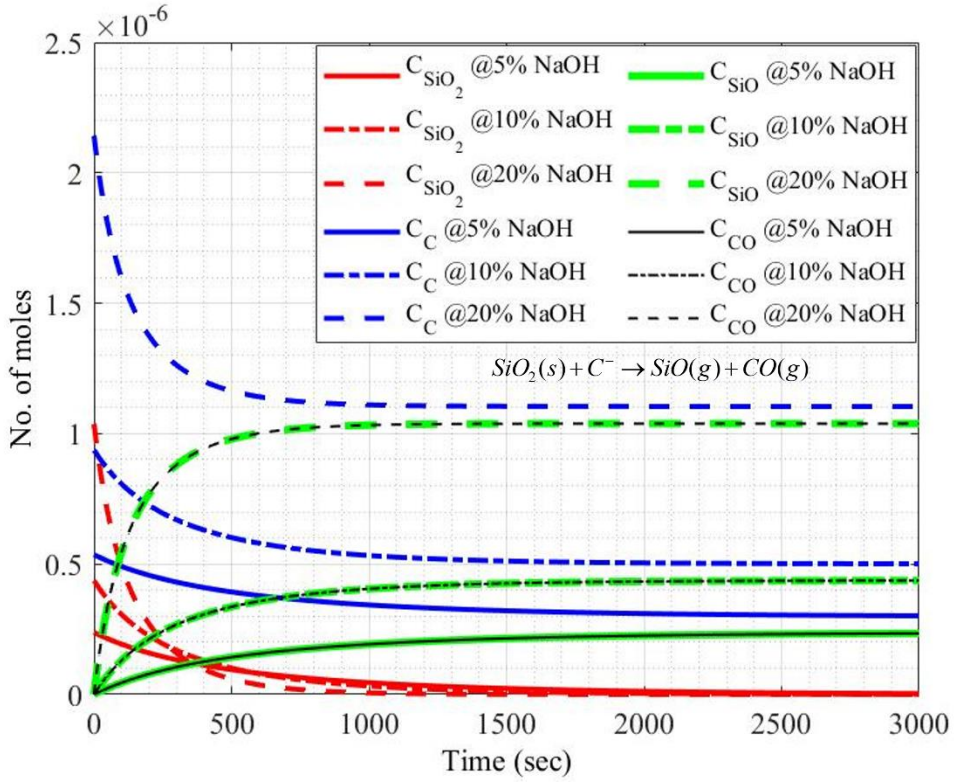

Figure 26: Plots of concentrations of reactants SiO_2 (red lines) and C (blue lines) and products SiO (green lines) and CO (black lines) of equation (5) with respect to time obtained by solving equation (22) given in appendix.

Figure 27-29) show plots of concentrations of reactants and products presented in equation (6) with respect to time for sintering temperatures varying from 800 °C to 1100 °C. The SiO vapor produced from equation (5) reacts with oxygen molecules from air inside the pore of 3D SiC disc and forms the SiO_2 molecules according to the equation (6). The SiO concentrations decreases with respect to time and eventually reachs zero resulting in a steady state. Increase in the NaOH concentration leads to the delay in achieving the steady state. Furthermore, Figure 27 and 28 show that as temperature increases, SiO and O_2 concentration reaches the steady state faster as according to Arrhenius equation reaction rate increases with increasing temperature. The SiO_2 concentration reaches a maximum value initially while the reaction occurs (Figure 29), and it later decreases as SiO_2 is consumed due to silica nanowire growth.

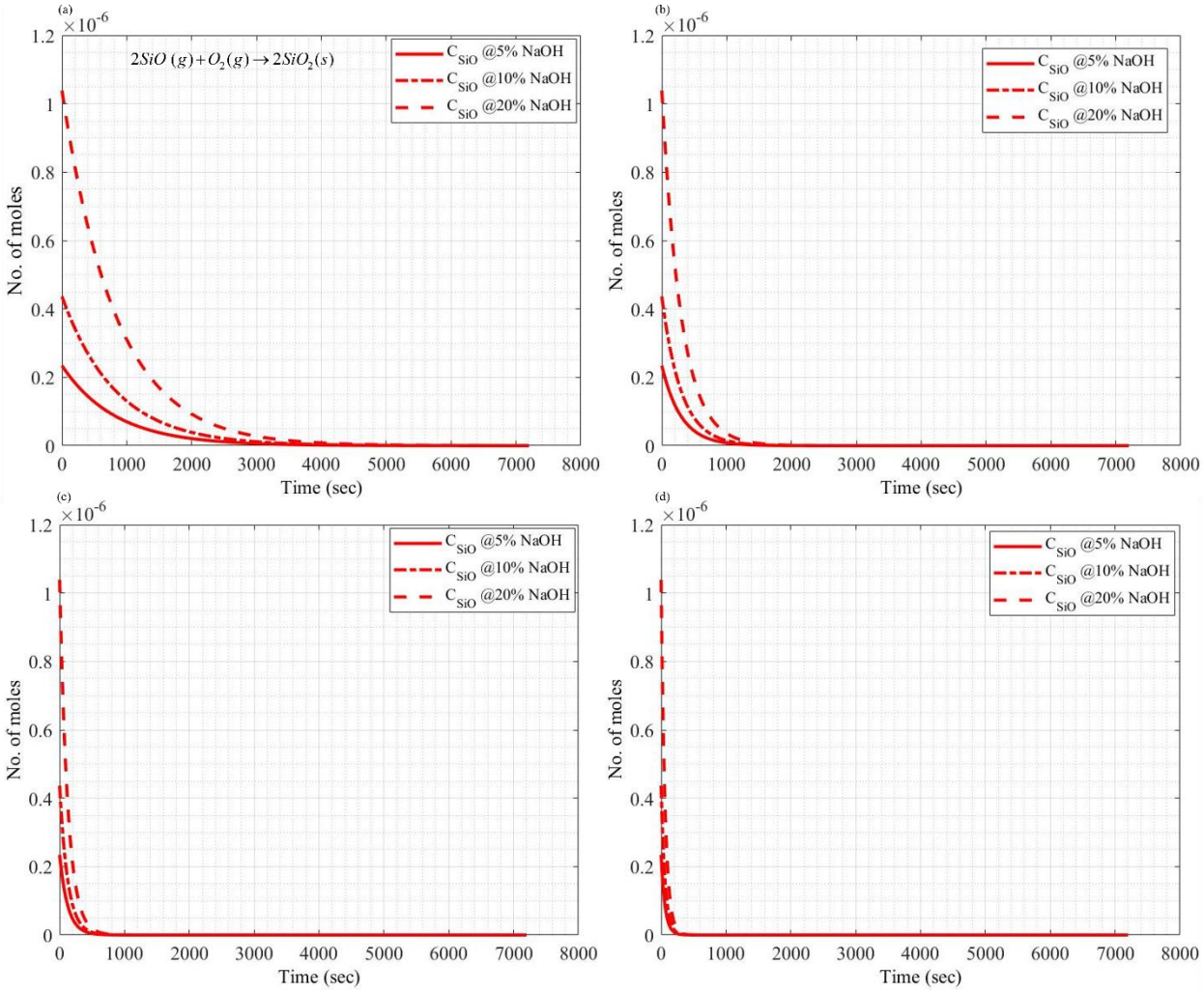

Figure 27: Plots of the SiO concentrations from equation (6) with respect to time over the sintering temperatures for (a) 800 °C, (b) 900 °C, (c) 1000 °C and (d) 1100 °C obtained by solving equation (23) given in appendix.

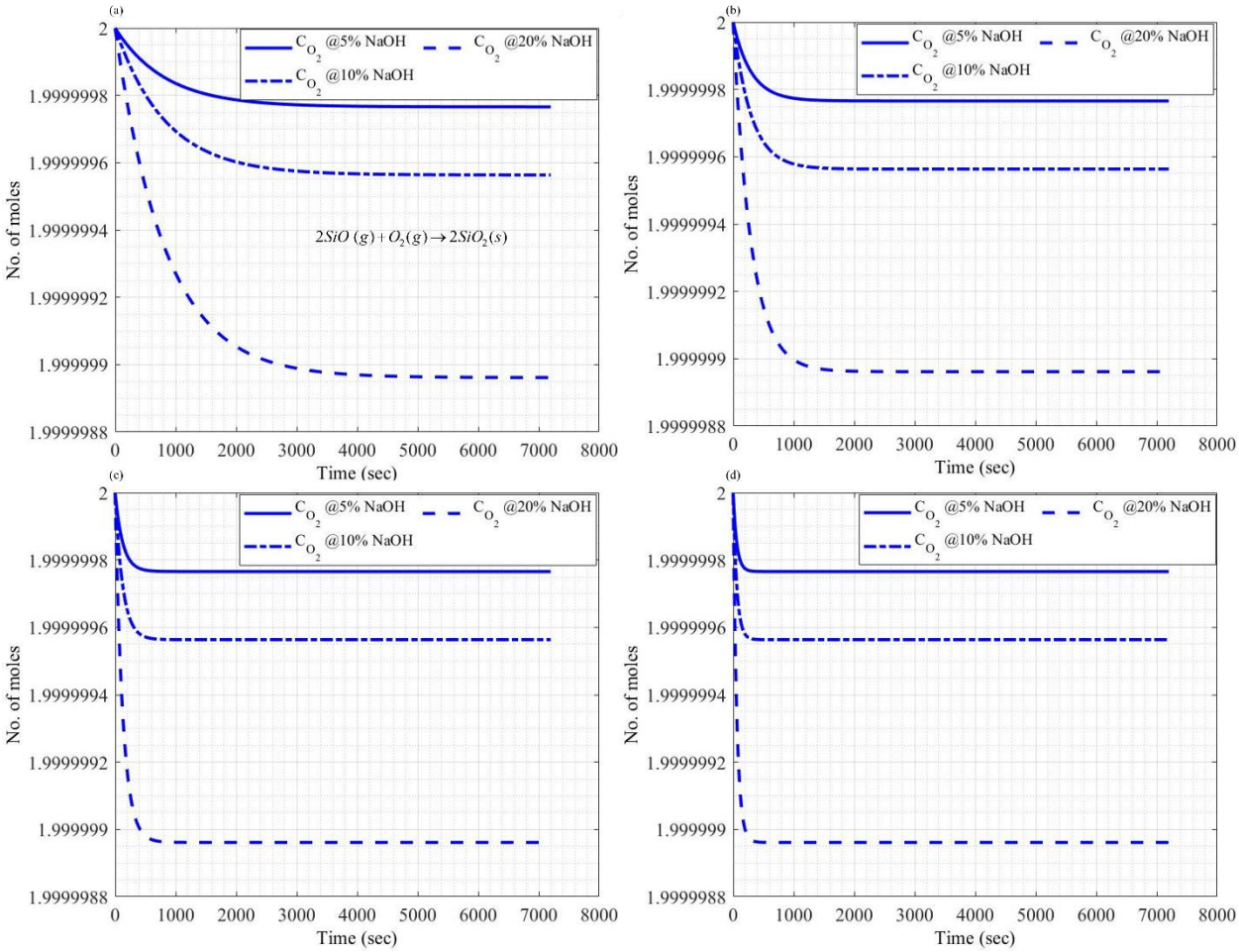

Figure 28: Plots of the O_2 concentrations from equation (6) with respect to time over the sintering temperatures for (a) 800 °C, (b) 900 °C, (c) 1000 °C and (d) 1100 °C obtained by solving equation (23) given in appendix.

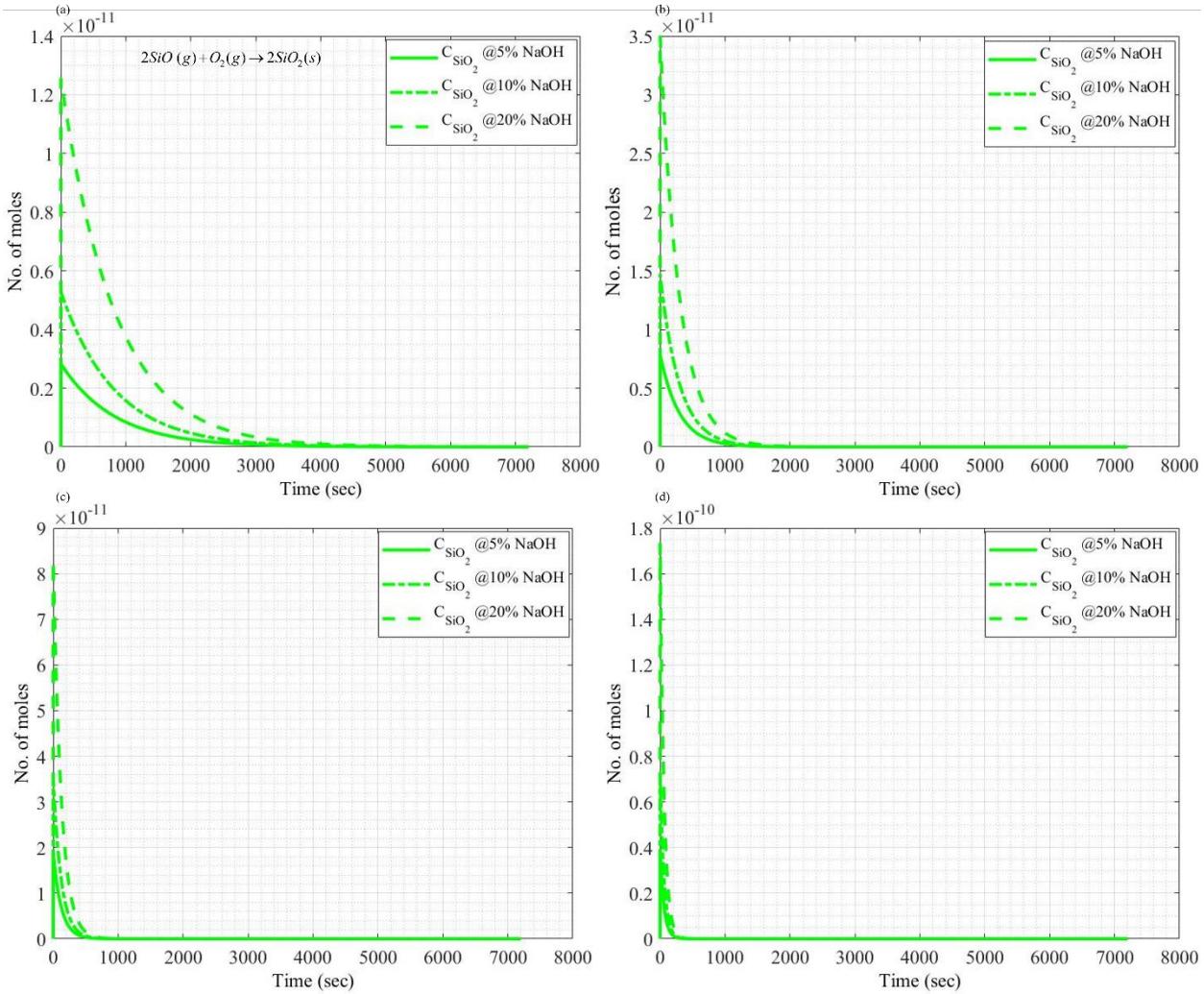

Figure 29: Plots of SiO_2 concentrations from equation (6) with respect to time over the sintering temperatures for (a) 800 °C, (b) 900 °C, (c) 1000 °C and (d) 1100 °C obtained by solving equation (23) given in appendix.

Figure 30 and 31 show plots of concentrations of reactants and products presented in equation (7) with respect to time for sintering temperature varying from 800 °C to 1100 °C. SiO_2 concentration reaches a maximum initially while the $Si(OH)_4$ vapor reaction occurs according to equation (7), and it later decreases as SiO_2 molecules get deposited for silica nanowire growth. As the sintering temperature increases, the $Si(OH)_4$ consumes faster and eventually reaches zero resulting in a steady state, and as the increase in NaOH concentration delays in obtaining steady state resulting in more SiO_2 molecules in the sample.

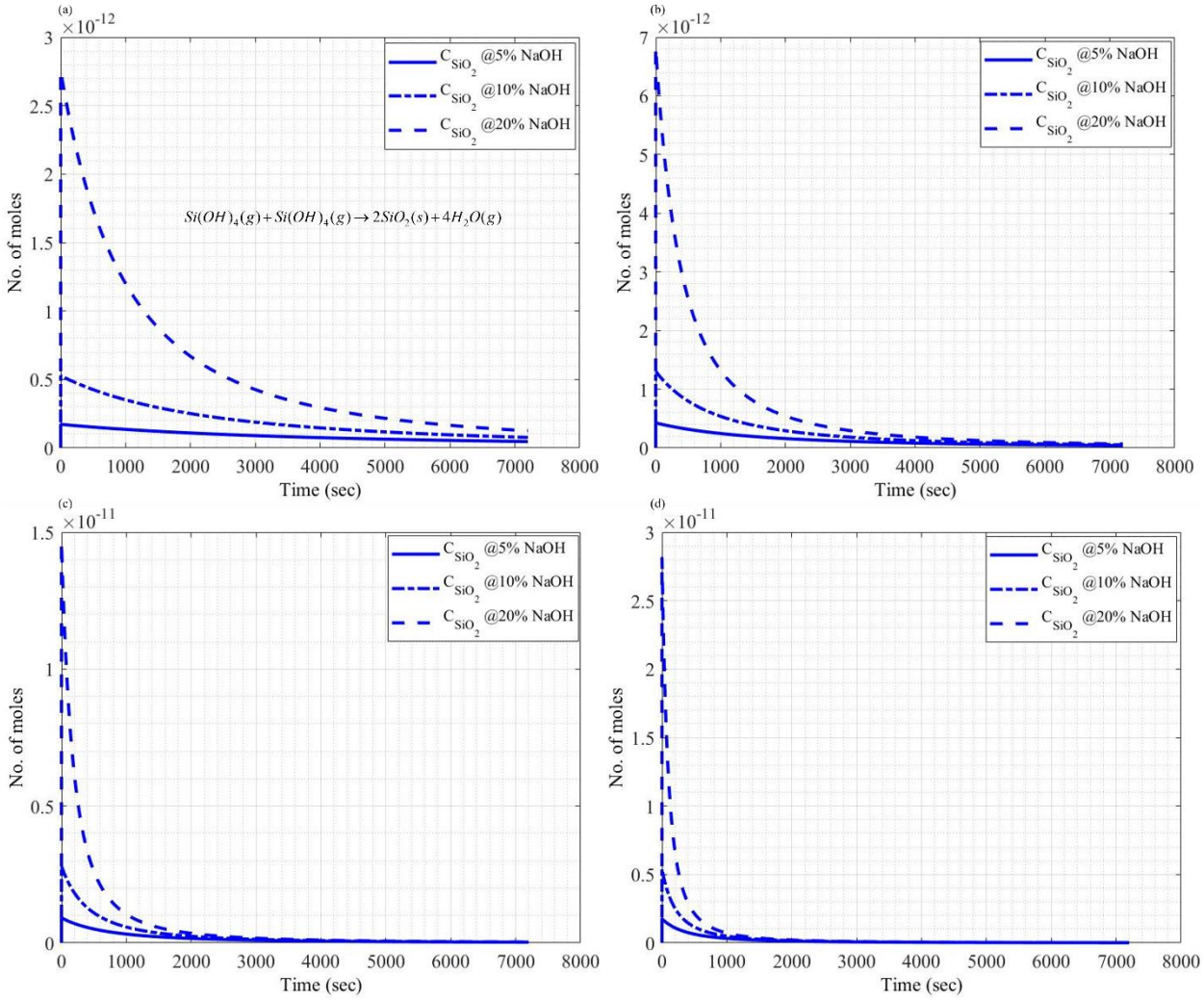

Figure 30: Plots of concentrations of product SiO_2 (blue lines) of equation (7) with respect to time over the sintering temperatures for (a) 800 °C, (b) 900 °C, (c) 1000 °C and (d) 1100 °C obtained by solving equation (24) given in appendix.

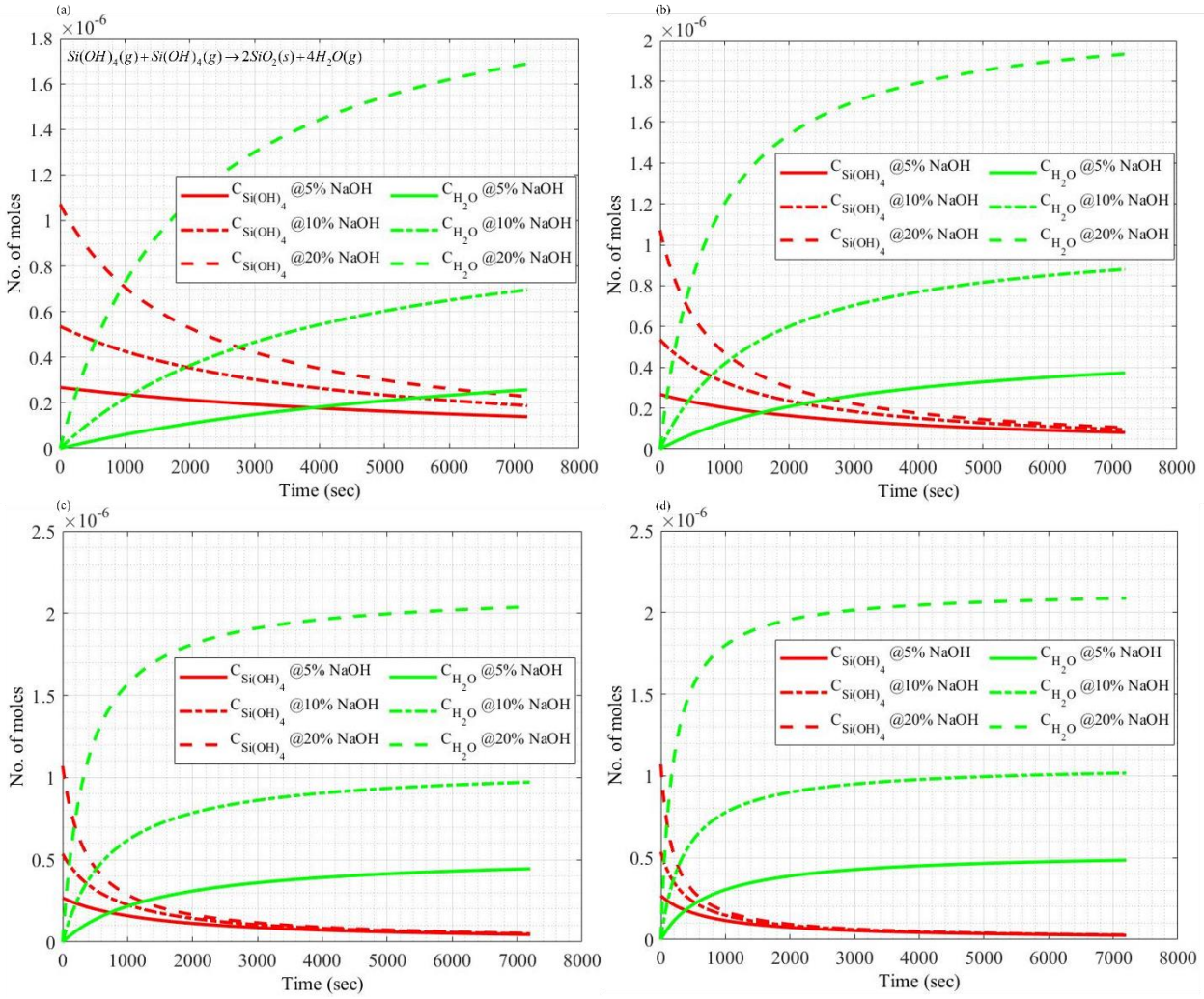

Figure 31: Plots of concentrations of reactants $Si(OH)_4$ (red lines) and product H_2O (green lines) of equation (7) with respect to time over the sintering temperatures for (a) 800 °C, (b) 900 °C, (c) 1000 °C and (d) 1100 °C obtained by solving equation (24) given in appendix.

Figure 32 shows the variation of nanowire lengths (μm) with respect to NaOH concentration obtained from silica nanowire growth model for 800 °C/2 hr and experimental data for 800 °C/2 hr. Modeling results show that the length of silica nanowire increases with increase in the NaOH concentration at 800 °C temperature. Figure 32 shows experimentally measured the average nanowire length as 8 ± 1.2 μm for 5% NaOH, 12.6 ± 3.2 μm 10 % NaOH, and 41 ± 7.0 μm 20% NaOH heat treated at 800 °C/2 hr. It is evident that both model and experimental data for nanowire length shows good agreement with respect at different NaOH concentration.

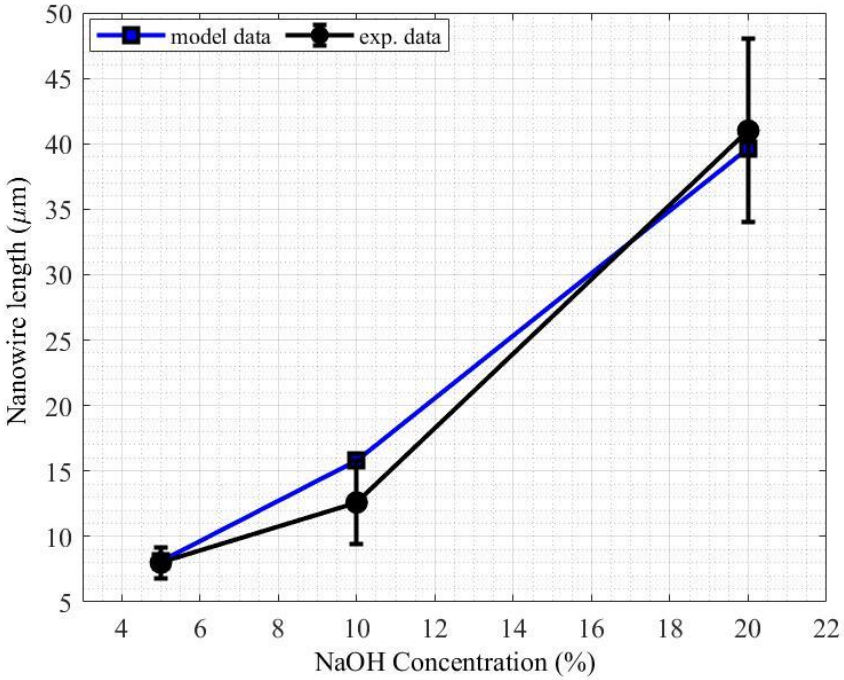

Figure 32: Variation of nanowire lengths (μm) with respect to NaOH concentrations obtained from silica nanowire growth model for 800 °C/2 hr (black line) and experimental data for 800 °C/2 hr (red line).

Figure 33 shows the changes in nanowire lengths (μm) with respect to the sintering temperature (°C) for 10% NaOH concentrations obtained from silica nanowire growth model and experimental data. The silica nanowire length increases as sintering temperature increases from 800 °C to 1100 °C. The model and experimental data in Figure 33 shows a good agreement. Results appear to be linear trend with respect to sintering temperature for 10% NaOH.

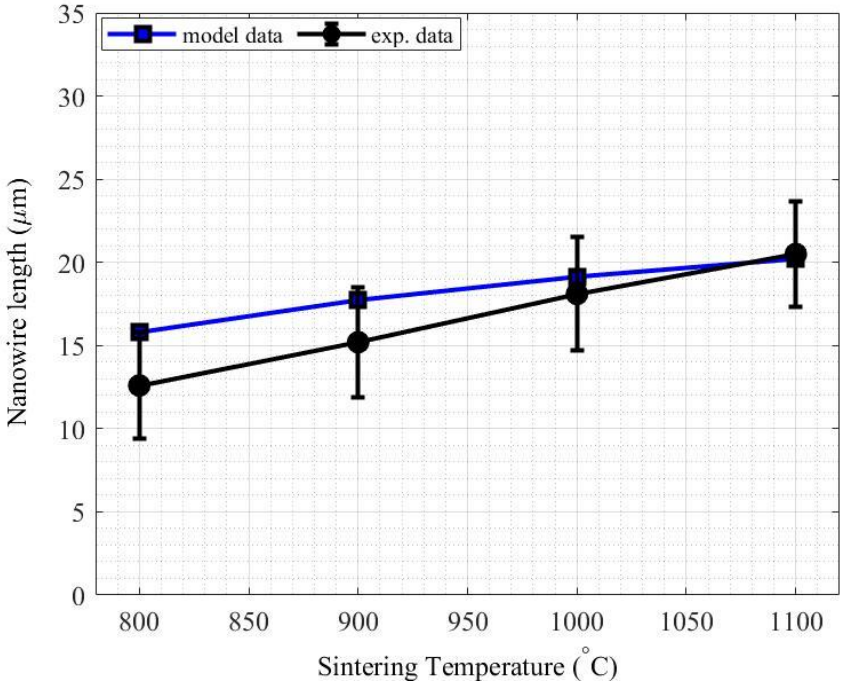

Figure 33: Changes in nanowire lengths (μm) with respect to sintering temperature (°C) for 10% NaOH (blue line) concentrations obtained from silica nanowire growth model and for experimental data (black line).

Figure 34 shows the variation of nanowire lengths (μm) with respect to sintering temperature (°C) for different NaOH concentrations obtained from silica nanowire growth model for 5% NaOH, 10% NaOH, and 20% NaOH. In this figure the growth model predicts change in nanowire length for 5% NaOH concentration and 20% NaOH concentration. As the NaOH concentration increases, from 5% to 20%, the slope of curves shown in Figure 34 also increases.

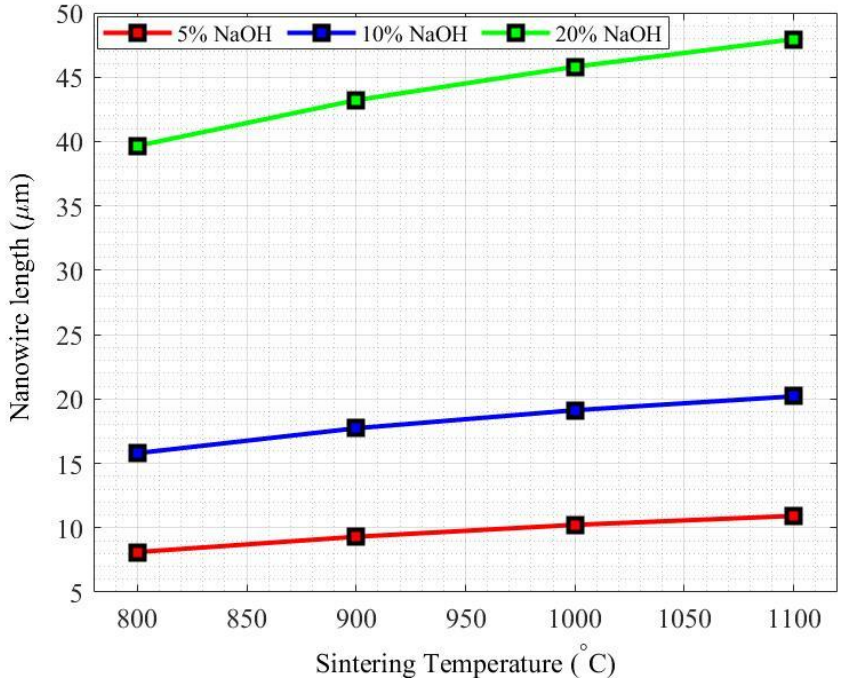

Figure 34: Variation of nanowire lengths (μm) with respect to sintering temperature (°C) for different NaOH concentrations obtained from silica nanowire growth model for 5% NaOH (red line), 10% NaOH (blue line), 20% NaOH (green line).

CHAPTER 4: CONCLUSION

4.1 Conclusion

In this work, the experimental optimization of process parameters for silica nanowire growth inside the pore of 3D printed SiC discs was investigated. The analysis included quantitative SEM image analysis and the development of a mathematical growth model. The goal was to achieve the highest nanowire growth and number density, leading to improved densification and mechanical properties. The use of DSC and TG analysis aids in understanding the nucleation and growth of silica nanowires under different conditions. Increasing the NaOH concentration effectively increased the nanowire number density and size of the nanowire resulted in densification and strengthening of 3D printed SiC discs. However, when NaOH concentration was increased to 20%, sample showed very poor dimensional stability compared to 5 and 10% NaOH. Hence, 10% NaOH was found to be the optimum NaOH concentration that allowed optimal nanowire growth and mechanical performance with good dimensional stability. The results indicated that increasing sintering temperature resulted in increased nanowire number density and length of the nanowire while width measurement showed a similar distribution for all temperatures. Droplets size measurement gathered at 600 °C showed same distribution as nanowire width indicating that the nanowire width is directly related to droplets and doesn’t change with post processing parameters. The optimum sintering temperature and time while using 10% NaOH was found to be 1100 °C and 4 hr that effectively led optimum nanowire growth and number density, leading to improved densification and mechanical properties with good dimensional stability of the 3D printed SiC discs. This work shows a possible roadmap for obtaining a completely dense 3D printed SiC parts by repeating the post processing treatment using the optimum parameters found from this study.

A mathematical model for silica nanowire growth was developed in this work that accounted for the reaction kinetics to form silica molecules and the subsequent deposition of the molecules for nanowire growth. Implementation of this model was done in MATLAB using forward Euler method to solve ODEs. The model developed in this work quantitatively describes the dependence of the length of silica on the NaOH concentration, sintering temperature, and time. Qualitative validation was conducted with the help of SEM images obtained via experimental work. The revealed analytical relation between the nanowire length and the post processing parameters can be used to optimize the process of silica nanowires formation.

4.2 Future work

In this work, the experimental optimization of post processing parameters successfully enhanced silica nanowire growth and mitigated the porosity of 3D printed SiC discs, achieving a porosity level of 38.32%. However, to attain fully dense SiC parts through the Powder Bed Binder Jet (PBBJ) process, a multi-step post processing procedure is required. Hence, the implementation of a multi-step post processing protocol needs to be performed, utilizing the optimal post processing parameters identified in this study.

The mathematical model developed in this study has demonstrated its efficacy in predicting the relationship between nanowire length and various post processing parameters. However, it is crucial to note that the model currently overlooks the width of the nanowire. Experimental observations have indicated that the width of nanowires is governed by the width of the droplets, a factor not accounted for in the existing model. However, the width of nanowire wasn’t considered in this model as the experimental work suggested that the droplets width controls the width of nanowires. Therefore, in order to comprehensively capture the growth mechanism of silica nanowires, it is essential to incorporate the physics of the nucleation process

into the model. This refinement will enhance the accuracy and completeness of the model, providing a more comprehensive understanding of silica nanowire growth. Further development will be needed in order for model to predict mechanical properties such as strength, density, and porosity.

PART II

IN SITU MINERALIZATION

CHAPTER 5: INTRODUCTION

5.1 Challenges of manufacturing SiC

Silicon carbide (SiC) stands out as a highly promising material for a diverse array of high-temperature applications, encompassing critical components for diesel engines, gas turbines, industrial heat exchangers, fusion reactor parts, filters designed for elevated temperature environments, wear-resistant components adaptable to various conditions, medical implants, and even mirrors tailored for space applications [141-145]. The thermomechanical properties of SiC are inherently linked to its strong Si–C covalent bond. Nonetheless, a notable challenge in achieving a dense SiC object lies in its inherent difficulties, specifically low sinterability and the limited formation of a silica bonding zone between SiC particles through thermal oxidation, even under high sintering temperatures.

5.2 Mechanism of thermal oxidation of SiC

The process of thermal oxidation leads to the generation of CO gas, which is released into the air, ultimately leaving a silicon oxide surface layer. This silicon oxide layer contributes to the partial fusion of SiC particles, giving rise to a porous matrix with compromised mechanical properties. Attempts to improve the mechanical characteristics of this porous matrix by increasing the thickness of the silicon oxide layer have faced challenges, primarily attributed to the poor diffusion coefficient of oxygen within SiC. SiC is a highly covalent material, approximately 88% of the bonding between Si and C atoms is covalent, with the remaining 12% being ionic, rendering the diffusion of oxygen atoms into SiC particles difficult without the need for exceedingly high temperatures with longer dwelling time and ultra-high pressures [146]. For instance, Nadeau et al. [147] successfully achieved full densification of SiC at 2500 °C and 5 GPa without the use of sintering additives. Moreover, the extended duration of high-temperature

exposure during thermal oxidation leads to weight losses and abnormal grain growth, accompanied by the formation of anisotropic α - SiC phase.

5.3 Approaches to overcome difficulty of SiC thermal oxidation

Many efforts have been directed to reduce the SiC sintering temperature using two main mechanisms: (1) solid phase sintering mechanism and (2) liquid phase sintering mechanism.

5.3.1 Solid phase sintering mechanism

Solid-phase sintering is a process used to consolidate and densify powdered materials into a solid mass without melting them. It involves heating the powdered material to a temperature below its melting point, where diffusion of atoms or molecules leads to the formation of strong bonds between particles. Solid-state sintering allows for the production of high purity SiC materials with excellent density control. This results in materials with superior mechanical and thermal properties. However, it also comes with challenges like high-temperature requirements, longer processing times, limitations on geometric complexity, and potential brittleness. Solid phase sintering of SiC requires an additive which can reduce the grain boundary-surface energy ratio of the SiC particles for the purpose of densification process. This can create a driving force that promotes the movement of particles during the sintering process. More commonly, additives like boron (B), carbon (C) [148], B_4C [149], and Al_3BC_3 [150] have been employed in the solid-phase sintering of SiC without the application of external pressure. However, this method demands extremely high temperatures, often exceeding 2150 °C. Even with the incorporation of these additives and the elevated sintering temperatures, achieving full densification of SiC remains challenging. This difficulty arises from Si-C covalent bonding nature and its low self-diffusion coefficient, which impedes the mass transport mechanism necessary for achieving complete densification.

5.3.2 Liquid phase sintering mechanism using mullite

The most preferred sintering approach for SiC is liquid phase sintering, which effectively addresses the limitations associated with the solid-state sintering method. Liquid phase sintering is a process for consolidating a powder material by partially melting the substance being sintered. This partial melting is achieved by introducing a low-melting-point liquid component, through the use of additives. The presence of this liquid phase significantly enhances mass transport mechanisms, reducing sintering time and temperatures. As a result, it leads to improved densification, a uniform microstructure, faster processing rates, and greater control over material properties compared to solid-phase sintering. Full densification of SiC ceramics can be achieved through liquid phase sintering by incorporating various metal oxide additives like rare-earth oxides or by adding substances such as Al_2O_3, Y_2O_3, CaO, MgO [151-162]. However, it's worth noting that even with these additives, high temperatures ranging from 1700 to 2100 °C are required, which can increase the production cost of SiC components immensely and limit their widespread use. The utilization of oxide additives like SiO_2 [163], cordierite ($2MgO.2Al_2O_3.5SiO_2$) [164-166], mullite ($3Al_2O_3.2SiO_2$) [8, 167-174] and glassy phases [175] has gained a lot of interest. This approach enables the liquid phase sintering of SiC ceramics at lower temperatures, typically around 1400-1600 °C, which leads to a significant reduction in manufacturing costs.

Recently, the in-situ mullite liquid phase sintering mechanism has gained increased attention due to its excellent compatibility with SiC, particularly in comparison to other oxide additives. Mullite, with a coefficient of thermal expansion (5.3×10^{-6} /K at 273-1273 K) similar to SiC (4.7×10^{-6} /K at 293-973 K) and good chemical compatibility with SiC [176-181], ensures a strong interfacial bonding between SiC and the mullite phase. Moreover, mullite exhibits high

oxidation resistance due to its low oxygen diffusion coefficient [171]. Therefore, numerous studies have concentrated on the in-situ synthesis of the mullite liquid phase at the joints of SiC particles to enhance adhesion strength between SiC particles, thereby promoting elevated mechanical strength and improved resistance to thermal shock. Various powders, such as Al_2O_3, Al, AlN, and $Al(OH)_3$ have been employed to form mullite through reactions with oxidation-derived SiO_2 on the surface of SiC particles [171, 181]. However, the in-situ formation of mullite by solid reaction between Al_2O_3 and SiO_2 is constrained by the slow solid diffusion speed of Al^{3+}, necessitating prolonged thermal treatment above 1500 °C for completing the mullitization reaction [182]. Such high temperatures in air lead to excessive oxidation of SiC, diminishing the thermomechanical properties of the SiC-mullite composite due to the formation of excess of cristobalite (SiO_2) phase, which has lower strength and introduces a significant coefficient of thermal expansion (CTE) mismatch between SiC (4.7×10^{-6} /K at 293-973 K) and cristobalite phase (17.5×10^{-6} /K at 273-1273 K) [183]. Utilizing $Al(OH)_3$ to induce mullite phase formation in the SiC-mullite composite required temperatures exceeding 1400 °C [184]. However, at this temperature range, the mullitization reaction remained incomplete, leading to suboptimal mechanical performance. Subsequent sintering at 1550 °C/6 hr achieved near-complete mullitization, as evidenced by the disappearance of diffraction peaks related to the aluminum source. Nevertheless, this process resulted in high-intensity cristobalite diffraction peaks, presenting challenges in achieving favorable mechanical properties for the composite. The introduction of sintering aids, such as yttria (Y_2O_3) [185] or Y_2O_3+CaF_2 [186], effectively eliminated the cristobalite phase. However, the elevated sintering temperature (1550 °C/4 hr) led to poor interfacial adhesion strength between SiC and the mullite phase, resulting in SiC-mullite composites with compromised mechanical strength and thermal shock resistance.

5.4 Use of coal ash as a source of mullite

In this study coal fly ash was utilized as the precursor for in-situ mullite phase formation through a liquid phase sintering mechanism. A finely powdered byproduct of coal combustion in coal-fired power plants, coal fly ash emerges as a fine and powdery substance. Its incorporation in the composite formulation aids in reducing the required sintering temperature. The coal ash powder composition includes approximately 45 wt% α-Al2O3, 42 wt% SiO2, and various minor concentrations of metal oxides. These metal oxides played a pivotal role in expediting the instantaneous formation of mullite on the surface of SiC particles, achieved at a relatively low temperature (1400 °C/1 hr), thereby promoting a strong interfacial bond between SiC particles. The gradual variation in aluminum concentration at the interface resulted in the creation of a functionally graded SiC-mullite composite with exceptional thermomechanical properties. The study systematically explored the impact of SiC/mullite weight ratios on density, mechanical properties, and thermal shock resistance. Furthermore, it delved into the influence of thermal treatment parameters and coal fly ash particle size on the thermomechanical and electrical properties of the composite.

5.5 Hypothesis

The hypothesis behind this work is that creating a stronger interfacial bond between the particles through in situ formation of mullite ($3Al_2O_3.2SiO_2$) instead of silica layer can lead to formation SiC composite with high thermomechanical properties.

5.6 Objective

The objective of this part of the work is to examine the role of creating liquid mullite bonding agent instead of silica layer for achieving denser SiC composite. In the first part, utilizing optimum growth of silica nanowires and silica layer formation decreased the open

porosity percentage of 3D printed SiC parts to 38%, which is still substantially high. Therefore, the second part of the thesis introduces liquid mullite phase sintering of SiC particles with the goal of creating a denser SiC composite by minimizing the voids between SiC particles and creating a stronger bonding zone.

CHAPTER 6: IN SITU MINERALIZATION OF MULLITE BONDING AGENT FOR SIC COMPOSITE

6.1 Materials and methods

6.1.1 Raw materials

The raw materials utilized in this study included SiC (comprising 40% alpha SiC, 50% beta SiC, and 10% amorphous SiC) with a particle size ranging from 1 to 40 μm, sourced from US Research Nanomaterials in Houston, TX. Additionally, coal fly ash powder from Duke Power, NC, was employed. Deionized water served as a binder during the mixing process.

6.1.2 Disc preparation and processing parameters

6.1.2.1 Effect of sintering temperature

To determine the sintering temperature facilitating the formation and melting of the mullite phase for filling the interspace between SiC particles, a mixture of SiC and coal fly ash (at a weight ratio of 90/10) was pressed at 250 MPa. The sample was then heat-treated at temperatures of 1300 °C, 1400 °C, or 1500 °C for 15 minutes, employing a heating rate of 10 °C/min, followed by overnight cooling. The effect of sintering temperature on the compressive strength of the composites was subsequently evaluated.

6.1.2.2 Effect of SiC/coal fly ash weight ratio

The influence of the SiC/coal fly ash weight ratio on mechanical strength was examined. SiC powder was mixed with coal fly ash at weight ratios of 90SiC/10ash, 85SiC/15ash, 80SiC/20ash, and 75SiC/25ash. To create composite discs, the SiC powder was mixed with the corresponding ratio of coal fly ash for homogeneity. This mixture was then pressed at 250 MPa for 30 minutes to produce discs of 10 mm diameter x 6 mm height. The discs underwent heating

at 100 °C for 8 hours and were then ramped to 1400 °C for 15 minutes. The samples were left to cool to room temperature overnight before assessing mechanical strength.

Since the composition with 85SiC/15ash demonstrated the highest compressive strength, samples with 90SiC/10ash, 80SiC/20ash, and 85SiC/25ash were excluded from further analyses.

6.1.2.3 Effect of coal fly ash particle size

Coal fly ash underwent ball milling for 5 hours at 200 rpm to achieve a reduced particle size (< 38 µm, Table 4) before mixing with SiC to make discs. before being blended with SiC for disc formation. Initially, coal fly ash powder was mixed with alumina balls of 5 mm diameter in a 1:10 ratio, followed by the addition of ethanol (about 20-25% of the mill volume) to ensure complete soaking of the powder and alumina balls. The resulting slurry was loaded into the planetary ball mill jar, with 25% of the jar left empty, and milled for 5 hours. Subsequently, the slurry was dried in an oven at 100 °C for 24 hours. The separated alumina balls were removed from the dried powder mix, and the powder underwent sieving using a set of ASTM standard sieves.

Two sets of 85SiC/15ash discs were then prepared, utilizing either coarse or fine coal fly ash powder, by pressing the mixture at 250 MPa and subjecting it to sintering at 1400 °C for 1 hour. The mechanical strength of these two discs was measured according to the procedure described below.

6.1.2.4 Effect of dwelling time

To determine the suitable dwelling time for optimal liquid-phase sintering of mullite at 1400 °C without deformation due to excessive melting, three sets of 85SiC/15ash discs were prepared and tested at 1400 °C with dwelling times of 15 mins, 45 mins, and 1 hr. Mechanical properties were assessed for these samples.

6.1.3 Characterization

6.1.3.1 Density measurements

The apparent open porosity (Pa, %) and density (D, g·cm^{-3}) were measured by following the Archimedes principle, employing a density determination kit (Ohaus, Parsippany, NJ) and a digital scale (Ohaus, Parsippany, NJ). Pure DI water served as the immersion liquid. The calculation of apparent density (D) was calculated using Eq. (1) [62],

$$D = \frac{m_d}{m_d - m_w}(D_0 - D_L) + D_L, \quad (1)$$

where, m_d is the dry mass of the sample in grams (g), m_w is the mass of the saturated sample in water (g), D_0 is the density of the DI water (g·cm^{-3}), and D_L represents the air density (0.0012 g·cm^{-3}). The apparent open porosity was determined through Eq. (2) [187],

$$P_a = \frac{m_a - m_d}{m_a - m_w} \times 100\%, \quad (2)$$

where, m_a represents saturated sample mass in the air (g).

6.1.3.2 SEM-EDX morphology analysis

The morphology of the sintered discs, encompassing aspects such as particle fusion, grain boundaries, and porosity, was examined using a JEOL 6480 Scanning Electron Microscope (SEM) equipped with energy-dispersive X-ray (EDX) analysis. Additionally, SEM-EDX was used to analyze the fracture mechanism following the mechanical test. SEM-EDX was employed to investigate the fracture mechanism post-mechanical testing. The microstructural features' elemental composition was analyzed at 20 kV with a working distance of 10 mm, utilizing an Oxford Instruments INCA Energy Dispersive Spectroscopy (EDS) system in conjunction with

the JEOL 6480 SEM. The determination of porosity percentage involved the analysis of 10 SEM images of the fractured surface using ImageJ software.

6.1.3.3 X-ray diffraction analysis (XRD)

The determination of crystalline phases in the SiC-mullite composite and coal fly ash was conducted using a PANalytical X'Pert Pro/MRD instrument. The analysis involved scanning finely crushed powder samples with Cu Kα radiation (wavelength λ = 1.54 Å). The X-ray diffractometer utilized a radiation source operating at 45 kV and 40 mA. The incident beam was contriolled by a 0.25 mm fixed divergence slit, and the diffracted radiation was captured using a 0.1 mm receiving slit. The scanning range encompassed 2θ angles from 5° to 90°, and continuous data collection with a step size of 0.002° was employed.

For phase quantification analysis of the SiC-mullite composite and coal fly ash powder, Rietveld refinement software MAUD [188] was utilized. The refinement process involved fitting calculated diffraction patterns to observed data by adjusting parameters describing crystal structures and peak shapes, as well as scaling factors for each phase. These scaling factors provided the percentage amount of each phase, normalized relative to all scaling factors and multiplied by 100. The iterative refinement aimed for the best fit between calculated and observed diffraction patterns. Statistical R factors obtained by Rietveld analysis were found to be < 10, indicating good fitting between calculated and observed diffraction patterns. The crystallite size was calculated using Scherrer's formula (equation 25) [189]:

$$D_{hkl} = \frac{K\lambda}{\beta \cos\theta}, \tag{25}$$

where, D_{hkl} is the crystallite size, K is the Scherrer constant, which is 0.89, and β is the full width at half maximum of the diffraction peaks for SiC (006), mullite (210), α cristobalite (101), and β cristobalite (111), and θ is the Bragg angle.

6.1.3.4 Fourier transform infrared spectroscopy (FTIR)

The SiC-mullite composite powder underwent analysis using FTIR (Fourier Transform Infrared Spectroscopy) in the diffuse reflectance mode (DRIFT) on a Nicolet 6700 instrument from Thermo-Nicolet in Madison, WI. This analysis aimed to identify the various chemical bonds present in the composite.

6.1.3.5 Mechanical testing

The mechanical properties of the thermally treated SiC-mullite composites were assessed utilizing an Instron 5582 machine at a temperature of 25 °C in an air environment. The samples underwent compression at a rate of 2 mm/min until failure, and the resulting stress-strain curves were employed to determine the compressive strength of the composites.

6.1.3.6 Hardness

The hardness of the composite was determined using a Vickers Hardness testing machine (Wilson Instruments, 402MVD). A pyramid-shaped diamond indenter with an applied load of 2.9 N (300 gf) and a dwelling time of 15 s was used for indentation. Indentations were made at 10 different locations on the sample (85SiC/15ash), and their mean and standard deviation were calculated. The Hardness value HV (GPa) was calculated using the formula in equation (26):

$$HV = 1.854\frac{P}{d_a^2}, \tag{26}$$

where, P is the applied load in Kg, d_a is the average of the indented diagonals in mm.

6.1.3.7 Modulus of elasticity

Nanoindentation was conducted at 25 °C on polished surfaces of the composites using a Berkovich diamond tip on a NanoIndenter (Agilent G200, USA). Continuous stiffness measuring (CSM) mode was applied with a maximum depth of 600 nm and a strain rate of 0.05 s^{-1}. For each distinct phase (SiC and mullite) of the composite in sample 85SiC/15ash, at least 10 indents were applied, and the modulus of elasticity was automatically calculated according to the standards of instrumented indentation (Oliver–Pharr method). Calibration of the indenter was conducted prior to the measurement by measuring Young's modulus and hardness of a silica standard.

6.1.4 Thermal shock resistance

The SiC-mullite discs were subjected to heating at 1400 °C for 15 mins to achieve thermal equilibrium, followed by quenching in liquid nitrogen (LN) at -196 °C for 10 mins, in accordance with the ASTM standard for quenching (ASTM:C1525-18). The discs were then removed from the LN and placed on an alumina plate at 25 °C. Subsequent analyses were performed to assess the dimensions, structure, and mechanical properties of the discs both before and after quenching. The thermal shock resistance experiment was conducted twice on two different sets of samples, and the results were averaged for accuracy.

6.1.5 Electrical and thermal properties measurement

The direct current (DC) electrical conductivity was evaluated from 25 °C to 1000 °C in an air atmosphere on SiC-mullite disks (sample 85SiC/15ash) using the four-point probe method. A conductive paste electrode was applied to the specimen surfaces before positioning it between two potentiostat meshes. Subsequently, the potentiostat meshes were connected with the ends of cell cables, and the sample setup was subjected to a temperature ramp from room temperature to

1000 °C within a tube furnace. Electrical conductivity measurements were conducted at every 100 °C increment.

For thermal characterization, the thermal diffusivity and specific heat capacity were measured at temperatures of -100, 0, 100, 300, 600, 900, and 1000 ºC using the laser flash method with a NETZSCH LFA 467 HT HyperFlashTM instrument [178]. The thermal conductivity was subsequently calculated using the formula provided in Eq. (27)

$$\lambda = \rho \alpha C_p, \tag{27}$$

where, ρ is the density, α is the thermal diffusivity, and C_p is the calculated specific heat value. The thermal expansion coefficient was determined using a NETZSCH DIL 402SU, with the test conducted over the temperature range from -100 °C to 100 °C at a heating rate of 2 °C/min.

6.1.6 Statistical analysis

Statistical analysis of mean differences was conducted using One-Way ANOVA test with Tukey's HSD test for multiple comparisons. A significance level of $p < 0.05$ was applied to determine statistical significance.

6.2 Results

6.2.1 Phase composition and microstructure of the composite

The phase composition analysis of coal fly ash powder and the SiC-mullite composite (sample 85SiC/15ash) sintered at 1400 °C/1hr is presented in Figure 35, with corresponding weight percentages of different phases detailed in Table 3. It can be seen from the analysis that the coal fly ash powder is composed of corundum (α-Al_2O_3) and quartz (SiO_2), mullite ($3Al_2O_3.2SiO_2$), and haematite (Fe_2O_3) phases. For coal fly ash, the d-spacing for the (104) plane was shifted to a lower value from 2.55126 (PDF) to 2.55033 (XRD) due to shift between

observed and known position of α-Al_2O_3 (104) peak (35.147° 2θ PDF card 04-014-1368). The coal fly ash used in this study is categorized as Class F, primarily due to its elevated silica content, approaching 50%. Class F coal fly ash typically contains minimal calcium oxide (CaO), usually less than 5%. Literature data indicate that under conditions of high temperature and pressure, Ca^{2+} can incorporate into the alumina structure [190]. Thus, alumina exists as a solid solution due to the incorporation of Ca^{2+} ions during the formation of coal ash at an extremely high temperature, approximately 2500 °C, within the energy station. The XRD analysis of the SiC-mullite composite reveals the presence of SiC 6H, mullite ($3Al_2O_3.2SiO_2$), and β cristobalite (SiO_2), with a complete absence of α-Al_2O_3 confirming the successful formation of in-situ mullite in the SiC-mullite composite. Additionally, the mullite phase content increased from 0.8 wt% in coal fly ash to 11.4 wt% in the SiC-mullite, as the composite was formulated through the blending of 85 wt% SiC with 15 wt% coal fly ash. This quantitative analysis is detailed in Table 3.

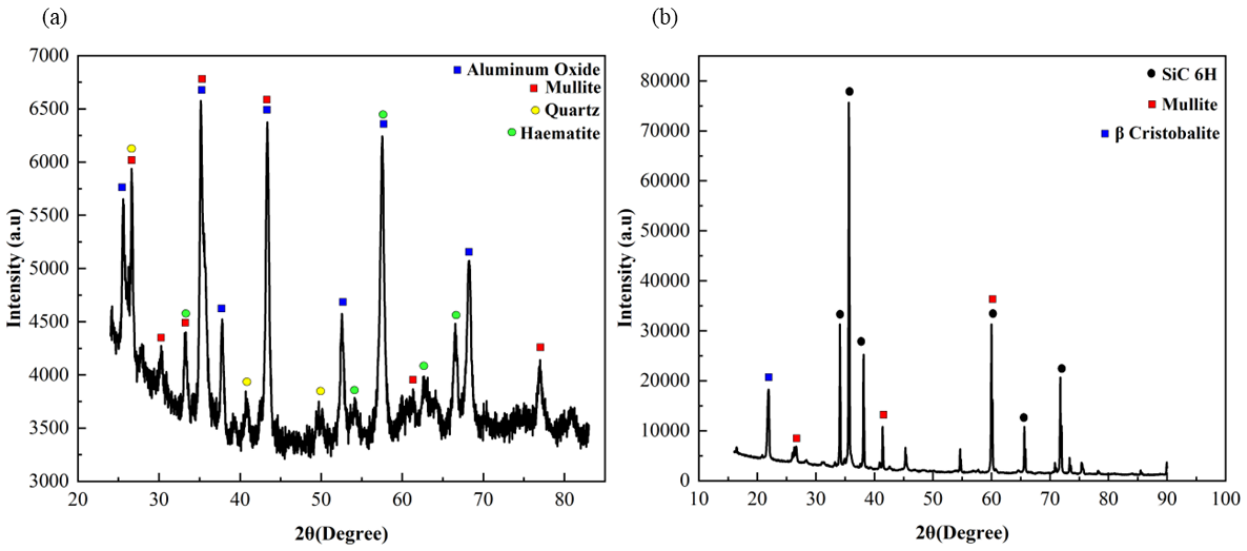

Figure 35: (a) The X-ray diffraction analysis of the coal fly ash powder sample reveals distinctive signals corresponding to crystalline phases, including corundum (α-Al_2O_3) solid solution and quartz (SiO_2), mullite ($3Al_2O_3.2SiO_2$), and haematite (Fe_2O_3) phases. (b) Following heat treatment at 1400 °C/1hr, the X-ray diffraction pattern of the 85SiC/15ash sample exhibits characteristic signals of SiC 6H, mullite ($3Al_2O_3.2SiO_2$) solid solution, and β cristobalite (SiO_2) solid solution [191].

Table 3: Quantitative assessment of different crystalline phases in coal fly ash and SiC-mullite (sample 85SiC/15ash), formed at 1400 °C/1hr, was computed by analyzing the peak intensity of their characteristic peaks [191].

Compositions	Phase Content (wt%) in Coal Fly Ash	Phase Content (wt%) in 85SiC/15ash sample before sintering	Phase Content (wt%) in 85SiC/15ash sample after sintering
α-Al_2O_3	45.6 ± 4.2	6.8 ± 0.6	0
Mullite	5.3 ± 1.1	0.8 ± 0.1	11.4 ± 0.5
Haematite	7.1 ± 0.3	1.1 ± 0.04	0
β quartz	42.2 ± 0.5	6.3 ± 0.1	0
β cristobalite	0	0	6.8 ± 0.2
SiC	0	85	81.8

Figure 36 demonstrates the uniform distribution of diverse microstructures in the SiC-mullite composite. Strong interconnectivity is observed among the large SiC particles, facilitated by a liquid mullite phase, while concurrently, a silica layer forms in close proximity to the surfaces of the SiC particles.

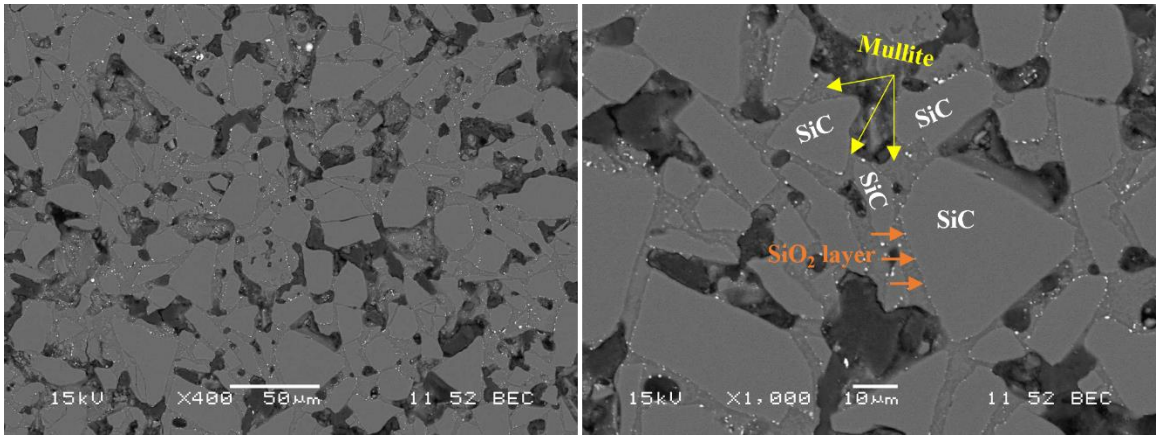

Figure 36: SEM-BSC images of the polished surface of SiC-mullite (85SiC/15ash samples) after heat treatment at 1400 °C/1hr reveal that the outer surface of SiC is coated with a SiO2 layer (indicated by the orange arrow), and the bonding between SiC particles is facilitated by the mullite phase (highlighted by the yellow arrow) [191].

EDX analysis (Figure 37) of spots A and B reveals the presence of Si and C only, indicating the presence of SiC particles. Spots C and D exhibit the presence of Al and O in

addition to Si, with a complete absence of carbon, suggesting the presence of mullite in the interspace between SiC particles. Spot E indicates the presence of a silicon oxide zone immediately at the surface of SiC, consistent with the microstructural distribution observed in Figure 36. Another notable observation is the gradual increase in Al atomic percentage from 4.17% at the boundary of the SiC particle (spot F) to 7.52% at the mullite interphase (spot G), suggesting an Al concentration gradient.

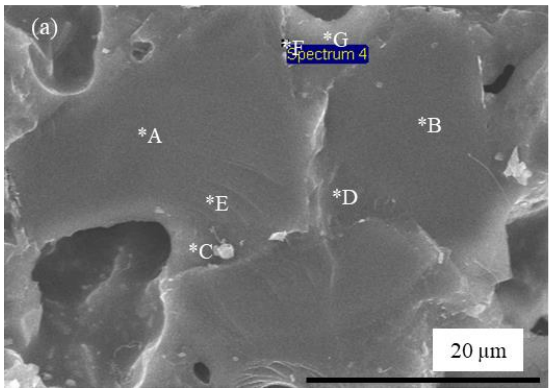

(b)

Spot	C atomic %	Si atomic %	Al atomic %	O atomic %
A	53.6	46.4		
B	44.15	55.85		
C		37.55	7.69	54.75
D		50.23	8.09	41.68
E	52.03	45.61		2.36
F	47.83	28.68	4.17	19.32
G		43.25	7.52	49.23

Figure 37: (a) Fracture analysis using SEM of SiC-mullite (85SiC/15ash samples) after heating at 1400 °C/1hr and (b) Elemental composition analysis using EDX, indicating the main phases (spots A, B, C, and D) and showcasing the gradual increase in Al concentrations (spots F and G) within the composite [191].

In Figure 38 the schematic illustrates the generation of a mullite bonding layer between two SiC particles, highlighting the ionic diffusion of Al^{3+} into the silica layer. This process creates a concentration gradient between the SiC and mullite phase.

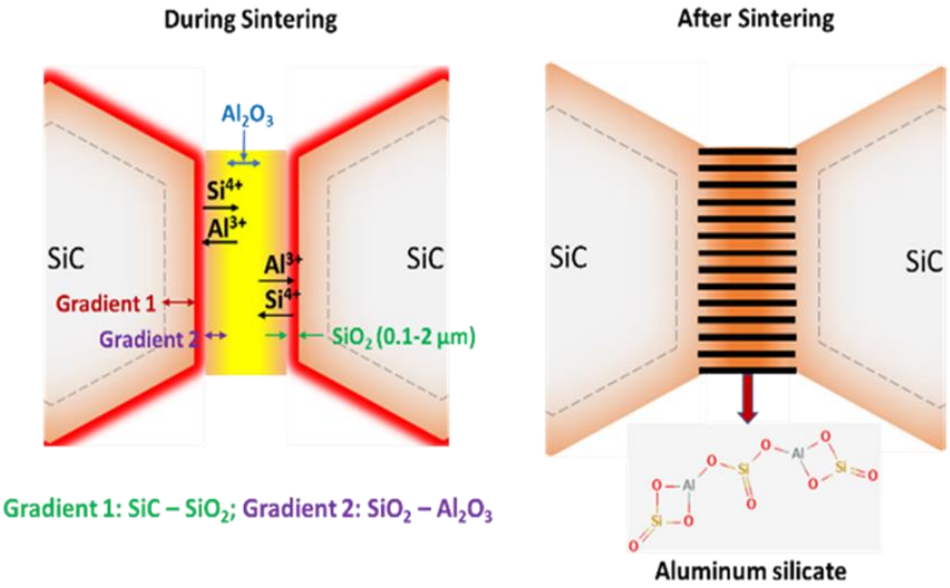

Figure 38: The schematic illustration depicting the formation of secondary mullite phase between SiC particles during the sintering process [191].

6.2.2 Mechanical properties measurement

6.2.2.1 Compressive strength

6.2.2.1.1 Effect of sintering temperature on the compressive strength

Figure 39a illustrates that the mechanical strength of the 90SiC/10ash sample, treated at 1400 °C/15 mins, is significantly superior to samples subjected to heat treatments at 1300 °C/15 mins ($P < 0.004$) or 1500 °C/15 mins ($P < 0.035$). Conversely, the 90SiC/10ash sample treated at 1500 °C exhibited higher strength than that treated at 1300 °C; however, this difference did not reach statistical significance.

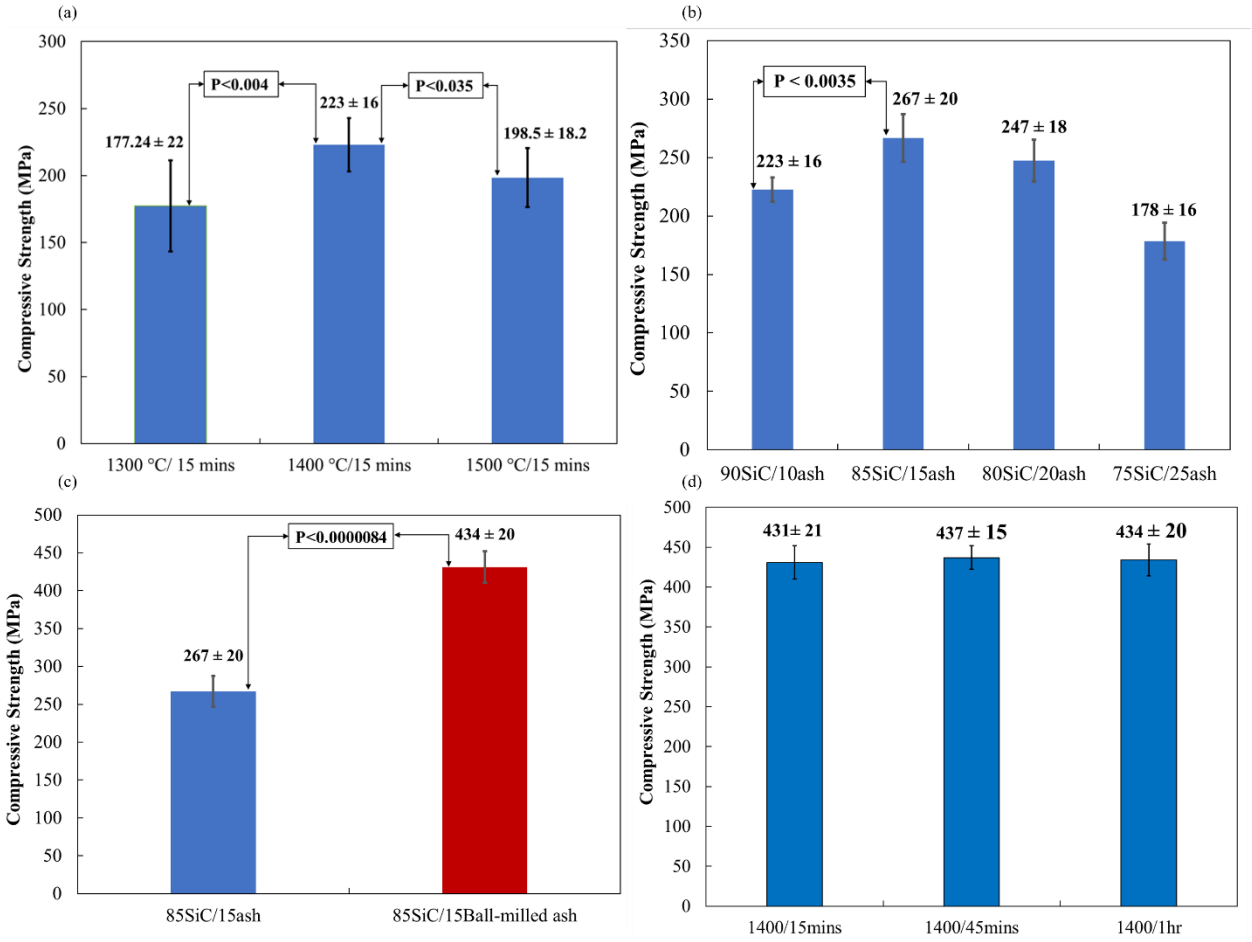

Figure 39: Mechanical properties of (a) cylindrical samples with a composition of 90SiC/10ash, pressed at 250 MPa/30 min and sintered at various temperatures for 15 min, (b) Samples with different weight percentages of SiC/coal fly ash ratios; namely, 90SiC/10ash, 85SiC/15ash, 80SiC/20ash, and 75SiC/25ash, pressed at 250 MPa/30 min and heated treated at 1400 °C/15 min, (c) Samples of 85SiC/15ash, both ball-milled and non-ball-milled, pressed at 250 MPa/30 min and heat-treated at 1400 °C/1hr, and (d) Samples of 85SiC/15ash pressed at 250 MPa/30 min and heat treated at 1400 °C for 15 mins, 45 mins, and 1 hr [191].

6.2.2.1.2 Effect of SiC/coal fly ash weight ratio on the compressive strength

In Figure 39b, the compressive strength of SiC-mullite composites, fabricated with varying percentages of coal fly ash powder (samples: 90SiC/10ash, 85SiC/15ash, 80SiC/20ash, and 75SiC/25ash), is depicted. The average compressive strength exhibited a notable increase in the sequence 85SiC/15ash > 80SiC/20ash > 90SiC/10ash > 75SiC/25ash.

6.2.2.1.3. Effect of coal fly ash particle size on the compressive strength

To investigate the influence of coal fly ash powder particle size on the mechanical strength of the SiC-mullite composite (sample 85SiC/15ash), the ash powder was subjected to ball milling, resulting in a reduced particle size of < 38 µm. The particle size analysis was conducted using a set of ASTM standard sieves, and Table 4 provides an overview of the approximate particle size of the coal fly ash powder before and after ball milling. The mechanical strength of samples prepared using the fine ash powder was measured and compared to that of samples prepared with coarse coal fly ash powder, as illustrated in Figure 39c.

Table 4: Particle size distribution of coal fly ash powder determined through a sieving process [191].

Particle size, P (µm)	Before ball milling (wt%)	After ball milling (wt%)
P < 38	31.74 %	100 %
45 ≥ P > 38	5.5 %	00 %
90 ≥ P > 45	20 %	00 %
150 ≥ P > 90	15.6 %	00 %
250 ≥ P > 150	11.2%	00 %
425 ≥ P > 250	16 %	00 %

6.2.2.1.1 Effect of dwelling time on the compressive strength

Figure 39d illustrates that the mechanical strength of sample 85SiC/15ash treated at 1400 °C/45 mins (437 ± 15 MPa) is slightly higher than the samples treated at 1400 °C/15 mins (431 ± 21 MPa) and 1400 °C/1 hr (434 ± 20 MPa). However, this difference does not reach statistical significance. Considering the uniformity of the sintering process observed in the sample, the optimal dwelling time was determined to be 1 hr at 1400 °C.

6.2.2.2 Hardness and nanoindentation elastic modulus

Figure 40 presents the nanoindentation elastic modulus measurement of SiC and mullite phases. To mitigate the influence of surface effects during measurements, the modulus of elasticity was computed at a depth ranging from 300 to 400 nm. Statistical analysis for SiC

particles within the SiC-mullite composite revealed consistent values of the modulus of elasticity in the depth ranges of 300-350 nm and 350-400 nm (Figure 41). Specifically, the calculated modulus of elasticity for SiC at 350 nm depth was 410 ± 23 GPa. Similarly, for the mullite bonding zone, statistical analysis indicated consistent values of the modulus of elasticity in the depth range of 300-350 nm (Figure 41), with the modulus of elasticity for the mullite phase calculated at 350 nm being 196 ± 21 GPa.

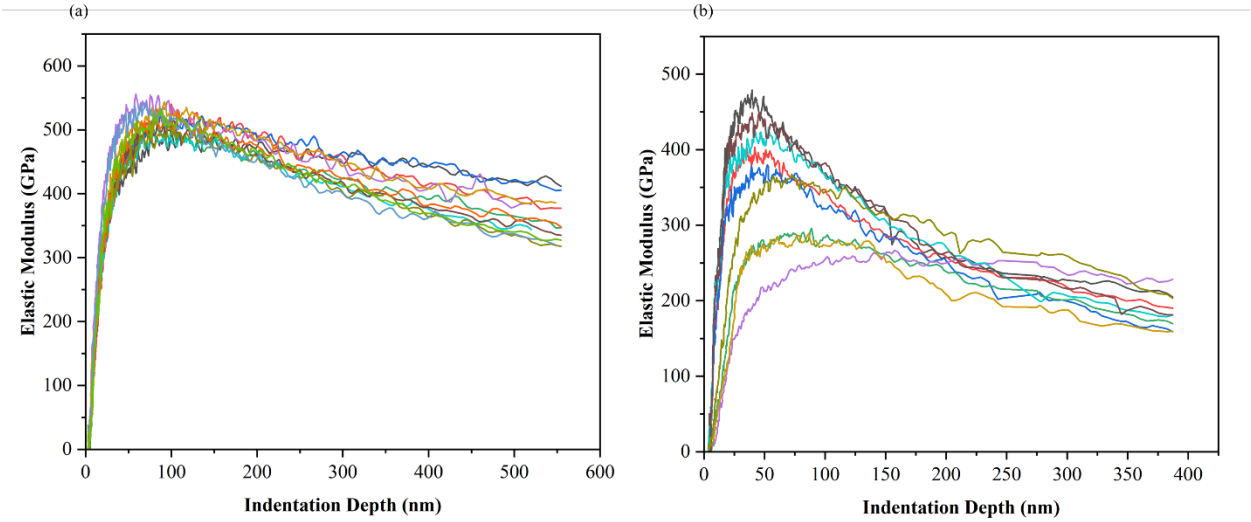

Figure 40: Nanoindentation results depicting the relationship between indentation modulus and indentation depth for (a) SiC phase and (b) mullite phase in the SiC-mullite composite [191].

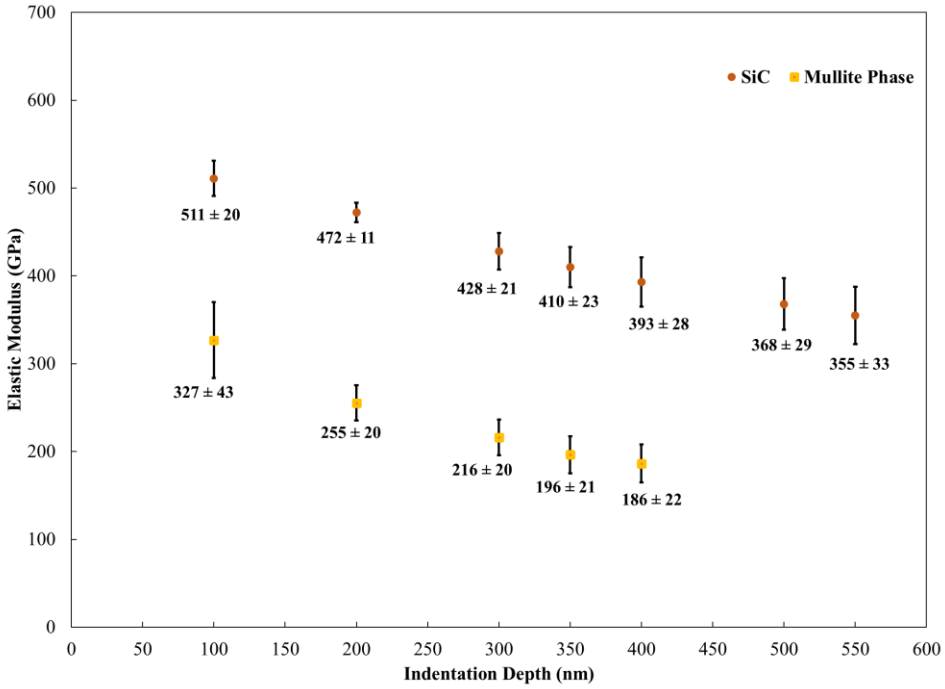

Figure 41: Nanoindentation results illustrating the relationship between indentation modulus and indentation depth for SiC particles (a) and the mullite phase (b) during testing of the SiC-mullite composite [191].

The elastic modulus of the composite can be determined employing a straightforward rule of mixtures, expressed as,

$$E_c = V_{SiC} E_{SiC} + V_M E_M \tag{28}$$

where, E_c, E_{SiC} (410 ± 23 GPa), and E_M (196 ± 21 GPa) denote the nanoindentation elastic modulus of the SiC-mullite composite, SiC, and mullite phase, respectively. Additionally, V_{SiC} (81.73 %) and V_M (18.26 %) represent the volume fraction of the SiC and mullite phases within the composite. Through this formula, the modulus of elasticity for the SiC-mullite composite at an indentation depth of 350 nm was calculated to be 370.9 ± 22.6 GPa..

6.2.3 Density and porosity (%) measurements

Table 5 presents the apparent density of the SiC-mullite composite, determined through the Archimedes principle, alongside the theoretical density calculated using a rule of mixtures based on the actual density of each pure phase: SiC (40% alpha SiC, 50% beta SiC, and 10%

amorphous SiC: 3.12 g.cm-3), mullite (2.23 g.cm-3), and cristobalite (2.35 g.cm-3). The observed apparent density of the composite is noted to be 79% of the theoretical density. Porosity measurements, conducted using both Archimedes principles and SEM image analysis, reveal low porosity values of 3% and 8.2%, respectively.

Table 5: The density and porosity data for the SiC-mullite composite are summarized in the table below [191].

SiC-mullite composite	Apparent Density ($g \cdot cm^{-3}$) (Archimedes principle)	Theoretical Density ($g \cdot cm^{-3}$) (Rule of mixtures)	Apparent open porosity (%) (Archimedes principle)	Porosity (%) (SEM image analysis)
	2.36	2.98	3	8.2

6.2.4 SEM-EDX morphology analysis of fracture surface

In Figure 42, distinctive brittle transcrystalline fracture characteristics are evident, including cleavage marks (indicated by blue arrows) resulting from the propagation path of cracks. These cracks traverse along the cross-section of the grain, halting at the periphery of a pore surface (highlighted by yellow arrows). Notably, the smoothness of the pore surface is attributed to the formation of mullite through the liquid phase sintering mechanism. Additionally, observations include crack deflection (encircled in white) and crack branching (encircled in blue) within the mullite phase.

Figure 42: SEM examination of the fracture morphology in SiC-mullite (85SiC/15ash samples) heat treated at 1400 °C/1hr reveals various fracture characteristics observed on the sample's fracture surface [191].

6.2.5 Thermal shock resistance

Mechanical tests revealed comparable compressive strength for the 85SiC/15ash composite both before (434 ± 20 MPa) and after (439 ± 34 MPa) exposure to thermal shock from 1400 °C/15 min to -196 °C in liquid nitrogen, as illustrated in Figure 43. Moreover, there was no significant alteration in the dimensions of the samples (with a sample size of n = 6) before (10.16 ± 0.004 mm diameter x 5.75 ± 0.04 mm height) and after (10.18 ± 0.01 mm diameter x 5.75 ± 0.04 mm height) the thermal shock, confirming the dimensional stability of the composite.

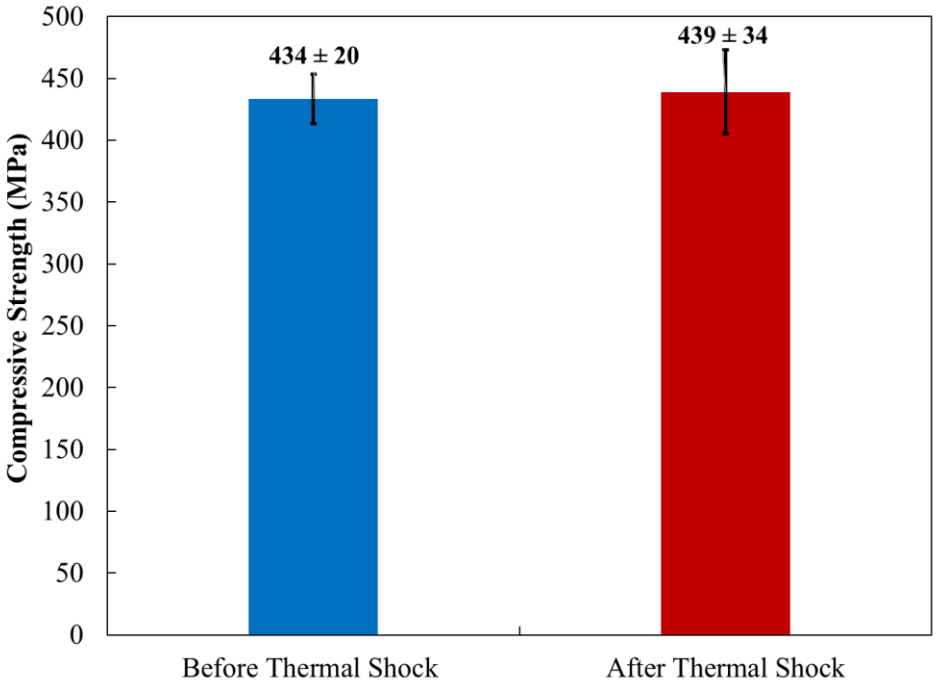

Figure 43: Evaluation of compressive strength for SiC-mullite discs before and after thermal shock [191].

6.2.6 Phase Analysis of SiC-mullite composite before and after thermal shock

The XRD analysis shown in Figure 44a reveals that, following heat treatment at 1400 °C/1h, the SiC-mullite composite (sample 85SiC/15ash) consists of 81.8 wt% SiC 6H, 11.4 ± 0.5 wt% mullite, and 6.8 ± 0.2 wt% β cristobalite (refer to Table 6). Subsequent XRD analysis in Figure 44b of the quenched samples indicates the presence of 80.7 ± 7.6 wt% SiC 6H, 11.8 ± 4.7 wt% mullite, and 7.5 ± 0.83 wt% α cristobalite (Table 6). Table 6 also provides lattice parameters

for SiC, mullite, and cristobalite phases within the composite before and after quenching. The obtained statistical R factors from Rietveld analysis are < 10, indicating a good fit between the experimental and calculated spectra.

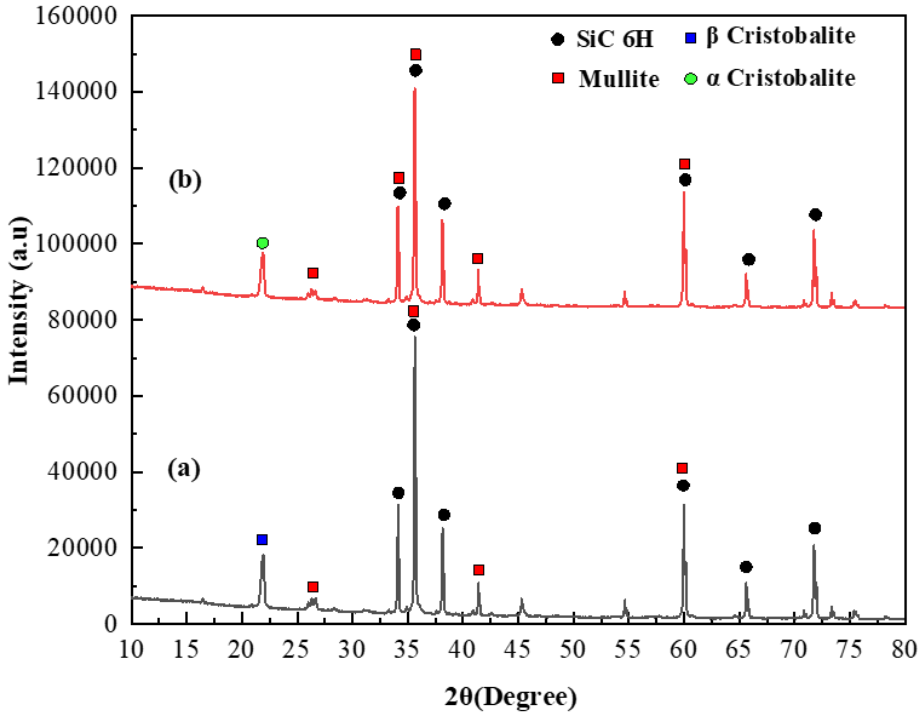

Figure 44: Crystalline phases of SiC-mullite composite following heat treatment at 1400 °C/1hr: (a) prior to quenching, and (b) after quenching in liquid nitrogen [191].

Table 6: Utilizing the MAUD diffraction analysis software, Rietveld refinement was employed to determine the phase composition and structural parameters of the SiC-mullite composite both before and after quenching based on the corresponding XRD data showed in table below [191].

SiC-mullite Sample	Crystalline phase content (wt%)	Crystallite size (Å)	ICDD #	d spacing (PDF)	d spacing (XRD)	Lattice parameters (Å)			Volume (Å^3)
						a	b	c	
Before thermal shock	81.8 wt% SiC 6H	413	04-010-5698	2.516	2.516	3.081	3.081	15.119	124.34
	11.4 wt% mullite	622	04-008-9532	3.405	3.385	7.547	7.693	2.882	168.17
	6.8 wt% β cristobalite	198	04-007-2468	4.116	4.061	7.091	7.091	7.091	362.47
After thermal shock	80.7 wt% SiC 6H	539	04-010-5698	2.516	2.516	3.080	3.080	15.117	124.34
	11.8 wt% mullite	592	04-008-9532	3.405	3.386	7.543	7.692	2.883	168.17
	7.5 wt% α cristobalite	159	04-007-2134	3.976	4.064	5.016	6.919	6.784	163.42

6.2.7 FTIR Analysis SiC-mullite composite before and after thermal shock

Figure 45 illustrates the FTIR spectra for SiC-mullite before and after quenching in the range of 400-1650 cm^{-1}. Additionally, Figure 46 provides a Gaussian fit for the wavenumbers within the 800-1270 cm^{-1} and 400-800 cm^{-1} ranges for samples both before and after quenching. In the quenched sample, new peaks at 1151 cm^{-1}, and 1067 cm^{-1} for the Si-O-Si group were observed, attributed to the transformation of β to α cristobalite phase, a finding confirmed by XRD analysis. The peaks observed in the wavenumber range of 900 to 950 cm^{-1} are associated with Si-O-Al and Al-O stretching [192]. Within the middle region, the band spanning from 700 to 800 cm^{-1} is attributed to Si-O symmetrical stretching vibration within the silicate structure [193]. The lower frequency band vibration at 480 cm^{-1} is a result of Si-O-Si bending modes [193], and the band at 436 cm^{-1} corresponds to Al-O vibration [194]. Consequently, the vibration bands of mullite exhibit overlap with SiO_2 in both the high-frequency (1200 and 900 cm^{-1}) region and low-frequency regions (750 and 400 cm^{-1}). The absorption peaks at 1183 and 1115 cm^{-1} are assigned to Si-O stretching vibration of SiO_4 [195, 196], as well as the peak at 728 cm^{-1}, which is assigned to AlO_4 stretching [197], representing the fundamental bands of the mullite phase. The peak observed at 1550 cm^{-1} is characteristic of Si-C stretching, while the peak centered at 1620 cm^{-1} indicates C=O stretching [101]. A novel peak identified at 888 cm^{-1} in the quenched sample can be ascribed to Si-N stretching, along with C-O and Al-O, possibly formed due to the absorption of nitrogen during the thermal shock process in liquid nitrogen [101, 198]. The peak at 775 cm^{-1} corresponds to Si-O stretching. Additionally, absorbance bands at 620 and 480 cm^{-1} are characteristic peaks of the cristobalite phase[193]. The functional groups corresponding to each band in the FTIR spectra for the samples were assigned in (Table 7).

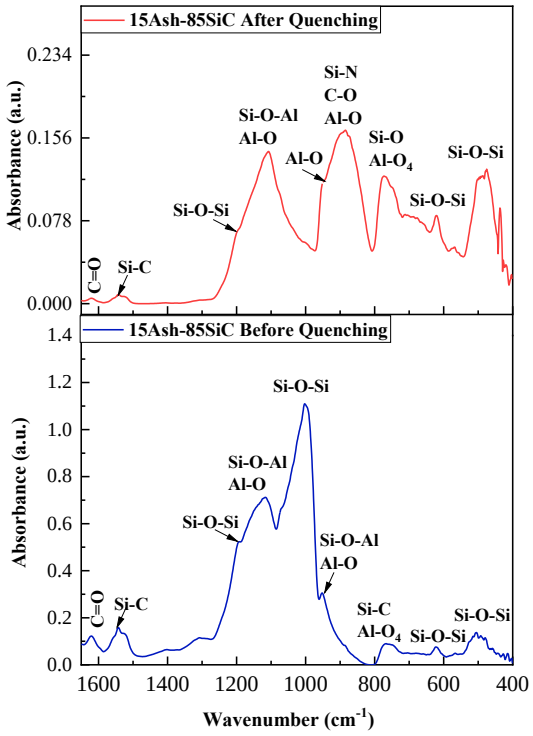

Figure 45: FTIR analysis of 85SiC/15ash composite discs after heat treatment at 1400 °C for 1 hour, depicting the spectra before and after quenching in liquid nitrogen [191].

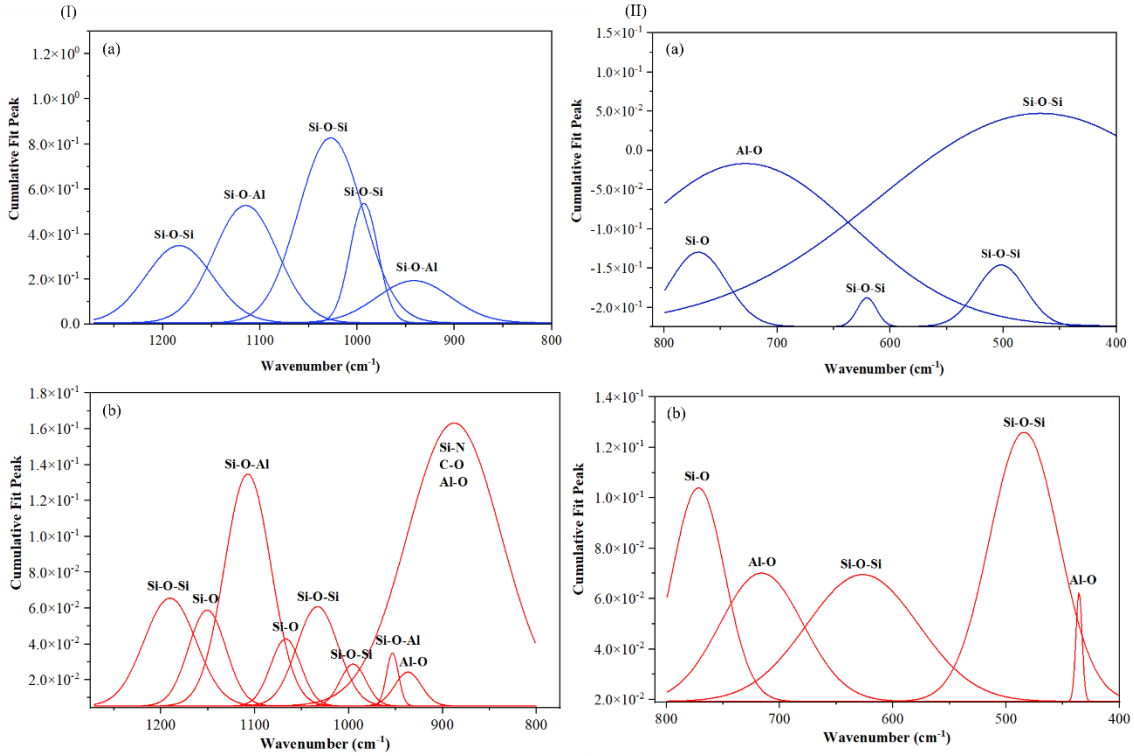

Figure 46: Deconvoluted Gaussian plot illustrating the FTIR spectra of 85SiC/15ash composite discs within the wavenumber ranges (I) 1270-800 cm-1 and (II) 800-400 cm-1 for (a) before quenching, and (b) after quenching [191].

Table 7: Identification and assignment of absorption bands in the FTIR spectra for the SiC-mullite composite (sample 85SiC/15ash) both before and after quenching [191].

Before quenching		**After quenching**	
Wavenumber (cm^{-1})	**Assignments**	**Wavenumber (cm^{-1})**	**Assignments**
1620	C=O stretching	1618	C=O stretching
1550	Si-C stretching	1550	Si-C stretching
1183	Si-O-Si stretching vibration of SiO_4	1190	Si-O-Si stretching vibration of SiO_4
		1151	Si-O Stretching
1115	Si-O-Al stretching, AlO_4	1108	Si-O-Al stretching, AlO_4
		1067	Si-O-Si, Si-O stretching
1027	Asymmetric in-plane Si-O-Si stretching vibration	1033	Asymmetric in-plane Si-O-Si stretching vibration
993		995	
		953	
942	Si-O-Al stretching, Al-O stretching	934	Si-O-Al stretching, Al-O stretching
		888	Si-N stretching, C-O stretching
770	Si-O symmetric stretching	772	Si-O symmetric stretching
728	AlO_4 stretching	716	AlO_4 stretching
627	Si-O-Si out-of-plane vibration	627	Si-O-Si out-of-plane vibration
502	Si-O-Si bending	484	Si-O-Si bending
467	Si-O-Si deformation vibration	436	AlO_6

6.2.8 Electrical and thermal properties of the SiC-mullite composite

Figure 47a illustrates the electrical conductivity of the SiC-mullite composite, measured across a temperature range from 0 °C to 1000 °C. The electrical conductivity of the SiC-mullite composite began to rise at approximately 400 °C, showing an increase from 1.38×10^{-4} at 400 °C to 3.48×10^{-2} Sm^{-1} at 1000 °C.

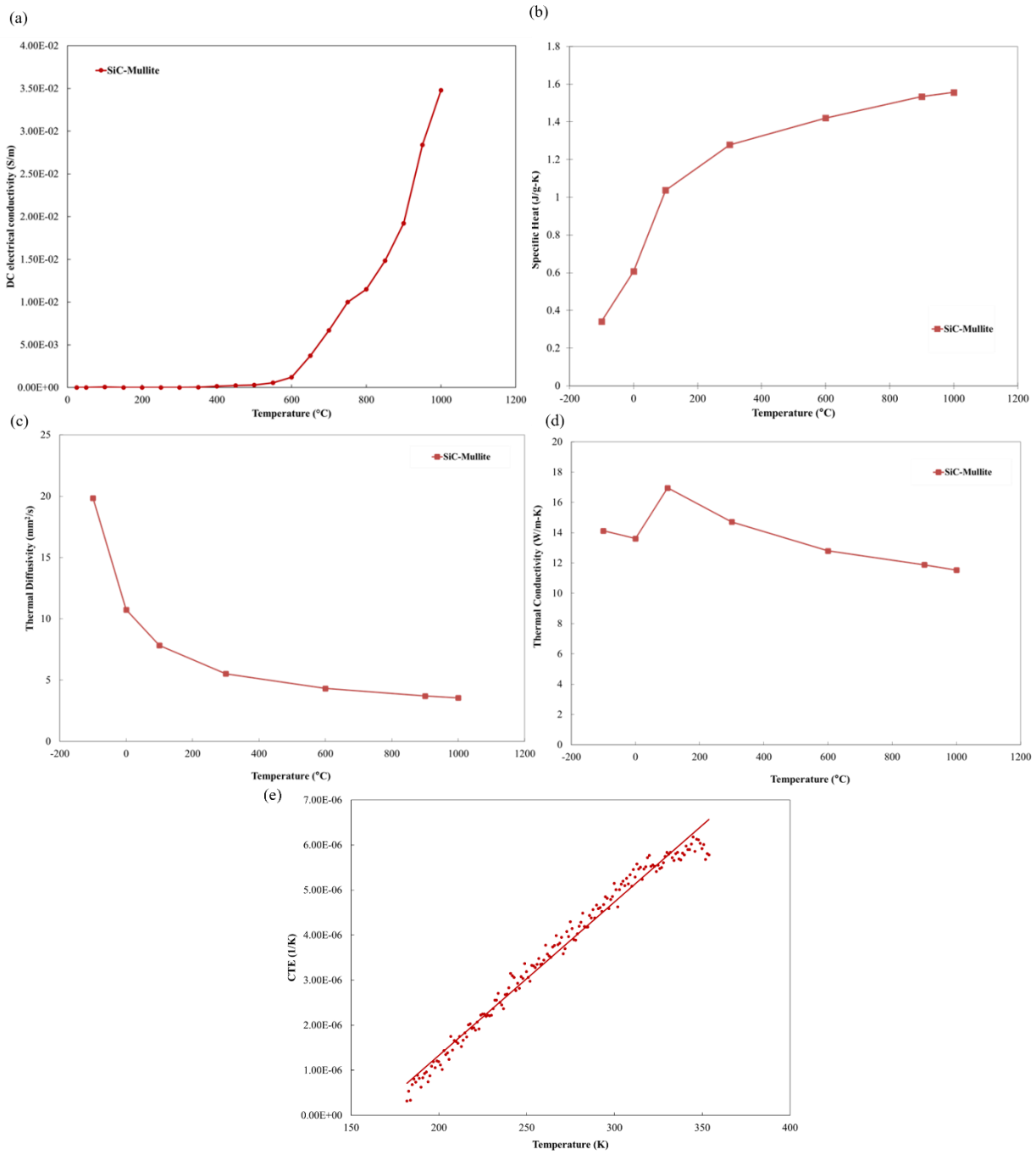

Figure 47: (a) Variation in the electrical conductivity of the SiC-mullite composite at different temperatures. Temperature-dependent trends for (b) specific heat capacity, (c) thermal diffusivity, (d) thermal conductivity, and (e) coefficient of thermal expansion (CTE) of the SiC-mullite composite [191].

The specific heat capacity of the SiC-mullite composite, as depicted in Figure 47b, exhibited a continuous increase from 0.341 to 1.56 $J.(g.K)^{-1}$ as the temperature rose from -100 °C to 1000 °C. Conversely, thermal diffusivity (Figure 47c) demonstrated a decrease from 19.8 to

3.55 mm^2/s within the same temperature range. Initial heating from -100 °C to 100 °C led to an increase in thermal conductivity (Figure 47d) from 14.1 to 17 $W.(m.K)^{-1}$, followed by a continuous decrease to 11.5 $W.(m.K)^{-1}$ as the temperature reached 1000 °C.

The thermal expansion coefficient (α) of SiC-mullite composite was determined using Eq. (29)

$$\alpha = \frac{\Delta L / L_0}{\Delta T} \tag{29}$$

Here, ΔL is the difference in length, L_0 is the initial length, and ΔT is the difference in temperature. The thermal expansion co-efficient, presented in Figure 47e, exhibited a linear increase from 3.17 x 10^{-7}/K to 5.615 x 10^{-6} /K as the SiC-mullite sample was heated from 182 K to 354 K.

6.3 Discussions

The study findings reveal that the in-situ mineralization of mullite has yielded a dense SiC-mullite composite characterized by high thermomechanical properties. The incorporation of 15 wt% coal ash with an Al_2O_3/SiO_2 ratio of 8.5 to 85 wt% SiC led to the formation of a SiC-mullite composite containing 11.4 wt % mullite phase with an Al_2O_3/SiO_2 ratio of 1.5 after thermal treatment at 1400 °C for 1h. The SiO_2 required for the mullite phase formation was provided by the oxidation product of SiC during thermal treatment. The use of a high thermal treatment temperature induced a liquid phase sintering mechanism, filling the interspaces between SiC particles with the mullite phase. Evidence from Energy Dispersive X-ray (EDX) analysis indicates Al ion diffusion into the silicon oxide layer during heat treatment resulted in a strong interfacial bond. This bond significantly enhanced the thermal conductivity and mechanical properties of the material: a thermal conductivity of 17 W/m.K at 100 °C, a

compression strength of 434 ± 20 MPa, a nano indentation modulus of elasticity of 370.9 ± 22.6 GPa, and Vicker's hardness of 11.5 ± 1.2 GPa. Thermal shock resistance tests demonstrated minimal changes in dimensions, emphasizing the material's high stability in terms of mechanical strength. The superior thermomechanical stability of the SiC-mullite composite can be attributed to the low and comparable thermal expansion coefficients, coupled with the high stiffness of the composite components. Enhanced thermal and electrical conductivity arise from the transition of entrapped iron ions from the hematite phase in coal ash within the interstitial space of the mullite and cristobalite solid solutions. The observed increase in electrical conductivity with temperature is linked to increased vacancies facilitating atomic mobility of oxygen and minor cations. Taken all together, the SiC-mullite preparation method outlined in this study has resulted in a material with promising engineering applications, including use as semiconductors, gas filters, diesel motor parts, gas turbines, industrial heat exchangers, fusion reactor components, and high-temperature energy exchanger systems.

The investigation employed SEM-EDX and XRD techniques to scrutinize the structural characteristics and phase composition of the SiC composite following diverse thermal treatments and mechanical assessments. XRD analysis (Figure 35a) of coal fly ash it was found that the 15 wt% ash powder used in this work is composed of 6.8 ± 0.6 wt % α-Al_2O_3 and 6.3 ± 0.1 wt % quartz (SiO_2), 0.8 ± 0.1 wt % mullite ($3Al_2O_3.2SiO_2$), and 1.1 ± 0.04 wt % haematite (Fe_2O_3). After sintering of the 85% SiC-15% coal ash at 1400 °C/1hr, XRD analysis showed the phase composition SiC and mullite with complete absence of α-Al_2O_3 (Figure 35b). Considering the coal ash's low SiO_2 content (8.6), which is insufficient to transform the α-Al_2O_3 present in the coal ash into mullite, it is anticipated that the majority of the SiO_2 oxidation product of SiC is responsible for formation of mullite as per equation (30),

$$3Al_2O_3 + 2SiO_2 \rightarrow 3Al_2O_3.2SiO_2 \quad (30)$$

This is further supported by a 3.2 wt% reduction in the concentration of the SiC component in the SiC-mullite composite. The XRD analysis revealed a shift in the d-spacing of the (210) plane of mullite and the (101) plane of cristobalite phases, indicating the formation of a solid solution, likely due to the diffusion of $Fe^{3+/2+}$ ions into the two phases during thermal treatment. Indeed, the XRD analysis of the SiC-mullite composite did not exhibit any signals of haematite (Fe_2O_3) present in the coal fly ash. Literature data indicates that mullite typically melts at approximately 1880 °C under metastable conditions [199]. However, in our study, the in-situ formation of mullite and its subsequent melting occurred at a lower temperature (1400 °C). The reduced formation temperature of mullite is attributed to $Fe^{3+/2+}$ ions completely entering the mullite structure through solid solution formation. Several studies have reported that iron can dissolve into the mullite structure [200-202]. These investigations suggest that iron, specifically the Fe^{3+} cation with an ionic radius of 0.0065 nm, is larger compared to the Al^{3+} cation with an ionic radius of 0.0054 nm. At high temperatures, these Fe^{3+} ions are inclined to occupy the AlO_6 octahedral sites within mullite, forming a stable solid solution [202].

SEM-EDX analysis (Figure 36) of the fracture surface illustrates the fusion of SiC particles by the mullite phase. Elemental analysis using EDX (Figure 37) revealed an Al concentration gradient at the mullite-SiC interface. This gradient is attributed to the diffusion of Al^{3+} ion into the SiO_2 oxidation product on SiC surface (Figure 38). The liquid phase sintering mechanism, at 1400 °C, reduced the diffusion distance, facilitating the in-situ formation of mullite. Mullite structures are known to accommodate a wide range of SiO_2/ Al_2O_3 ratios [182]. Consequently, the gradual variation in Al concentration at the interface promotes a functionally graded SiC-mullite composite, wherein the mechanical and thermal properties vary gradually

across the bonding zone between components. Moreover, under the application of mechanical stresses, the smooth transduction of the mechanical signal across the interface between SiC and mullite minimizes stress concentration at the grain boundaries. Therefore, the creation of a functionally graded SiC-mullite is responsible for retaining the high thermal and mechanical stability of the composite after thermal shock.

Mechanical tests revealed that the compressive strength of the SiC-mullite composite is influenced by several key parameters: (i) thermal treatment temperature (1300-1500 °C), (ii) SiC/coal fly ash weight ratio, and (iii) coal fly ash particle size as shown in Figure 39(a-d). Literature data indicate that the optimal formation and densification of the mullite phase occur in the temperature range of 1400-1600 °C [171, 181-183]. The notable increase in strength ($p < 0.004$) for samples treated at 1400 °C compared to those treated at 1300 °C can be attributed to the enhanced mineralization of the mullite phase, which facilitates bonding between SiC particles. The relatively lower mechanical strength of samples treated at 1500 °C compared to those treated at 1400 °C may be attributed to increased cristobalite formation, which has lower mechanical strength than SiC and mullite, and partial melting of the silica. As the percentage of coal ash increased from 10 to 15%, the compressive strength increased from 223 ± 16 MPa to 267 ± 20 MPa. This significant strength increase is attributed to the higher percentage of mullite in the composite, as coal ash serves as a source of Al_2O_3. However, as the coal fly ash percentage increased to 20% or 25 wt%, the compressive strength of the composite decreased. Since SiC is the strongest phase present in the SiC-mullite composite, the decrease in its concentration is responsible for the decline in compressive strength. A similar decrease in SiC composite strength was observed in another study when the wt% of SiC fell below 85% [203]. The compressive strength of the SiC-mullite composite nearly doubled when the coal ash particle size was reduced

below 38 µm. The enhanced mechanical strength is attributed to the increased intergranular contact surface area between particles, which efficiently expedited the mullitization reaction, enhanced liquid phase formation, and reduced porosity. This aligns with literature data showing that decreasing the particle size of coal fly ash to 58 µm enhances the formation of the mullite phase compared to coarser fly ash [197]. The compressive strength of the SiC-mullite composite increased from 431 ± 21 MPa to 437 ± 15 MPa when the dwelling time was increased from 15 mins to 45 mins; however, the strength of the composites decreased to 434 ± 20 MPa as the dwelling time increased to 1 hr. Although the changes in compressive strength are not statistically significant due to the homogeneity of the sintering process, an optimal dwelling time of 1 hr at 1400 °C was selected. Therefore, the SiC-mullite composite, prepared by mixing at a ratio of 85 wt% SiC/15 wt% coal fly ash of particle size < 38 µm, pressed at 250 MPa/30 mins, and treated at 1400 °C/1 hr, exhibited a compressive strength of 434 ± 20 MPa, a nanoindentation modulus of elasticity of 370.9 ± 22.6 GPa, and Vickers hardness of 11.5 ± 1.2 GPa. Fracture surface morphology revealed crack deflection and crack branching in the mullite phase, indicative of a strong interfacial bonding zone. The interaction between cracks and pores was also observed, wherein a crack may be arrested or deflected due to the presence of micropores. This is advantageous for relieving stress concentration and achieving higher mechanical performance. The apparent density of the composite was found to be 2.36 $g.cm^{-3}$, while the theoretical density was calculated to be 2.98 $g.cm^{-3}$. Hence, the apparent density is approximately 79% of the theoretical density. SEM image analysis showed 8.2 ± 1.7% porosity, and apparent open porosity using Archimedes' principle was found to be 3%. The low porosity of the SiC-mullite composite is attributed to the mullite liquid-phase sintering mechanism, which filled the interspace among the SiC particles.

The exceptional thermal shock resistance observed in our SiC-mullite composite can be attributed to several key factors: (i) low and comparable coefficients of thermal expansion (CTE) values for the constituent phases, (ii) a strong interphase bond, (iii) compositional stability at high temperatures, and (iv) low porosity. The composite retained both its mechanical strength and dimensions after rapid quenching from 1400 °C to -196 °C in liquid nitrogen (Figure 43). The CTE of mullite (5.3×10^{-6} /K at 273-1273 K) is comparable to that of SiC (4.7×10^{-6} /K at 293-973 K), facilitating uniform expansion and contraction during heating and quenching, respectively. This similarity reduces interfacial shear stress between the two phases, as evidenced by the prevalence of a transgranular fracture mechanism (Figure 42). Analysis of the fracture surface through FTIR (Figure 45 and Figure 46) revealed distinctive bands corresponding to Si-O-Si, Si-O, Si-C, Al-O, and Si-O-Al, representing the three phases within the composite and providing strong evidence of transgranular fracture. The CTE of pure cristobalite is 17.5×10^{-6} /K at 273-1273 K, but the diffusion of Al ions is recognized for increasing density and reducing the CTE of silica [204]. Moreover, XRD analysis (Figure 44a) of the SiC-mullite composite reveals a 6.8 ± 0.2 phase % β cristobalite. The minimal presence of cristobalite in the composite, coupled with Al diffusion, mitigates the impact of cristobalite on the final CTE. The overall CTE value for the SiC-mullite composite was found to be relatively low (3.17×10^{-7} /K at 182 K and 5.615×10^{-6} /K at 354 K). Although XRD analysis (Figure 44b) indicates 1% decrease in the SiC phase after quenching, this minimal reduction does not any affect the mechanical strength of the composite, as demonstrated in (Figure 43). Previous research, as documented in the literature, has reported a substantial reduction, close to 30%, in the weight percentage of the SiC phase after sintering a mixture comprising SiC, $Al(OH)_3$, Y_2O_3, and CaF_2 to in situ form mullite-bonded porous SiC at 1550 °C for 4 hours [186] This notable decrease in SiC weight is primarily

attributed to the oxidation of carbon, resulting in its release as CO or CO_2. Concomitant with the 30% SiC loss, there was a formation of a 30.5 wt% mullite phase [186]. While no cristobalite phase was observed in that study, there was a substantial 75% reduction in the strength and thermal stability of the composite after undergoing thermal shock from 800 °C to 20 °C. A similar decline of 70% in flexural strength was noted after quenching mullite-bonded porous SiC ceramics containing 3.0 wt% Y_2O_3 from 1200 °C to 20 °C in water [185]. The compromise in mechanical strength is attributed to the formation of microcracks induced by thermal stresses at the interface between phases. The extensive formation of microcracks, coupled with an increase in crack length as the temperature difference escalates during the thermal shock test, compromised the residual strength of the material. Additionally, the introduction of Y_2O_3 led to the formation of a glass phase, facilitating the debonding of phases within the composite. Han et al employed a composition consisting of 4 wt % mullite fibers, 79 wt % SiC, 15 wt % activated carbon, and 2 % zirconia, which was sintered in air at 1450 °C for 4 hr to produce mullite fiber-reinforced SiC porous ceramics [187]. Zirconia served as a sintering aid, facilitating a reduction in the heat treatment temperature. During the process, mullite fibers reacted with the cristobalite phase present on the SiC surface through oxidation, transforming into acicular mullite crystals within the neck of the pore. The formation of acicular mullite required elevated temperatures and an extended duration, resulting in excessive oxidation of SiC particles and promoting the generation of microcracks in the composite due to the high concentration of cristobalite. Consequently, a substantial decrease in bending strength was observed when the ceramics were rapidly cooled in water from 800 °C [187]. Additionally, it has been reported that thermally oxidized bonded porous SiC ceramics exhibited a similar decrease in mechanical strength upon quenching [12, 164]. The thermomechanical stability exhibited by the mullite-bonded SiC in our

study surpasses that of other SiC composites, including those formulated with SiC-ZrB_2-HfB_2 and SiC-$ZrBr_2$ or SiC-carbon nanotube CNT) [205, 206].

Analysis of crystal size using X-ray diffraction (XRD) spectra revealed an increase in the size of SiC crystallites from 413 to 539 Å after quenching (Table 6). This increase in SiC crystallite size can be attributed to induced crystal growth during the recrystallization process, which occurred when the discs were reheated at 1400 °C for 15 minutes before quenching. The recrystallization mechanism is believed to transpire through the diffusion of carbon atoms into the silicon decomposed from SiC at high temperatures. Indeed, a reduction in the percentage of the SiC phase from 84.1% to 80.7% was observed after quenching. This decline in the SiC percentage was accompanied by an elevation in the silica phase from 4.5% to 7.5%, attributed to SiC oxidation. The silica layer forming on the surface of SiC particles is rich in Si and deficient in oxygen [62, 63]. These findings indicate that the recrystallization process occurs through the diffusion of released carbon into the oxygen-deficient silica phase at the interface with the SiC particle, leading to the growth of SiC crystals. This is supported by the absence of a carbon characteristic signal in the XRD spectrum. A comparable increase in SiC crystallite size, from 16 Å to 1500 Å at 1400 °C, was documented in the synthesis of SiC powder from organosilane [207]. The observed augmentation in SiC crystallite size aligns well with the enlargement of disc dimensions, evidenced by a 20 µm increase in disc diameter after thermal shock. Conversely, the reduction in the crystallite size of cristobalite results from the transformation of β to α cristobalite. Other studies have similarly noted a decrease in crystallite size during the phase transformation of quartz to cristobalite, from 67.27 nm to 41.47 nm at 1200 °C [208].

The electrical conductivity of the SiC-mullite composite in our study is governed by the proportion and distribution of semiconductive SiC and dielectric mullite phases, in addition to

the presence of iron ions in the interstitial space. As the temperature increases, the electric conductivity of the SiC-mullite composite also increases. Below 400 ℃, the relatively low electrical conductivity is attributed to the poor conductive nature of both SiC and mullite phases (Figure 47a). During this temperature range, the ceramic's low conductivity is linked to the sluggish phonon transition [209]. The electrical conductivity of the SiC-mullite composite exhibits a notable increase from 1.38 x 10^{-4} at 400 ℃ to 3.48 x 10^{-2} Sm^{-1} at 1000 ℃. Malki et al. have documented a distinction in the electrical conductivity of single crystal mullite, noting a low-temperature range (LTR) of conductivity up to to 900°C (average conductivity ≈ 5.4910 38 x 10^{-7} Sm^{-1} at 550 ℃) and a high-temperature range (HTR) above ≈ 900°C (average conductivity ≈ 1.2 x 10^{-3} Sm^{-1} at 1400°C) [210]. At elevated temperatures, the rise in mullite's electrical conductivity is attributed to the hopping of oxygen atoms. This process involves linking the tetrahedra of the tetrahedral double chains in the aluminosilicates towards adjacent oxygen vacancies, accompanied by associated structural rearrangements [210]. The overall increase in electrical conductivity can be attributed to several factors. Initially, the transition of entrapped iron ions within the interstitial space of the mullite and cristobalite solid solution plays a role. Subsequently, the thermal excitation of a substantial number of electrons at higher temperatures leads to their transition from the Fermi to the conduction levels in the SiC phase. Additionally, the hopping of oxygen atoms in the mullite phase towards oxygen vacancies contributes to the heightened electrical conductivity at elevated temperatures.

The observed decline in thermal diffusivity in the SiC-mullite composite with increasing temperature is fundamentally linked to the rise in phonon frequency or phonon vibration amplitude. This increase in phonon amplitude is directly associated with the elevation of specific heat, consequently leading to a reduction in thermal diffusivity [211]. The thermal conductivity

of the SiC-mullite composite (Figure 47d) exhibited a continuous decrease from 17 to 11.5 $W.(m.K)^{-1}$ as the temperature rose to 1000 °C. This decline in thermal conductivity at elevated temperatures is attributed to the heightened amplitude of thermal vibration, which, in turn, increases the collision frequency of phonons, resulting in a constrained phonon mean free path length [212]. The thermal conductivity of the SiC-mullite composite prepared in our study (17 W/m.K at 100 °C) surpasses that reported for other materials, such as 4.8 $W.(m.K)^{-1}$ for SiC-mullite-Al_2O_3 composite [213] and 9.62 $W.(m.K)^{-1}$ for SiC-mullite composite composed of 68 wt% SiC (61 µm), 17 wt% SiC (20 µm), 8.49 wt% $Al(OH)_3$ and 6.51 wt% Suzhou kaolin [203]. These studies have linked the decrease in thermal conductivity to the porosity (24.64% - 29.26%) present in these composites, contributing to an increase in interface resistance. The presence of pores in the samples is likely to result in fewer phonon mean free paths, causing increased thermal energy loss during transmission and, consequently, a reduction in thermal conductivity. In contrast, the high thermal conductivity observed in our SiC-mullite composite can be attributed to the low porosity (8.2 ± 1.7%) achieved through liquid phase sintering, limiting phonon scattering and leading to an increased phonon mean free path length. Parchovianský observed a substantial 76% decline in thermal conductivity during the heating of composites consisting of 80 wt% Al_2O_3-20 wt% SiC composites from 0 to 1000 °C. This reduction was attributed to the development of internal stresses between the alumina matrix and SiC, arising from a thermal expansion coefficient mismatch [214]. In our study, the comparable thermal expansion coefficients between SiC and mullite, along with a concentration gradient of Al ions in the bonding zone, effectively modulated the transition of thermal conductivity and enhanced high thermal stability. This synergistic effect is responsible for the relatively low (32%) decrease in thermal conductivity observed at 1000 °C in our SiC-mullite composite.

CHAPTER 7: CONCLUSION

7.1 Conclusion

In this work, a SiC-mullite thermal material was synthesized through the innovative technique of in situ mullite liquid phase sintering, utilizing coal fly ash as an alumina source. The strong interfacial bond between SiC and mullite, coupled with the composite's notable mechanical strength, dimensional stability, and resistance to thermal shock, can be attributed to the reaction between alumina in the coal fly ash and the silica layer forming on SiC during sintering. The gradual variation in Al concentration at the interface further contributes to these enhanced properties. The relatively lower formation temperature and in situ melting of mullite are facilitated by the presence of minor metal oxides, particularly haematite, in the coal fly ash. The incorporation of haematite into the mullite structure forms a solid solution, thereby improving electrical properties and thermal conductivity. The composite's low porosity (8.2%) and the similar thermal expansion coefficients of SiC and mullite phases collectively contribute to its high thermal conductivity. In conclusion, the mullite-bonded SiC composite exhibits promising potential for diverse high-temperature applications, including semiconductors, gas filters, diesel engine components, gas turbines, industrial heat exchangers, fusion reactor parts, and high-temperature energy exchanger systems. This work demonstrated that instead of silica layer, in situ mullite bonding agent can be utilized in additive manufacturing of SiC in the powder bed binder jet for achieving a dense SiC parts with high thermomechanical properties.

7.2 Future work

This work successfully demonstrated the possibility of utilizing an in-situ mullite bonding agent, rather than a silica layer, in the additive manufacturing of SiC through the powder bed binder jet process, in order to form dense SiC parts with superior thermomechanical

properties. As illustrated in Appendix B, the mullite bonding phase, which fuses the SiC particles together, exhibited significantly higher compressive strength compared to the cristobalite phase formed from the silica layer. Therefore, future work should focus on incorporating SiC-mullite into the feedstock within a powder bed binder jet system. This strategic inclusion can minimize voids between SiC particles, creating a strong bonding zone predominantly composed of mullite. The objective will be to facilitate the fusion of SiC particles, thereby enhancing the densification and thermomechanical properties of the printed parts.

REFERENCES

1. Saddow, S.E. and A.K. Agarwal, Advances in silicon carbide processing and applications. 2004: Artech House.

2. Harris, G.L., Properties of silicon carbide. 1995: Iet.

3. Somiya, S. and Y. Inomata, Silicon carbide ceramics. 1. Fundamental and solid reaction. Vol. 13. 1991: Springer.

4. Liu, G., et al., Recent advances in joining of SiC-based materials (monolithic SiC and SiC f/SiC composites): Joining processes, joint strength, and interfacial behavior. Journal of Advanced Ceramics, 2019. 8: p. 19-38.

5. Chen, X., et al., Residual stress variation in SiC f/SiC composite during heat treatment and its effects on mechanical behavior. Journal of Advanced Ceramics, 2020. 9: p. 567-575.

6. Liu, J., et al., Fabrication, microstructure, and properties of SiC/Al 4 SiC 4 multiphase ceramics via an in-situ formed liquid phase sintering. Journal of Advanced Ceramics, 2020. 9: p. 193-203.

7. Eom, J.-H., Y.-W. Kim, and S. Raju, Processing and properties of macroporous silicon carbide ceramics: A review. Journal of Asian Ceramic Societies, 2013. 1(3): p. 220-242.

8. She, J., et al., Oxidation bonding of porous silicon carbide ceramics. Journal of materials science, 2002. 37: p. 3615-3622.

9. Green, D.J. and P. Colombo, Cellular ceramics: intriguing structures, novel properties, and innovative applications. MRS bulletin, 2003. 28(4): p. 296-300.

10. Greil, P., Advanced engineering ceramics. Advanced Engineering Materials, 2002. 4(5): p. 247-254.

11. Rojas, P., G. Piderit, and P. Toro, Development of open-pore silicon carbide foams. Key engineering materials, 1997: p. 1731-1734.

12. Ding, S., Y.-P. Zeng, and D. Jiang, Thermal shock resistance of in situ reaction bonded porous silicon carbide ceramics. Materials Science and Engineering: A, 2006. 425(1-2): p. 326-329.

13. Kotani, M., A. Kohyama, and Y. Katoh, Development of SiC/SiC composites by PIP in combination with RS. Journal of nuclear materials, 2001. 289(1-2): p. 37-41.

14. Nastic, A., et al., Instrumented and Vickers indentation for the characterization of stiffness, hardness and toughness of zirconia toughened Al2O3 and SiC armor. Journal of Materials Science & Technology, 2015. 31(8): p. 773-783.

15. Shen, Z., et al., Ballistic reliability study on SiC/UHMWPE composite armor against armor-piercing bullet. Composite Structures, 2019. 213: p. 209-219.

16. Übeyli, M., et al., The ballistic performance of SiC–AA7075 functionally graded composite produced by powder metallurgy. Materials & Design (1980-2015), 2014. 56: p. 31-36.

17. Yin, J., et al., The effects of SiC precursors on the microstructures and mechanical properties of SiCf/SiC composites prepared via polymer impregnation and pyrolysis process. Ceramics International, 2015. 41(3): p. 4145-4153.

18. Dong, S., Y. Katoh, and A. Kohyama, Preparation of SiC/SiC composites by hot pressing, using Tyranno-SA fiber as reinforcement. Journal of the American Ceramic Society, 2003. 86(1): p. 26-32.

19. Kotani, M., et al. Fabrication of high performance SiC/SiC composite by polymer impregnation and pyrolysis method. in 23rd Annual Conference on Composites, Advanced Ceramics, Materials, and Structures: B: Ceramic Engineering and Science Proceedings. 1999. Wiley Online Library.

20. Wilhelm, M., M. Kornfeld, and W. Wruss, Development of SiC–Si composites with fine-grained SiC microstructures. Journal of the European Ceramic Society, 1999. 19(12): p. 2155-2163.

21. Alhosseini, S.H.N. and S.R. Mousavi, The effect of oxide, carbide, nitride and boride additives on properties of pressureless sintered SiC: A review. Journal of the European Ceramic Society, 2019. 39(7): p. 2215-2231.

22. Wu, C., et al., High-speed grinding of HIP-SiC ceramics on transformation of microscopic features. The International Journal of Advanced Manufacturing Technology, 2019. 102: p. 1913-1921.

23. Lewis, J.A., Colloidal processing of ceramics. Journal of the American Ceramic Society, 2000. 83(10): p. 2341-2359.

24. Larker, H.T. and R. Lundberg, Near net shape production of monolithic and composite high temperature ceramics by hot isostatic pressing (HIP). Journal of the European Ceramic Society, 1999. 19(13-14): p. 2367-2373.

25. Edirisinghe, M. and J. Evans, Fabrication of engineering ceramics by injection moulding. II. Techniques. International journal of high technology ceramics, 1986. 2(4): p. 249-278.

26. Greil, P., Near net shape manufacturing of polymer derived ceramics. Journal of the European Ceramic Society, 1998. 18(13): p. 1905-1914.

27. Klocke, F., Modern approaches for the production of ceramic components. Journal of the European Ceramic Society, 1997. 17(2-3): p. 457-465.

28. Polozov, I., et al., Fabrication of silicon carbide fiber-reinforced silicon carbide matrix composites using binder jetting additive manufacturing from irregularly-shaped and spherical powders. Materials, 2020. 13(7): p. 1766.

29. DebRoy, T., et al., Additive manufacturing of metallic components–process, structure and properties. Progress in Materials Science, 2018. 92: p. 112-224.

30. de Hazan, Y. and D. Penner, SiC and SiOC ceramic articles produced by stereolithography of acrylate modified polycarbosilane systems. Journal of the European Ceramic Society, 2017. 37(16): p. 5205-5212.

31. Chen, H., et al., 3D printing of SiC ceramic: Direct ink writing with a solution of preceramic polymers. Journal of the European Ceramic Society, 2018. 38(16): p. 5294-5300.

32. Park, S., et al., Fabrication of three-dimensional SiC ceramic microstructures with near-zero shrinkage via dual crosslinking induced stereolithography. Chemical communications, 2009(32): p. 4880-4882.

33. He, R., et al., Fabrication of SiC ceramic architectures using stereolithography combined with precursor infiltration and pyrolysis. Ceramics International, 2019. 45(11): p. 14006-14014.

34. Gómez-Gómez, A., et al., Highly-porous hierarchical SiC structures obtained by filament printing and partial sintering. Journal of the European Ceramic Society, 2019. 39(4): p. 688-695.

35. Tu, T. and G. Jiang, SiC reticulated porous ceramics by 3D printing, gelcasting and liquid drying. Ceramics International, 2018. 44(3): p. 3400-3405.

36. Zocca, A., et al., Additive manufacturing of SiSiC by layerwise slurry deposition and binder jetting (LSD-print). Journal of the European Ceramic Society, 2019. 39(13): p. 3527-3533.

37. Zhu, Q., et al., High strength aligned SiC nanowire reinforced SiC porous ceramics fabricated by 3D printing and chemical vapor infiltration. Ceramics International, 2020. 46(5): p. 6978-6983.

38. Weisensel, L., et al., Laminated object manufacturing (LOM) of SiSiC composites. Advanced Engineering Materials, 2004. 6(11): p. 899-903.

39. Liu, K., et al., Laser additive manufacturing and homogeneous densification of complicated shape SiC ceramic parts. Ceramics International, 2018. 44(17): p. 21067-21075.

40. Zhang, S., R. Tu, and T. Goto, High-speed epitaxial growth of β-SiC film on Si (111) single crystal by laser chemical vapor deposition. Journal of the American Ceramic Society, 2012. 95(9): p. 2782-2784.

41. Chen, Z., et al., 3D printing of ceramics: A review. Journal of the European Ceramic Society, 2019. 39(4): p. 661-687.

42. Sachs, E.M., et al., Three-dimensional printing techniques. 1993, Google Patents.

43. Withell, A., et al. Porous ceramic filters through 3D printing. in Innovative Developments in Virtual and Physical Prototyping: Proceedings of the 5th International Conference on Advanced Research in Virtual and Rapid Prototyping, Leiria, Portugal. 2011.

44. Diegel, O., et al., Low-Cost 3D Printing of Controlled Porosity Ceramic Parts. Int. J. Autom. Technol., 2012. 6(5): p. 618-626.

45. Enneti, R.K., et al., Sintering of WC-12% Co processed by binder jet 3D printing (BJ3DP) technology. International Journal of Refractory Metals and Hard Materials, 2018. 71: p. 28-35.

46. Watters, M.P. and M.L. Bernhardt, Modified curing protocol for improved strength of binder-jetted 3D parts. Rapid Prototyping Journal, 2017. 23(6): p. 1195-1201.

47. Nandwana, P., et al., Powder bed binder jet 3D printing of Inconel 718: Densification, microstructural evolution and challenges☆. Current Opinion in Solid State and Materials Science, 2017. 21(4): p. 207-218.

48. Garzón, E.O., J.L. Alves, and R.J. Neto, Post-process influence of infiltration on binder jetting technology. Materials design and applications, 2017: p. 233-255.

49. Mostafaei, A., et al., Binder jet 3D printing—Process parameters, materials, properties, modeling, and challenges. Progress in Materials Science, 2021. 119: p. 100707.

50. Du, W., et al. Binder jetting additive manufacturing of ceramics: A literature review. in ASME International Mechanical Engineering Congress and Exposition. 2017. American Society of Mechanical Engineers.

51. Cesaretti, G., et al., Building components for an outpost on the Lunar soil by means of a novel 3D printing technology. Acta Astronautica, 2014. 93: p. 430-450.

52. Yu, T., Z. Zhao, and J. Li, Effect of sintering temperature and sintering additives on the properties of alumina ceramics fabricated by binder jetting. Ceramics International, 2023. 49(6): p. 9948-9955.

53. Tang, Y., et al., Elastic modulus of 316 stainless steel lattice structure fabricated via binder jetting process. Materials Science and Technology, 2016. 32(7): p. 648-656.

54. Rabinskiy, L., et al. Fabrication of porous silicon nitride ceramics using binder jetting technology. in IOP Conference Series: Materials Science and Engineering. 2016. IOP Publishing.

55. Gonzalez, J., et al., Characterization of ceramic components fabricated using binder jetting additive manufacturing technology. Ceramics International, 2016. 42(9): p. 10559-10564.

56. Fielding, G.A., A. Bandyopadhyay, and S. Bose, Effects of silica and zinc oxide doping on mechanical and biological properties of 3D printed tricalcium phosphate tissue engineering scaffolds. Dental materials, 2012. 28(2): p. 113-122.

57. Melcher, R., et al., Fabrication of Al2O3-based composites by indirect 3D-printing. Materials Letters, 2006. 60(4): p. 572-575.

58. Lv, X., et al., Fabrication of SiC whisker-reinforced SiC ceramic matrix composites based on 3D printing and chemical vapor infiltration technology. Journal of the European Ceramic Society, 2019. 39(11): p. 3380-3386.

59. Baux, A., et al., Synthesis and properties of macroporous SiC ceramics synthesized by 3D printing and chemical vapor infiltration/deposition. Journal of the European Ceramic Society, 2020. 40(8): p. 2834-2854.

60. Fleisher, A., et al., Reaction bonding of silicon carbides by Binder Jet 3D-Printing, phenolic resin binder impregnation and capillary liquid silicon infiltration. Ceramics International, 2019. 45(14): p. 18023-18029.

61. Fu, Z., et al., Three-dimensional printing of SiSiC lattice truss structures. Materials Science and Engineering: A, 2013. 560: p. 851-856.

62. El-Ghannam, A., S. Chandrasekaran, and F. Sultana, Synthesis and characterization of a novel silica nanowire-reinforced SiC thermal material. Journal of Solid State Chemistry, 2021. 297: p. 122055.

63. El-Ghannam, A., S. Chandrasekaran, and F. Sultana, Mechanism of epitaxial growth of silica nanowires reinforcing agent in porous SiC scaffold. Procedia Manufacturing, 2021. 53: p. 535-560.

64. Beasock, D., et al., Effect of processing parameters on the microstructure and mechanical behavior of a silicon carbide-silica composite. Procedia Manufacturing, 2019. 34: p. 747-753.

65. Rao, C., et al., Inorganic nanowires. Progress in Solid State Chemistry, 2003. 31(1-2): p. 5-147.

66. Xia, Y., et al., One-dimensional nanostructures: synthesis, characterization, and applications. Advanced materials, 2003. 15(5): p. 353-389.

67. Rao, C., A. Govindaraj, and S. Vivekchand, Inorganic nanomaterials: current status and future prospects. Annual Reports Section" A"(Inorganic Chemistry), 2006. 102: p. 20-45.

68. Neubauer, E., et al., Potential and challenges of metal-matrix-composites reinforced with carbon nanofibers and carbon nanotubes. Composites Science and Technology, 2010. 70(16): p. 2228-2236.

69. Marshall, D.B. and A.G. Evans, Failure mechanisms in ceramic-fiber/ceramic-matrix composites. Journal of the American Ceramic Society, 1985. 68(5): p. 225-231.

70. Becher, P.F., et al., Toughening behavior in whisker-reinforced ceramic matrix composites. Journal of the American Ceramic Society, 1988. 71(12): p. 1050-1061.

71. Vedrtnam, A. and S.P. Sharma, Study on the performance of different nano-species used for surface modification of carbon fiber for interface strengthening. Composites Part A: Applied Science and Manufacturing, 2019. 125: p. 105509.

72. Schneck, T.K., et al., Carbon fiber surface modification for tailored fiber-matrix adhesion in the manufacture of C/C-SiC composites. Composites Part A: Applied Science and Manufacturing, 2019. 120: p. 64-72.

73. Wang, Z., et al., Effects of surface treatment of carbon fiber: Tensile property, surface characteristics, and bonding to epoxy. Polymer Composites, 2016. 37(10): p. 2921-2932.

74. Zhang, X., et al., Microstructure and synergistic-strengthening efficiency of CNTs-SiCp dual-nano reinforcements in aluminum matrix composites. Composites Part A: Applied Science and Manufacturing, 2018. 105: p. 87-96.

75. He, F., et al., Carbon fiber/SiC composites modified SiC nanowires with improved strength and toughness. Materials Science and Engineering: A, 2018. 734: p. 374-384.

76. Wang, H.-f., et al., Preparation and strength of SiC refractories with in situ β-SiC whiskers as bonding phase. Ceramics International, 2016. 42(1): p. 727-733.

77. Li, J., et al., Fabrication and characterization of carbon-bonded carbon fiber composites with in-situ grown SiC nanowires. Carbon, 2017. 118: p. 148-155.

78. Fu, Q., et al., Effects of thermal shock on the microstructures, mechanical and thermophysical properties of SiCnws-C/C composites. Composites Part B: Engineering, 2019. 164: p. 620-628.

79. Rahman, A.S., M.E. Hossain, and D.W. Radford, Synergistic effects of processing and nanofiber reinforcement on the mechanical and ferroelectric performance of geopolymer matrix composites. Journal of materials research and technology, 2018. 7(1): p. 45-54.

80. Cano-Crespo, R., et al., Carbon nanofibers replacing graphene oxide in ceramic composites as a reinforcing-phase: Is it feasible? Journal of the European Ceramic Society, 2017. 37(12): p. 3791-3796.

81. Cano-Crespo, R., et al., Graphene or carbon nanofiber-reinforced zirconia composites: Are they really worthwhile for structural applications? Journal of the European Ceramic Society, 2018. 38(11): p. 3994-4002.

82. Qu, L., et al., Design of a ductile carbon nanofiber/ZrB2 nanohybrid film with entanglement structure fabricated by electrostatic spinning. Ceramics International, 2021. 47(11): p. 15114-15120.

83. Tian, J., et al., Mechanical and thermal-insulating performance of silica aerogel enhanced jointly with glass fiber and fumed silica by a facile compressing technique. Chemical Physics Letters, 2020. 739: p. 136950.

84. He, J., et al., Transparent ultrathin SiO2 nanowire aerogel displaying novel properties when interacting with water: A promising versatile functional platform. Fundamental Research, 2023. 3(1): p. 118-125.

85. Pan, Z., et al., Temperature dependence of morphologies of aligned silicon oxide nanowire assemblies catalyzed by molten gallium. Nano Letters, 2003. 3(9): p. 1279-1284.

86. Yu, D., et al., Amorphous silica nanowires: intensive blue light emitters. Applied Physics Letters, 1998. 73(21): p. 3076-3078.

87. Zhang, R.Q., Y. Lifshitz, and S.T. Lee, Oxide-assisted growth of semiconducting nanowires. Advanced Materials, 2003. 15(7-8): p. 635-640.

88. Zhang, M., et al., Bright visible photoluminescence from silica nanotube flakes prepared by the sol–gel template method. Applied physics letters, 2002. 80(3): p. 491-493.

89. Wu, X., et al., Preparation and photoluminescence properties of amorphous silica nanowires. Chemical physics letters, 2001. 336(1-2): p. 53-56.

90. Wang, Z.L., Nanobelts, nanowires, and nanodiskettes of semiconducting oxides—from materials to nanodevices. Advanced Materials, 2003. 15(5): p. 432-436.

91. Simakov, V., et al., Experimental investigation and modeling of temperature influence on vertical and radial growth rate of tin dioxide nanowires synthesized by catalyst-free thermal evaporation method. Materials Chemistry and Physics, 2020. 242: p. 122502.

92. Dubrovskiĭ, V., et al., Effect of deposition conditions on nanowhisker morphology. Semiconductors, 2007. 41(7): p. 865-874.

93. Dubrovskii, V. and Y.Y. Hervieu, Diffusion-induced growth of nanowires: Generalized boundary conditions and self-consistent kinetic equation. Journal of crystal growth, 2014. 401: p. 431-440.

94. Dubrovskii, V., et al., Narrowing the length distribution of Ge nanowires. Physical review letters, 2012. 108(10): p. 105501.

95. Schmidtbauer, J., et al., Germanium nanowire growth controlled by surface diffusion effects. Applied Physics Letters, 2012. 101(4): p. 043105.

96. Dubrovskii, V. and M. Timofeeva, Modeling GaN nanowire growth on silicon. Technical Physics Letters, 2013. 39(1): p. 127-129.

97. Johansson, J., et al., Mass transport model for semiconductor nanowire growth. The Journal of Physical Chemistry B, 2005. 109(28): p. 13567-13571.

98. Chandrasekaran, S., Additive Manufacturing of 3D Printed SiC Composites: Strengthening and Densification Through Surface Modification and Use of Mineral Binders. 2023, The University of North Carolina at Charlotte.

99. Charmas, B., et al., Characterization of multimodal silicas using TG/DTG/DTA, Q-TG, and DSC methods. Colloids and Interfaces, 2018. 3(1): p. 6.

100. Kwon, D.-J., et al., Interfacial properties and thermal aging of glass fiber/epoxy composites reinforced with SiC and SiO2 nanoparticles. Composites Part B: Engineering, 2017. 130: p. 46-53.

101. El-Ghannam, A., et al., Synthesis and characterization of porous bioactive SiC tissue engineering scaffold. Journal of Biomedical Materials Research Part A, 2020. 108(11): p. 2162-2174.

102. Zhuravlev, L., The surface chemistry of amorphous silica. Zhuravlev model. Colloids and Surfaces A: Physicochemical and Engineering Aspects, 2000. 173(1-3): p. 1-38.

103. Tahiri, N., et al. Study of the thermal treatment of SiO2 aggregate. in IOP Conference Series: Materials Science and Engineering. 2014. IOP Publishing.

104. Fokin, V.M., et al., Critical assessment of DTA–DSC methods for the study of nucleation kinetics in glasses. Journal of Non-Crystalline Solids, 2010. 356(6-8): p. 358-367.

105. Jorgensen, P.J., M.E. Wadsworth, and I.B. Cutler, Oxidation of silicon carbide. Journal of the American Ceramic Society, 1959. 42(12): p. 613-616.

106. Auweter-Kurtz, M., et al., Investigation of oxidation protected C/C heat shield material in different plasma wind tunnels. Acta Astronautica, 1999. 45(2): p. 93-108.

107. Harder, B., N. Jacobson, and D. Myers, Oxidation transitions for SiC part II. Passive-to-active transitions. Journal of the American Ceramic Society, 2013. 96(2): p. 606-612.

108. Sultana, F., et al., Synthesis and characterization of functionally graded SiC-mullite thermal material. Journal of Solid State Chemistry, 2023: p. 124414.

109. Ramírez-Rico, J., J. Martínez-Fernández, and M. Singh, Effect of oxidation on the compressive strength of sintered SiC-fiber bonded ceramics. Materials Science and Engineering: A, 2012. 534: p. 394-399.

110. Wagner, R.S. and W.C. Ellis, VAPOR-LIQUID-SOLID MECHANISM OF SINGLE CRYSTAL GROWTH. Applied Physics Letters, 1964. 4(5): p. 89-90.

111. Filby, J.D. and S. Nielsen, Growth of epitaxial layers of silicon by sublimation through thin alloy zones. British Journal of Applied Physics, 1966. 17(1): p. 81.

112. Kamins, T.I., et al., Ti-catalyzed Si nanowires by chemical vapor deposition: Microscopy and growth mechanisms. Journal of Applied Physics, 2001. 89(2): p. 1008-1016.

113. Hudak, B.M., et al., Understanding nanomaterial synthesis with in situ transmission electron microscopy. Microscopy and Microanalysis, 2015. 21(S3): p. 1507-1508.

114. Huson, J.J., et al., Reaction intermediate-induced vapor–liquid–solid growth of silicon oxide nanowires. CrystEngComm, 2018. 20(45): p. 7256-7265.

115. Wu, Y. and P. Yang, Direct Observation of Vapor−Liquid−Solid Nanowire Growth. Journal of the American Chemical Society, 2001. 123(13): p. 3165-3166.

116. Mohammad, S.N., Analysis of the Vapor–Liquid–Solid Mechanism for Nanowire Growth and a Model for this Mechanism. Nano Letters, 2008. 8(5): p. 1532-1538.

117. Dai, Z.R., Z.W. Pan, and Z.L. Wang, Novel Nanostructures of Functional Oxides Synthesized by Thermal Evaporation. Advanced Functional Materials, 2003. 13(1): p. 9-24.

118. Ambrosini, S., et al., Vapor-liquid-solid and vapor-solid growth of self-catalyzed GaAs nanowires. AIP Advances, 2011. 1(4): p. 042142.

119. Sheng, T., et al., Growth of ultra-long sodium tungsten oxide and tungsten oxide nanowires: Effects of impurity and residue deposition. Journal of Crystal Growth, 2014. 395: p. 61–67.

120. Pan, Z.W., Z.R. Dai, and Z.L. Wang, Nanobelts of semiconducting oxides. Science, 2001. 291(5510): p. 1947-1949.

121. Wang, Y., et al., Zn nanobelts: a new quasi one-dimensional metal nanostructure. Chemical Communications, 2001(24): p. 2632-2633.

122. Jiang, Y., et al., Zinc selenide nanoribbons and nanowires. The Journal of Physical Chemistry B, 2004. 108(9): p. 2784-2787.

123. Zhang, J., F. Jiang, and L. Zhang, Fabrication of single-crystalline semiconductor CdS nanobelts by vapor transport. The Journal of Physical Chemistry B, 2004. 108(22): p. 7002-7005.

124. Dalacu, D., et al., Selective-area vapour–liquid–solid growth of InP nanowires. Nanotechnology, 2009. 20(39): p. 395602.

125. Ahmad, I., et al., Fe-Assisted Synthesis of Si Nanowires. The Journal of Physical Chemistry C, 2009. 113(4): p. 1286-1292.

126. Cho, S.K. and T. Lim, Catalyst-mediated doping in electrochemical growth of solar silicon. Electrochimica Acta, 2021. 367: p. 137472.

127. Yao, Y. and S. Fan, Si nanowires synthesized with Cu catalyst. Materials Letters, 2007. 61(1): p. 177-181.

128. Qiu Zhu, Y., et al., 3D Silicon oxide nanostructures: from nanoflowers to radiolaria. Journal of Materials Chemistry, 1998. 8(8): p. 1859-1864.

129. Tuan, H.-Y., et al., Catalytic Solid-Phase Seeding of Silicon Nanowires by Nickel Nanocrystals in Organic Solvents. Nano Letters, 2005. 5(4): p. 681-684.

130. Peng, H., et al., Morphology Control of Layer-Structured Gallium Selenide Nanowires. Nano Letters, 2007. 7(1): p. 199-203.

131. Bae, J., et al., VLS growth of Si nanocones using Ga and Al catalysts. Journal of Crystal Growth, 2008. 310(20): p. 4407-4411.

132. Chase Jr, M.W., JANAF thermochemical tables. J. Phys. Chem. Ref. Data, 1985.

133. Mehner, T., et al., Transition metal derivatives of SiO: interaction of molecular SiO with silver atoms in an argon matrix. Journal of the Chemical Society, Chemical Communications, 1988(2): p. 117-119.

134. Mehner, T., R. Köppe, and H. Schnöckel, Evidence for [PdSiO] from IR spectroscopy. Angewandte Chemie International Edition in English, 1992. 31(5): p. 638-640.

135. González-Fariña, R., et al., Modeling microsilica particle formation and growth due to the combustion reaction of silicon monoxide with oxygen. SIAM Journal on Applied Mathematics, 2020. 80(2): p. 1003-1033.

136. Buckmaster, J.D., The mathematics of combustion. 1985: SIAM.

137. Upadhyay, S.K., Reaction dynamics. 2006: Springer.

138. Abolpour, B. and R. Shamsoddini, Mechanism of reaction of silica and carbon for producing silicon carbide. Progress in Reaction Kinetics and Mechanism, 2020. 45: p. 1468678319891416.

139. Rockett, A., The materials science of semiconductors. 2007: Springer Science & Business Media.

140. Shi, J., et al., Evolution of zinc oxide nanostructures through kinetics control. Journal of materials chemistry, 2011. 21(25): p. 9000-9008.

141. Borrero-López, O., et al., Microstructural design of sliding-wear-resistant liquid-phase-sintered SiC: an overview. Journal of the European Ceramic Society, 2007. 27(11): p. 3351-3357.

142. Janney, M.A., Mechanical properties and oxidation behavior of a hot-pressed SiC-15-vol%-TiB/sub 2/composite. Am. Ceram. Soc. Bull.;(United States), 1987. 66(2).

143. Chin, H.S., K.Y. Cheong, and A.B. Ismail, A review on die attach materials for SiC-based high-temperature power devices. Metallurgical and Materials Transactions B, 2010. 41: p. 824-832.

144. Ortiz, A., et al., A route for the pressureless liquid-phase sintering of SiC with low additive content for improved sliding-wear resistance. Journal of the European Ceramic Society, 2012. 32(4): p. 965-973.

145. Ribeiro, S., et al., Effect of heating rate on the shrinkage and microstructure of liquid phase sintered SiC ceramics. Ceramics International, 2016. 42(15): p. 17398-17404.

146. Malinge, A., et al., Pressureless sintering of beta silicon carbide nanoparticles. Journal of the European ceramic society, 2012. 32(16): p. 4393-4400.

147. Nadeau, J.S., Very high pressure hot pressing of silicon carbide. 1973.

148. Hirohata, Y., et al., Gas permeability of SiC/SiC composites as fusion reactor material. Fusion engineering and design, 2002. 61: p. 699-704.

149. Datta, M., A. Bandyopadhyay, and B. Chaudhuri, Sintering of nano crystalline α silicon carbide by doping with boron carbide. Bulletin of Materials Science, 2002. 25: p. 181-189.

150. Zhang, X.F., Q. Yang, and L.C. De Jonghe, Microstructure development in hot-pressed silicon carbide: effects of aluminum, boron, and carbon additives. Acta materialia, 2003. 51(13): p. 3849-3860.

151. Suzuki, K. and M. Sasaki, Fundamental Structural Ceramics. Edited by S. Somiya and RC Bradt. 1987, Terra Scientific Publishing Company, Tokyo, Japan.

152. Nader, M., F. Aldinger, and M. Hoffmann, Influence of the α/β-SiC phase transformation on microstructural development and mechanical properties of liquid phase sintered silicon carbide. Journal of Materials Science, 1999. 34(6): p. 1197-1204.

153. Kim, Y.W., M. Mitomo, and H. Hirotsuru, Microstructural development of silicon carbide containing large seed grains. Journal of the American Ceramic Society, 1997. 80(1): p. 99-105.

154. Rixecker, G., et al., High-temperature effects in the fracture mechanical behaviour of silicon carbide liquid-phase sintered with AlN–Y2O3 additives. Journal of the European Ceramic Society, 2001. 21(8): p. 1013-1019.

155. Sciti, D. and A. Bellosi, Effects of additives on densification, microstructure and properties of liquid-phase sintered silicon carbide. Journal of materials science, 2000. 35: p. 3849-3855.

156. Kim, J.Y., et al., Microstructure and Mechanical Properties of alpha-Silicon Carbide Sintered with Yttrium-Aluminum Garnet and Silica. Journal of the American Ceramic Society, 1999. 82(2): p. 441-444.

157. Zhou, Y., et al., Tailoring the mechanical properties of silicon carbide ceramics by modification of the intergranular phase chemistry and microstructure. Journal of the European Ceramic Society, 2002. 22(14-15): p. 2689-2696.

158. Becher, P.F., et al., Compositional effects on the properties of Si-Al-RE-based oxynitride glasses (RE= La, Nd, Gd, Y, or Lu). Journal of the American Ceramic Society, 2002. 85(4): p. 897-902.

159. Jou, Z.C., A.V. Virkar, and R.A. Cutler, High temperature creep of SiC densified using a transient liquid phase. Journal of materials research, 1991. 6(9): p. 1945-1949.

160. Chen, D., et al., Role of the grain-boundary phase on the elevated-temperature strength, toughness, fatigue and creep resistance of silicon carbide sintered with Al, B and C. Acta materialia, 2000. 48(18-19): p. 4599-4608.

161. Lidén, E., et al., Homogeneous Distribution of Sintering Additives in Liquid-Phase Sintered Silicon Carbide. Journal of the American Ceramic Society, 1995. 78(7): p. 1761-1768.

162. Choi, H.-J., et al., Intergranular glassy phase free SiC ceramics retains strength at 1500° C. Scripta materialia, 2004. 50(9): p. 1203-1207.

163. Resmi, V., et al., Processing of silica bonded porous SiC preform for metallic composites. Journal of Porous Materials, 2015. 22: p. 1445-1454.

164. Zhu, S., et al., Preparation and characterization of SiC/cordierite composite porous ceramics. Ceramics International, 2007. 33(1): p. 115-118.

165. Bai, C.-Y., et al., Fabrication and properties of cordierite–mullite bonded porous SiC ceramics. Ceramics International, 2014. 40(4): p. 6225-6231.

166. Liu, S., Y.-P. Zeng, and D. Jiang, Fabrication and characterization of cordierite-bonded porous SiC ceramics. Ceramics International, 2009. 35(2): p. 597-602.

167. She, J., T. Ohji, and Z.Y. Deng, Thermal shock behavior of porous silicon carbide ceramics. Journal of the American Ceramic Society, 2002. 85(8): p. 2125-2127.

168. She, J., et al., High-strength porous silicon carbide ceramics by an oxidation-bonding technique. Journal of the American Ceramic Society, 2002. 85(11): p. 2852-2854.

169. Choi, Y.-H., et al., Effect of alkaline earth metal oxide addition on flexural strength of porous mullite-bonded silicon carbide ceramics. Journal of materials science, 2010. 45: p. 6841-6844.

170. Eom, J.-H., et al., Effect of submicron silicon carbide powder addition on the processing and strength of reaction-sintered mullite-silicon carbide composites. Journal of the Ceramic Society of Japan, 2009. 117(1364): p. 421-425.

171. Jing, Y., et al., Fabrication and properties of SiC/mullite composite porous ceramics. Ceramics international, 2014. 40(1): p. 1329-1334.

172. Luo, Z.-Y., et al., In-situ reaction bonding to obtain porous SiC membrane supports with excellent mechanical and permeable performance. Ceramics International, 2019. 45(7): p. 9007-9016.

173. Bukhari, S.Z.A., et al., Oxidation-bonded SiC membrane for microfiltration. Journal of the European Ceramic Society, 2018. 38(4): p. 1711-1719.

174. Bai, C.-y., et al., Preparation and properties of mullite-bonded porous SiC ceramics using porous alumina as oxide. Materials characterization, 2014. 90: p. 81-87.

175. Chae, S.-H., et al., Low temperature processing and properties of porous frit-bonded SiC ceramics. Journal of the Korean Ceramic Society, 2009. 46(5): p. 488-492.

176. Zhang, W., et al., Mechanical properties and thermal stability of carbon fiber cloth reinforced sol-derived mullite composites. Journal of Advanced Ceramics, 2019. 8: p. 218-227.

177. Arai, Y. and R. Inoue, Detection of small delamination in mullite/Si/SiC model EBC system by pulse thermography. Journal of Advanced Ceramics, 2019. 8: p. 438-447.

178. Cape, J. and G. Lehman, Temperature and finite pulse-time effects in the flash method for measuring thermal diffusivity. Journal of applied physics, 1963. 34(7): p. 1909-1913.

179. Touloukian, Y.S., Thermophysical properties of matter. Master Index to Materials and Properties, 1979.

180. Ding, S., Y. Zeng, and D. Jiang, Preparation and properties of in situ reaction bonded porous SiC ceramics. J. Inorg. Mater., 2006. 21: p. 1397-1403.

181. BV, M., et al., Effect of aluminum source on flexural strength of mullite-bonded porous silicon carbide ceramics. Journal of the Ceramic Society of Japan, 2010. 118(1373): p. 13-18.

182. Schneider, H., J. Schreuer, and B. Hildmann, Structure and properties of mullite—A review. Journal of the European Ceramic Society, 2008. 28(2): p. 329-344.

183. Ma, C., et al., Mullite oxidation resistant coating for SiC-coated carbon/carbon composites by supersonic plasma spraying. Journal of Materials Science & Technology, 2013. 29(1): p. 29-33.

184. Kumar, B.M., et al., Effect of aluminum hydroxide content on porosity and strength of porous mullite-bonded silicon carbide ceramics. Journal of the Ceramic Society of Japan, 2011. 119(1389): p. 367-370.

185. Ding, S., Y.-P. Zeng, and D. Jiang, Thermal shock behaviour of mullite-bonded porous silicon carbide ceramics with yttria addition. Journal of Physics D: Applied Physics, 2007. 40(7): p. 2138.

186. Li, Z., et al., A novel sintering additive system for porous mullite-bonded SiC ceramics: High mechanical performance with controllable pore structure. Ceramics International, 2022. 48(3): p. 4105-4114.

187. Han, F., et al., High gas permeability of SiC porous ceramics reinforced by mullite fibers. Journal Of the European Ceramic Society, 2016. 36(16): p. 3909-3917.

188. Lutterotti, L., S. Matthies, and H. Wenk, MAUD: a friendly Java program for material analysis using diffraction. CPD NEWSLETTER, 1999. 21: p. 14-15.

189. Luo, H., et al., Effects of fabrication processes on the properties of SiC/SiC composites. Ceramics International, 2021. 47(16): p. 22669-22676.

190. Ghosh, P., et al., The influence of temperature on the solubility limit of Ca in alumina. Journal of the European Ceramic Society, 2020. 40(15): p. 5767-5772.

191. Sultana, F., et al., Synthesis and characterization of functionally graded SiC-mullite thermal material. Journal of Solid State Chemistry, 2024. 330: p. 124414.

192. Fritze, H., et al., Mullite based oxidation protection for SiC–C/C composites in air at temperatures up to 1900 K. Journal of the European Ceramic Society, 1998. 18(16): p. 2351-2364.

193. Qiao, Z., et al., The mineralogical characteristics between opaline silica in bentonite and α-cristobalite. Solid State Sciences, 2019. 96: p. 105948.

194. Wang, W., et al., Molten salt synthesis of mullite whiskers on the surface of SiC ceramics. Journal of alloys and compounds, 2014. 582: p. 96-100.

195. Cividanes, L.S., et al., Review of mullite synthesis routes by sol–gel method. Journal of Sol-Gel Science and Technology, 2010. 55(1): p. 111-125.

196. Beran, A., D. Voll, and H. Schneider, Dehydration and structural development of mullite precursors: an FTIR spectroscopic study. Journal of the European Ceramic Society, 2001. 21(14): p. 2479-2485.

197. Sultana, P., et al., Effect of size of fly ash particle on enhancement of mullite content and glass formation. Bulletin of Materials Science, 2011. 34: p. 1663-1670.

198. Kobayashi, S.-i., IR spectroscopic study of silicon nitride films grown at a low substrate temperature using very high frequency plasma-enhanced chemical vapor deposition. World Journal of Condensed Matter Physics, 2016. 6(4): p. 287-293.

199. Mishra, R. and R. Ningthoujam, High-temperature ceramics, in Materials under extreme conditions. 2017, Elsevier. p. 377-409.

200. Schneider, H., Solubility of TiO2, Fe2O3 and MgO in mullite. Ceramics International, 1987. 13(2): p. 77-82.

201. Schneider, H. and H. Rager, Occurrence of Ti3+ and Fe2+ in mullite. Journal of the American Ceramic Society, 1984. 67(11): p. c248-c250.

202. Scheider, H., Temperature-Dependent Iron Solubility in Mullite. Journal of the American Ceramic Society, 1987. 70(3): p. C-43-C-45.

203. Xu, X., et al., Preparation and characterization of mullite-silicon carbide heat absorbing ceramics for solar thermal tower plant. Journal of Wuhan University of Technology-Mater. Sci. Ed., 2015. 30: p. 27-32.

204. Lima, M., et al., Structural, electrical and thermal properties of borosilicate glass–alumina composites. Journal of Alloys and Compounds, 2012. 538: p. 66-72.

205. Monteverde, F. and L. Scatteia, Resistance to thermal shock and to oxidation of metal diborides–SiC ceramics for aerospace application. Journal of the American Ceramic Society, 2007. 90(4): p. 1130-1138.

206. Yang, L., et al., Thermal resistant, mechanical and electrical properties of a novel ultrahigh-content randomly-oriented CNTs reinforced SiC matrix composite-sheet. Composites Part B: Engineering, 2017. 119: p. 10-17.

207. Ekimov, E.A., et al., Structural and optical properties of silicon carbide powders synthesized from organosilane using high-temperature high-pressure method. Nanomaterials, 2021. 11(11): p. 3111.

208. Sarangi, M., P. Nayak, and T. Tiwari, Effect of temperature on nano-crystalline silica and carbon composites obtained from rice-husk ash. Composites Part B: Engineering, 2011. 42(7): p. 1994-1998.

209. Gao, H., et al., Temperature-dependent dielectric and microwave absorption properties of silicon carbide fiber-reinforced oxide matrices composite. Journal of Materials Science, 2018. 53(22): p. 15465-15473.

210. Malki, M., et al., Electrical conductivity of mullite ceramics. Journal of the American Ceramic Society, 2014. 97(6): p. 1923-1930.

211. Samvedi, V. and V. Tomar, An ab initio study of ZrB2–SiC interface strength as a function of temperature: Correlating phononic and electronic thermal contributions. Journal of the European Ceramic Society, 2013. 33(3): p. 615-625.

212. Yun, S.I., S. Nahm, and S.W. Park, Effects of SiC particle size on flexural strength, permeability, electrical resistivity, and thermal conductivity of macroporous SiC. Ceramics International, 2022. 48(1): p. 1429-1438.

213. Xu, X., et al., Preparation and thermal shock resistance of mullite and corundum Co-bonded SiC ceramics for solar thermal storage. Journal of Wuhan University of Technology-Mater. Sci. Ed., 2020. 35: p. 16-25.

214. Parchovianský, M., et al., Thermal behavior, electrical conductivity and microstructure of hot pressed Al2O3/SiC nanocomposites. Ceramics International, 2014. 40(9): p. 14421-14429.

APPENDIX A: DISCRETIZED VERSION OF ODES FOR EQUATIONS (10-13)

The complete set of discretized ODEs representing equation (10) can be given as,

$$\left(C_{Si(OH)_4}\right)_{n+1} = \left(C_{Si(OH)_4}\right)_n - 2\cdot dt\cdot K_2\left(C_{Si(OH)_4}\right)_n\left(C_{Si(OH)_4}\right)_n \tag{21a}$$

$$\left(C_{SiO_2}\right)_{n+1} = \left(C_{SiO_2}\right)_n + 2\cdot dt\cdot K_2\left(C_{Si(OH)_4}\right)_n\left(C_{Si(OH)_4}\right)_n \tag{21b}$$

$$\left(C_{H_2O}\right)_{n+1} = \left(C_{H_2O}\right)_n + 4\cdot dt\cdot K_2\left(C_{Si(OH)_4}\right)_n\left(C_{Si(OH)_4}\right)_n \tag{21c}$$

The complete set of discretized ODEs representing equation (11) can be given as,

$$\left(C_{SiO_2}\right)_{n+1} = \left(C_{SiO_2}\right)_n - dt\cdot K_3\left(C_{SiO_2}\right)_n\left(C_{C^-}\right)_n \tag{22a}$$

$$\left(C_{C^-}\right)_{n+1} = \left(C_{C^-}\right)_n - dt\cdot K_3\left(C_{SiO_2}\right)_n\left(C_{C^-}\right)_n \tag{22b}$$

$$\left(C_{SiO}\right)_{n+1} = \left(C_{SiO}\right)_n + dt\cdot K_3\left(C_{SiO_2}\right)_n\left(C_{C^-}\right)_n \tag{22c}$$

$$\left(C_{CO}\right)_{n+1} = \left(C_{CO}\right)_n + dt\cdot K_3\left(C_{SiO_2}\right)_n\left(C_{C^-}\right)_n \tag{22d}$$

The complete set of discretized ODEs representing equation (12) can be given as,

$$\left(C_{SiO}\right)_{n+1} = \left(C_{SiO}\right)_n - 2\cdot dt\cdot K_4\left(C_{SiO}\right)_n\left(C_{O_2}\right)_n \tag{23a}$$

$$\left(C_{O_2}\right)_{n+1} = \left(C_{O_2}\right)_n - dt\cdot K_4\left(C_{SiO}\right)_n\left(C_{O_2}\right)_n \tag{23b}$$

$$\left(C_{SiO_2}\right)_{n+1} = \left(C_{SiO_2}\right)_n + 2\cdot dt\cdot K_4\left(C_{SiO}\right)_n\left(C_{O_2}\right)_n \tag{23c}$$

The complete set of discretized ODEs representing equation (13) can be given as,

$$\left(C_{Si(OH)_4}\right)_{n+1} = \left(C_{Si(OH)_4}\right)_n - 2\cdot dt\cdot K_5\left(C_{Si(OH)_4}\right)_n\left(C_{Si(OH)_4}\right)_n \tag{24a}$$

$$\left(C_{SiO_2}\right)_{n+1} = \left(C_{SiO_2}\right)_n + 2\cdot dt\cdot K_5\left(C_{Si(OH)_4}\right)_n\left(C_{Si(OH)_4}\right)_n \tag{24b}$$

$$\left(C_{H_2O}\right)_{n+1} = \left(C_{H_2O}\right)_n + 4\cdot dt\cdot K_5\left(C_{Si(OH)_4}\right)_n\left(C_{Si(OH)_4}\right)_n \tag{24c}$$

APPENDIX B: COMPARISON BETWEEN CRISTOBALITE VS MULLITE AS BINDING AGENT FOR SIC

SiC-Cristobalite discs were prepared using a protocol previously reported from our laboratory. Briefly, 1000 mg of 40 µm SiC was mixed with 60 µL of 10%, 15%, or 20% NaOH, the mixture was compacted at 250 MPa for 30 mins in a hydraulic press to produce a disc of 10 mm diameter x 5.8 mm height. The discs were then subjected to a thermal treatment at 1400 °C/1 hr at 10 °C/min. The mechanical strength of the SiC-Cristobalite discs were measured and compared to SiC-mullite prepared under the same experimental conditions.

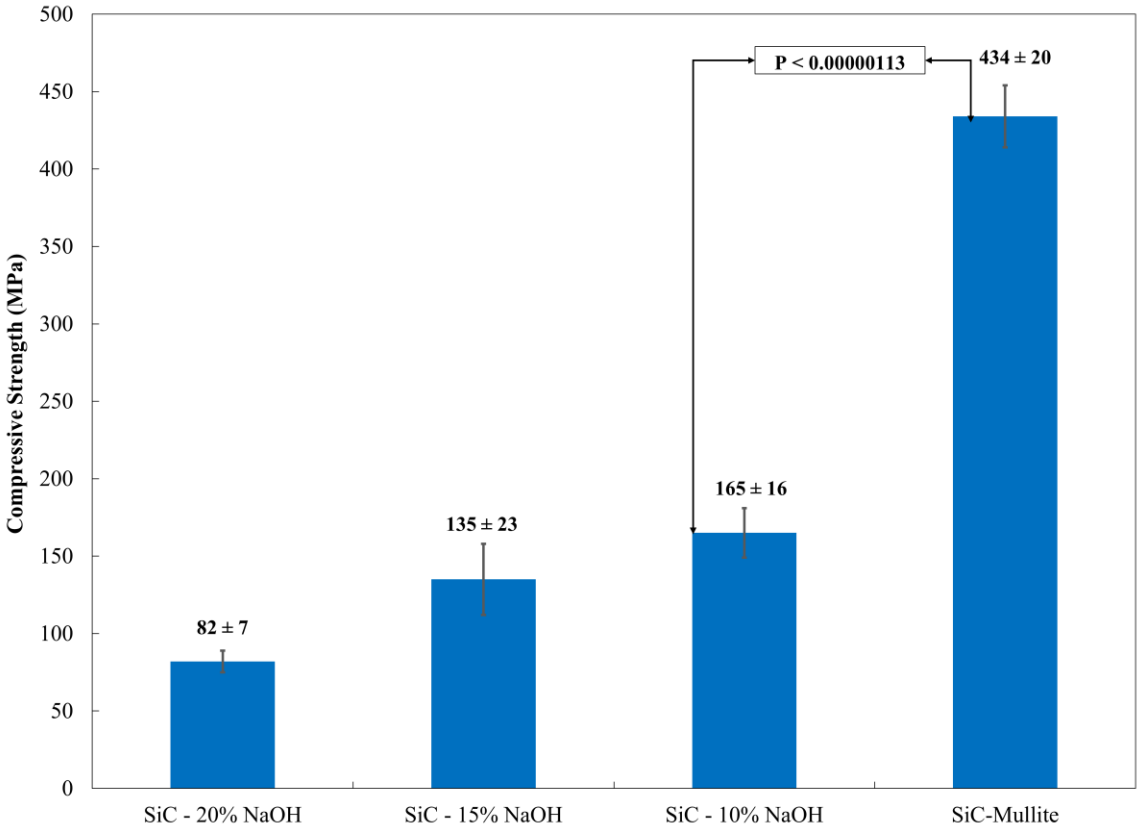

Figure A1: Comparison of mechanical properties of SiC cristobalite prepared by using 10%, 15%, and 20% NaOH solutions and SiC-mullite composite prepared by mixing 90 wt% SiC with 10 wt% ash, pressed at 250 MPa/30 min and heat treated at 1400 °C/1 hr.

SiC-mullite composite shows significantly high mechanical strength compared to SiC-cristobalite, (Figure A1). It is evident from the compression data that the increase in cristobalite

phase; after treatment of SiC particles with high NaOH concentration and heat treatment at 1400 °C/1h, resulted in a significant decrease in the mechanical strength. The compression strength for SiC-cristobalite samples decreased as the concentration of NaOH used to treat the samples increased in the order 10% > 15% > 20%. From this compressive strength analysis, secondary mullite phase is much stronger than cristobalite and hence provides stronger adhesion for SiC particles.